Magnetic Vortex Dynamics: Non-linear Dynamics, Pinning Mechanisms, and Dimensionality Crossover

A DISSERTATION
SUBMITTED TO THE FACULTY OF THE GRADUATE SCHOOL
OF THE UNIVERSITY OF MINNESOTA
BY

Te-Yu Chen

IN PARTIAL FULFILLMENT OF THE REQUIREMENTS
FOR THE DEGREE OF
Doctor of Philosophy

Paul A. Crowell

January, 2012

Acknowledgements

I joined Professor Paul Crowell's group in the summer of 2007. Paul is knowledgeable and is always generous with his time. Learning from his excellent research insight and problem-solving skills has been the most valuable experience in my graduate study. I am grateful to have had the opportunity to work with him.

Johoo Park established the original time-resolved Kerr microscope setup, and Rob Compton improved the setup for studying the dynamics of magnetic vortices. They developed various experimental techniques and LabVIEW software infrastructure that I still use today. I am grateful to inherit the knowledge and techniques which they established in this Lab.

The research which I discuss in this dissertation is a collaboration work with Professor Chris Leighton's group in the Chemical Engineering and Materials Science Department of the University of Minnesota. All of the samples shown in my dissertation were grown in Chris' lab. I also would like to thank Chris for valuable discussions and advices.

I have also had the pleasure of working directly with Rob Compton, Mun Chan, Mike Erickson, and Andrew Galkiewicz. Rob was my mentor when I joined the group, and he fabricated the samples which I used for studying the nonlinear vortex dynamics. Mun developed the original fabrication process which I optimized for patterning magnetic disks in my research. Mike grew all the samples which I used for studying pinning mechanisms and dimensionality crossover of vortex dynamics. Andrew Galkiewicz developed the double modulation technique and he also conducted some of the micromagnetic simulations discussed in this

dissertation.

I owe many thanks to all of the other members of the Crowell group, including Chad Geppert, Eric Garlid, Kevin Christie, Dmitry Spivak, and Changjiang Liu. They were always happy to discuss physics or to help me prepare presentations.

My wife, Yu-Wen Chen, is smart, funny, and wonderful. Yu-Wen has been my most cherished partner in these last six years together, and I'm grateful for her love. I must thank my parents for always supporting me in all possible ways, especially during the past few years when I'm 7,129 miles away from them.

This work was supported by the MRSEC Program of the National Science Foundation under Award Number DMR-0819885, and the University of Minnesota Graduate School through the Doctoral Dissertation Fellowship. Additional support for the Nanofabrication Center was provided by the NSF NNIN network. The figure from Physical Review Letter has been reprinted with permission from the American Physical Society (APS). The figure from Science has been reprinted with permission from the American Association for the Advancement of Science (AAAS).

Abstract

The dynamics of a magnetic vortex, which is the simplest realization of a domain structure, are influenced profoundly by non-linear effects at both large and small amplitudes. For example, a strongly driven magnetic vortex is unstable with respect to internal deformation, leading to reversal of its core magnetization. At small amplitudes, a second class of non-linear phenomena are associated with pinning of the vortex core. The pinning of magnetic vortices is closely related to the pinning of domain walls in ferromagnetic films. For both cases, however, the absence of an appropriate characterization tool has limited the ability to correlate the physical and magnetic microstructures of ferromagnetic films with specific pinning mechanisms. Given this range of phenomena, there is also an acute need for a global picture of vortex dynamics over a wide range of excitation amplitudes and frequencies.

In this dissertation, I show a global phase diagram of vortex dynamics in permalloy ($Ni_{80}Fe_{20}$) disks by probing the response spectrum over four orders of magnitude in excitation power. A clear boundary separates pinned and unpinned dynamics in a phase space of amplitude and frequency. I also discuss a highly quantitative analysis of the pinning potential for defects, and how it can be used to trace the dynamics of a single vortex from deep in the pinning regime to the onset of core reversal. Regarding the pinning mechanism, I show that the pinning of a magnetic vortex is strongly correlated with surface roughness, and I make a quantitative comparison of the pinning energy and spatial range in films of various thickness. The results demonstrate that thickness fluctuations on the lateral length scale of the vortex core diameter, i.e., an effective roughness at a specific length scale, provide the dominant pinning mechanism. I argue that this mechanism will be important in virtually any soft ferromagnetic film.

Finally, I show the dynamics of a magnetic vortex cross over from two-dimensional (2D) to three-dimensional (3D) with increasing disk thickness. A 2D mode of the

vortex dynamics is the lowest frequency excitation below the crossover region, above which a 3D mode becomes the lowest frequency excitation.

Contents

List of Tables

List of Figures

Chapter 1

Introduction

The research of magnetization dynamics describes how a magnetic material responds when excited by a variety of sources, such as magnetic fields, spin-polarized currents [1–15], polarized light [16–20], or temperature gradients [21]. In this dissertation I will focus on the magnetization dynamics excited by magnetic fields. For example, the magnetization direction of a ferromagnet can be changed by applying a magnetic field, and the reversal process from one saturated magnetization direction to the reversed direction is of particular interest for magnetic devices, such as hard disk drives of computers.

It is well-known that the magnetization dynamics of a ferromagnet are governed by fundamental magnetic energies, i.e., exchange energy, dipole energy, magnetostatic energy, crystalline anisotropy energy, and Zeeman energy, which will be discussed in Sec 1.1. It has been challenging, however, to describe precisely how these energies and the magnetization change with time in real materials. The challenges arise from the inevitable disorder in the material.

As will be discussed in Sec. 1.3, for example, the dynamics of a magnetic domain wall are strongly affected by pinning defects in the material. Magnetic domain walls are the boundaries of magnetic domains, within which the magnetization is uniformly aligned. When excited by a magnetic field, some domains expand while others become smaller, resulting in the motion of domain walls. In

the presence of pinning defects, a domain wall moves stochastically and discontinuously. This is often the dynamical process by which a ferromagnet reverses its magnetization.

Although pinning of domain walls is ubiquitous, the microscopic mechanism of pinning remains unclear for virtually all soft ferromagnetic materials. Quantitative measurements of the physical properties (i.e., strength and range) of pinning sites are required to provide essential information for identifying the pinning mechanisms, but such measurements have been practically impossible in extended structures such as thin films. The reason is that the structures of domain walls are generally very complex, and every domain wall interacts with multiple pinning sites simultaneously.

In this dissertation, I will focus on the simplest realization of a domain structure - a single vortex in a circular ferromagnetic disk. Similar to the dynamics of a domain wall, the dynamics of a vortex are strongly affected by pinning defects. But, unlike a domain wall, the structure of a single vortex is simple and well-defined. Additionally, the lowest frequency excitation of a vortex, i.e., the gyrotropic mode, can be described by an analytical theory, which provides a foundation for the development of analytical models for vortex pinning. These advantages make a single vortex a model system for studying how disorder affects the dynamics of a non-uniform domain structure, as will be detailed in Sec. 1.4.

This introductory chapter will outline the basic principles of magnetization dynamics, including the dynamics of magnetic domain walls and magnetic vortices. Equations will be written in CGS units in this dissertation unless otherwise indicated.

1.1 Energies of a Ferromagnet

The magnetic properties of a ferromagnet are governed by four magnetic energies, including the exchange energy, the Zeeman energy, the magnetostatic energy, and the crystalline anisotropy energy. A brief description of these energies will be

given in the following.

1.1.1 Exchange Energy

The fundamental property of a ferromagnet is its preference for a constant magnetization direction. Deviations from this ideal case cause an energy penalty, i.e., the exchange energy W_{ex}, which is given by:

$$W_{ex} = \int_V d^3\boldsymbol{r} \frac{A}{{M_s}^2} \left(\boldsymbol{\nabla} \cdot \boldsymbol{M}(\boldsymbol{r})\right)^2, \tag{1.1}$$

where $\boldsymbol{M}$ is the magnetization (magnetic moment per unit volume), M_s is the saturation magnetization, and A is the exchange constant. Typical values for $Ni_{80}Fe_{20}$ are $M_s = 800$ emu/cm^3 and $A = 10^{-6}$ erg/cm.

1.1.2 Zeeman Energy

The Zeeman energy W_H is the interaction energy of $\boldsymbol{M}$ with an external field $\boldsymbol{H_{ext}}$, and it is given by:

$$W_H = -\int_V d^3\boldsymbol{r} \boldsymbol{M}(\boldsymbol{r}) \cdot \boldsymbol{H_{ext}}(\boldsymbol{r}). \tag{1.2}$$

It is clear from Eq. 1.2 that W_H is minimum when the magnetization aligns with the applied magnetic field.

1.1.3 Magnetostatic Energy

The magnetostatic energy W_{ms} arises from the magnetic dipole-dipole interactions. W_{ms} is given by:

$$W_{ms} = -\frac{1}{2} \int d^3\boldsymbol{r} \boldsymbol{H}_d(\boldsymbol{r}) \cdot \boldsymbol{M}(\boldsymbol{r}), \tag{1.3}$$

where the dipole field $\boldsymbol{H_d}$ has the form:

$$\boldsymbol{H}_d(\boldsymbol{r}) = \frac{1}{4\pi} \int_V d^3\boldsymbol{r'} \frac{1}{R^3} \left[3\left(\boldsymbol{M} \cdot \hat{\boldsymbol{R}}\right)\hat{\boldsymbol{R}} - \boldsymbol{M}\right], \tag{1.4}$$

where $\boldsymbol{R} = \boldsymbol{r} - \boldsymbol{r'}$. An important example is the magnetostatic energy of an extended ferromagnetic thin film. The energy of $\boldsymbol{M}$ in the plane of the film is lower than that of $\boldsymbol{M}$ along the normal axis of the film. The difference in W_{ms} is $2\pi M_s^2$.

In contrast to the short-range (exchange) interaction characterizing the exchange energy (Sec. 1.1.1), the magnetostatic energy is associated with the long-range (dipole-dipole) interaction. The competition between these two energies results in various domain structures, such as domain walls in extended ferromagnetic films (Sec. 1.3) and vortices in ferromagnetic disks (Sec. 1.4). A characteristic length in a soft ferromagnetic material is give by the exchange length:

$$L_{ex} = \sqrt{\frac{A}{2\pi {M_s}^2}}, \tag{1.5}$$

which is based on the ratio of the exchange constant to the magnetostatic energy of a thin film. A typical value for $Ni_{80}Fe_{20}$ is $L_{ex} \approx 6$ nm.

1.1.4 Crystalline Anisotropy Energy

The crystalline anisotropy energy W_a originates from the spin-orbit interaction and depends on the direction of the magnetization relative to the crystal structural axes of the material. For single crystal materials, cubic crystals have cubic anisotropies, while hexagonal and tetragonal crystals have uniaxial anisotropies. For polycrystalline materials, which are composed of many crystallites of varying size and orientation, the crystalline axis can be random or directed, determined by growth and processing conditions, resulting in an averaged global anisotropy.

The strength of the anisotropy depends strongly on the material. In polycrystalline $Ni_{80}Fe_{20}$, the anisotropic energy is typically below 1000 erg/cm^3, which is much smaller than the exchange energy and the magnetostatic energy. The magnetic properties of $Ni_{80}Fe_{20}$ are primarily determined by the exchange and magnetostatic energies.

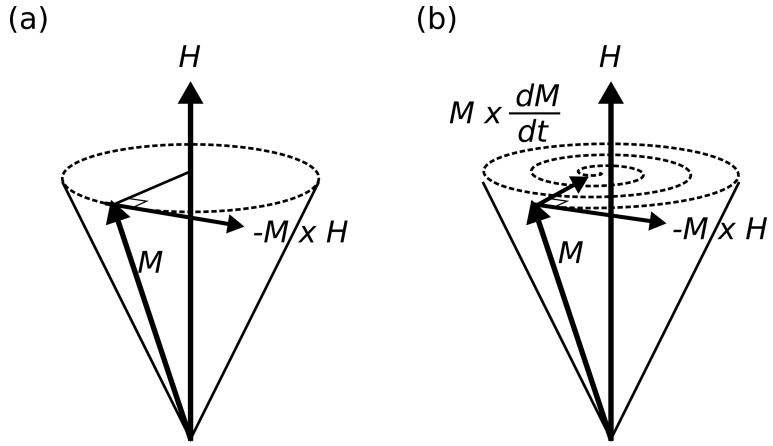

Figure 1.1: Schematic of the precession of magnetization about H. (a) Without damping. (b) With damping.

1.2 Magnetization Dynamics

This section will discuss the basic principles of magnetization dynamics. These principles will provide the foundations for the discussions of domain-wall dynamics and vortex dynamics in this dissertation.

1.2.1 Landau-Lifshitz-Gilbert (LLG) Equation

The magnetic energies discussed in Sec. 1.1 determine the magnetization dynamics. The total energy $W_{tot} = W_{ex} + W_H + W_{ms} + W_a$ leads to an effective field H_{eff}, which is defined as:

$$\boldsymbol{H_{eff}} = \frac{dW_{tot}}{d\boldsymbol{M}}. \tag{1.6}$$

H_{eff} results in a torque $\boldsymbol{M} \times \boldsymbol{H_{eff}}$ acting on the magnetization $\boldsymbol{M}$. The dynamics of $\boldsymbol{M}$ are given by:

$$\frac{d\boldsymbol{M}}{dt} = -\gamma \boldsymbol{M} \times \boldsymbol{H_{eff}}, \tag{1.7}$$

where $\gamma = g\mu_B/\hbar$ is the gyromagnetic ratio, μ_B is the Bohr magneton, and the factor g has a value close to 2 for most ferromagnetic materials [22].

Eq 1.7 is the fundamental equation of magnetization dynamics without damping. For example, if H_{eff} is constant, a circular precession mode of the magnetization occurs, as illustrated in Fig. 1.1(a). The precession frequency ω_0 is given by the Larmor frequency γH_{eff}.

In real materials damping is inevitable, but the origin of damping remains controversial. For the purpose of this dissertation, I will apply a phenomenological damping parameter α, which is the Gilbert damping constant (see Ref. [23]). The corresponding magnetization dynamics are described by the Landau-Lifshitz-Gilbert (LLG) equation [24],

$$\frac{d\boldsymbol{M}}{dt} = -\gamma \boldsymbol{M} \times \boldsymbol{H_{eff}} + \frac{\alpha}{M_s} \boldsymbol{M} \times \frac{d\boldsymbol{M}}{dt}. \tag{1.8}$$

Fig. 1.1(b) illustrates that in the presence of damping the magnetization spirals down until it becomes parallel to H_{eff}.

1.2.2 Micromagnetic Simulation

The magnetization dynamics of a ferromagnet can be numerically calculated by using Eq. 1.8. This approach is referred to as *micromagnetic simulation*. The simulated system first needs to be divided into a grid of cells. The cell size is smaller than L_{ex} (Eq. 1.5), so that the magnetization in each cell is assumed to respond as a single unit. In this case H_{eff} in Eq. 1.8 accounts for the interactions between cells, including the dipole-dipole interaction and the exchange interaction. Micromagnetic simulations can provide useful microscopic insight into the behavior of a ferromagnet. There are several micromagnetics software packages available, and the LLG Micromagnetics Simulator [25] has been used in this dissertation research.

1.3 Pinning of Magnetic Domain Walls

The pinning of magnetic domain walls has been studied intensively since 1919, the year when Barkhausen discovered the discontinuous reversal process of a ferromagnet [26]. In this section, I will discuss the static and dynamical properties of a domain wall, including the domain-wall dynamics in the presence of pinning defects. I will also point out the challenges of identifying the microscopic pinning mechanisms.

1.3.1 Magnetic Domains and Domain Walls

The magnetization of any sufficiently large ferromagnetic thin film will spontaneously break into domains. Within each domain, the magnetization aligns uniformly to minimize the exchange energy. The structure of the domains depends on the geometry of the film. For example, Fig.1.2(a) shows schematically a flux-closure domain structure near the edge of a film. The flux-closure structure of M minimizes the stray field outside the film, and therefore minimizes the magnetostatic energy.

The magnetic domains are separated by domain walls, within which the magnetization rotates continuously over a lateral range L_{DW}, i.e., the domain-wall width. Generally speaking, a large L_{DW} corresponds to small gradient of M within the domain wall, which is favorable for minimizing the exchange energy. On the other hand, a small L_{DW} is favorable for minimizing the magnetostatic energy. The competition of these two energies determines the value of L_{DW}. Therefore, similar to L_{ex} discussed in Sec. 1.1.3, L_{DW} is typically on the order of 10 nm. The exact structures of domain walls depend on both the material and the thickness of the film [24]. For example, if the thickness of the $Ni_{80}Fe_{20}$ film is below $\sim$ 20 nm, the magnetizations rotate in the plane of the wall (Néel wall), as shown in Fig.1.2(b). For thicknesses larger than $\sim$ 100 nm, the rotation is perpendicular to the plane of the wall (Bloch wall), as shown in Fig.1.2(c). For thicknesses between 20 and 100 nm, a cross-tie wall is stable, containing a chain

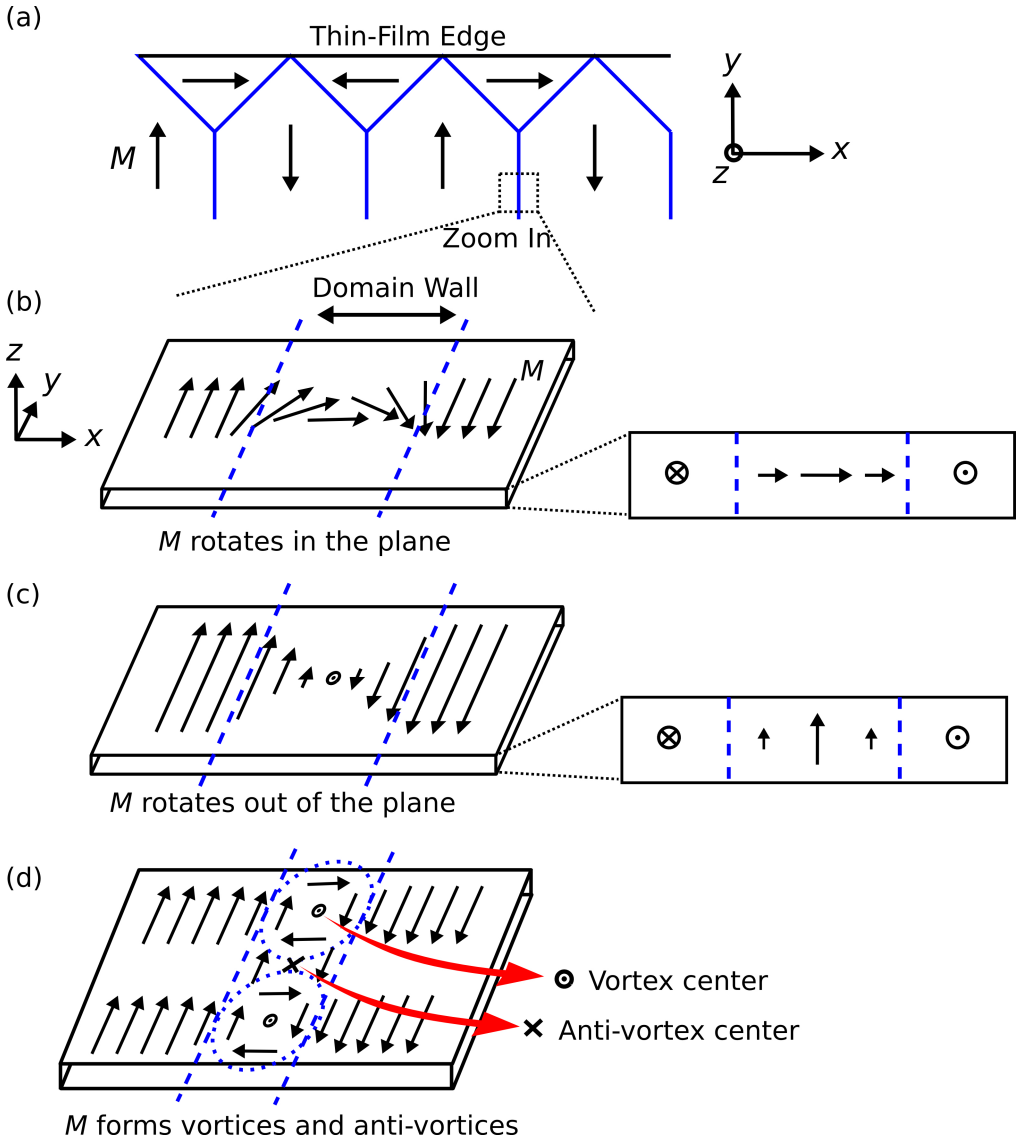

Figure 1.2: Schematic representation of (a) a simple model of flux-closure type domains at the edge of a film, (b) a Néel wall, (c) a Bloch wall, and (d) a cross-tie wall. The solid lines in (a) indicate the domain walls. The dashed lines in (b), (c), and (d) indicate the range of the domain walls. The projections into the cross-sectional dimension are shown for the Néel wall (b) and the Bloch wall (c). The cross tie wall (d) contains a chain of vortices and antivortices. The centers of a vortex and an antivortex are indicated by the red (gray) arrows in (d).

of vortices and antivortices, as shown in Fig.1.2(d).

1.3.2 Barkhausen Effect

The simplest type of domain-wall dynamics is continuous motion with a fixed internal structure. For example, for the domain walls shown in Fig.1.2(b)-(d), applying a magnetic field along the positive y direction will make the domain on the left of the domain wall expand, resulting in domain-wall motion in the positive x direction. For a homogeneous material (without defects), domain-wall motion is continuous, with a domain-wall velocity v_{DW} determined by the intrinsic damping and the excitation. The value of v_{DW} will be discussed in detail in Sec. 1.3.3.

In a real material, domain-wall motion is generally discontinuous and stochastic, caused by pinning defects in the material. The avalanche of domain-wall motion is usually referred to as the Barkhausen effect [26–29]. Contemporary investigations of Barkhausen phenomena are primarily concerned with universal (sample-independent) behavior in which the jump size of domain-wall motion exhibits power law behavior

$$P(s) \propto b^{-\eta}, \tag{1.9}$$

where the probability of the occurrence of a jump scales inversely with the jump size b. The critical exponent η determines the universality class. Further discussions of the universality class can be found in references [30–37].

As an example, Fig. 1.3 shows a direct observation of the Barkhausen avalanche by Kim *et al.* [37]. They measured the domain-evolution patterns of a Co film for six times on the same 400×320 μm^2 area, as shown for the six images in Fig. 1.3. In each image, a single domain wall moves from the left to the right of the image as a function of time. The domain wall positions are at the boundaries of the regions with different colors. The positions of the domain wall are discrete because pinning defects trap the domain wall. The domain wall remains static at each position for several seconds, as indicated by the color code for each position, and then the domain wall moves to the next position. The transient motion

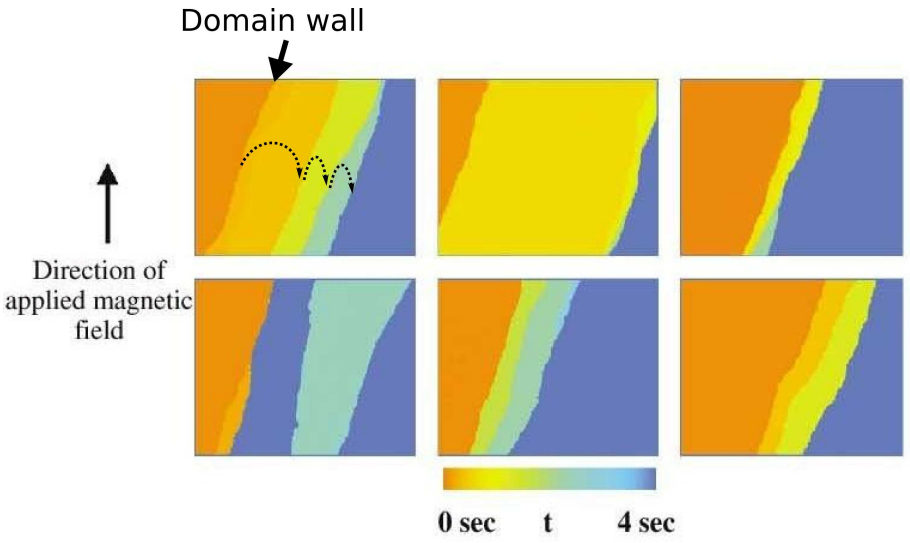

Figure 1.3: A series of six images showing avalanches of the domain structure captured for six experiments on the same 400 × 320 μm^2 area of a 20 nm thick Co film. The sample was saturated downward first, and then a constant field was applied upward as indicated. For each image, the successive positions of a single domain wall are indicated by the boundaries of the regions with different colors. The initial position of the domain wall is at the first boundary from the left. For example, the solid arrow of the first image indicates the initial position of the domain wall for the first experiment. The domain wall stays at each position for some time and then moves to the next position, as illustrated by the dashed arrows in the first image. The color code represents the elapsed time from 0 to 4 sec for the domain wall to stay at each position. Reprinted from Ref. [37] with permission from the APS.

between the indicated domain-wall positions is not shown because the elapsed time between those positions is much smaller than 1 sec.

The experimental results of Fig. 1.3 demonstrate three characteristics of domain-wall pinning. First, the data in each image show that a domain wall moves discontinuously in the presence of pinning. Second, the discontinuous motion is random for each time when the measurement was taken, as shown by the differences of the six images. Third, the domain wall interacts with multiple pinning defects, which are randomly distributed in the material, resulting in the bending of the domain wall. Because of these three characteristics, it is practically impossible to characterize an individual pinning defect from the behavior of a domain wall in an extended film. Consequently, the microscopic pinning mechanisms of domain walls remain largely mysterious in all ferromagnetic materials. I will show in Ch. 3 and 4 that, in contrast to domain-wall pinning, vortex pinning can be characterized quantitatively for each individual pinning site.

1.3.3 Dynamic Regimes of Magnetic Domain Walls

In the presence of pinning, domain-wall motion shows multiple dynamic regimes, as illustrated in Fig. 1.4. The velocity of domain-wall motion depends on the strength of the driving force F, which is induced by an applied magnetic field or spin-polarized current. When F acting on the wall is below a characteristic depinning threshold F_{dep}, the domain wall is trapped by defects. As F increases, so that $F > F_{dep}$, a depinning transition occurs. If the temperature $T > 0$, the depinning transition is smeared, and the domain wall enters a thermally activated creep regime at the depinning region [30, 38–44]. Above the pinned (creep) regime, the domain-wall velocity v_{DW} increases linearly with increasing F [45–47]. As the driving force increases further, above a critical force F_W, the corresponding magnetization dynamics become highly non-linear, and domain-wall motion is accompanied by internal excitations [45, 48, 49]. The internal excitations cause v_{DW} to decrease from its maximum value at F_W, and the drop of v_{DW} in this

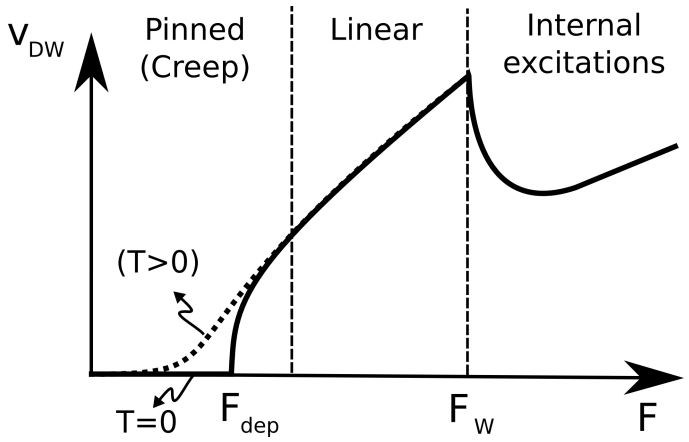

Figure 1.4: Schematic of the domain-wall velocity v_{DW} as a function of the applied force F. Three dynamic regimes are separated by the vertical dashed lines. The solid and dotted curves correspond to the cases of zero temperature ($T = 0$) and non-zero temperature ($T > 0$) respectively.

regime is referred to as Walker breakdown [45].

The domain-wall velocity in the creep and linear regimes is relatively well-understood compared to that of Walker breakdown, which remains controversial. The creep motion has been described by a theory of a 1D interface moving in a 2D weakly disordered medium. The velocity-field relationship is given by [38]:

$$v_{DW} = v_0 \exp\left[-\left(\frac{T_{dep}}{T}\right)\left(\frac{F_{dep}}{F}\right)^{\mu}\right]. \tag{1.10}$$

The depinning temperature T_{dep} is given by U_C/k_B, where U_c is related to the height of the defect-induced pinning energy barrier. μ is a universal dynamic exponent equal to 1/4 for a 1D interface moving in a 2D weakly disordered medium [38]. Eq. 1.10 has been confirmed by a recent experiment [39].

In the linear dynamics regime, v_{DW} is determined by the dissipation, which can be characterized by a Gilbert Damping constant α. When the domain wall is driven by a magnetic field H, v_{DW} is given by [45, 46]:

$$v_{DW} = mH, \tag{1.11}$$

where $m = \gamma L_{DW}/\alpha$ is the wall mobility. In $Ni_{80}Fe_{20}$ $m \sim 10$ m/sec Oe, which

is consistent with the experimental results observed in films [50] and nanowires [48, 49].

A simple model has been developed to describe the onset of the Walker breakdown by treating the domain wall in 1D (for a review, see Ref. [6]). The model explains the existence of F_W, below which the shape of the domain wall remains rigid. Above F_W, the domain wall starts to precess and the internal excitations occur. The predicted value of F_W, however, is at least a factor of 10 larger than the experimental values of F_W. Furthermore, the 1D model fails to describe the microscopic behavior of the domian wall in this regime. The microscopic behavior remains unclear because of the lack of tools to probe the microstructure of the domain wall with sufficient temporal and spatial resolution.

It should be noted that, although the transitions between the three regimes have been observed in films [39, 50] or nanowires [48, 49], it has been difficult to capture all of these regimes in a single quantitative experiment because of the large dynamic range covered by these phenomena as well as the spatially extended nature of domain walls.

1.3.4 Pinning Mechanisms of Magnetic Domain Walls

Another challenge is to identify the microscopic mechanisms of the domain-wall pinning. Pinning is usually attributed to the interactions between the domain structure and local fluctuations of magnetic properties due to defects. Possible sources of defects in polycrystalline ferromagnets include point defects (e.g., impurities, vacancies, and nonmagnetic inclusions), line defects (e.g., dislocations), surface imperfections (e.g., roughness), and random anisotropies. Because multiple types of defects coexist in a given material, it is problematic to identify exactly which ones dominate the pinning process. It has been practically impossible to identify an individual pinning site, and therefore studies of domain wall pinning have focused on collective effects [51–54]. For example, Li *et al.* [54] reported a correlation between the surface roughness and the coercivity (i.e., the half-width

of the magnetic hysteresis loop) from a series of Co films, implying that the pinning of domain walls is stronger in rougher films. The approaches of studying the collective effects, however, are not adequate for applications of domain wall-based devices, such as domain-wall logic [55] and domain-wall memory [56, 57], in which pinning must be precisely engineered .

1.4 Dynamics of Magnetic Vortices in the Presence of Pinning

In Sec. 1.3, I discussed the difficulties in investigating the pinning of domain walls. An alternative approach is to study pinning in simple, albeit non-uniform magnetic structures, where an individual pinning site can be readily identified. In this section, I will focus on a single magnetic vortex, which is the simplest realization of a non-uniform domain structure. I will discuss the structure and the dynamics of a single magnetic vortex. I will also discuss the recent experimental studies of vortex pinning at the end of this section.

1.4.1 Magnetic Vortex

A magnetic vortex is often the ground state of soft ferromagnetic disks with thicknesses on the order of 10 nm and diameters on the order of 1 μm. Although the magnetization circulates in the bulk of the disk, the most significant feature of a vortex is a core of diameter $\sim$ 10 nm, within which the magnetization rotates out of the disk plane, as shown schematically in Fig. 1.5(b).

In 1990, Aharoni and Amikam [59] first hypothesized the magneitzation distribution for the vortex state, which was later derived by Usov and Peschany [60] using a variational principle. A intuitive way to understand the vortex state is that, starting from the edge of of the disk, the magnetization follows the circular shape of the disk to minimize the magnetostatic energy. The central point of the disk corresponds to a topological defect, at which the large magnetization

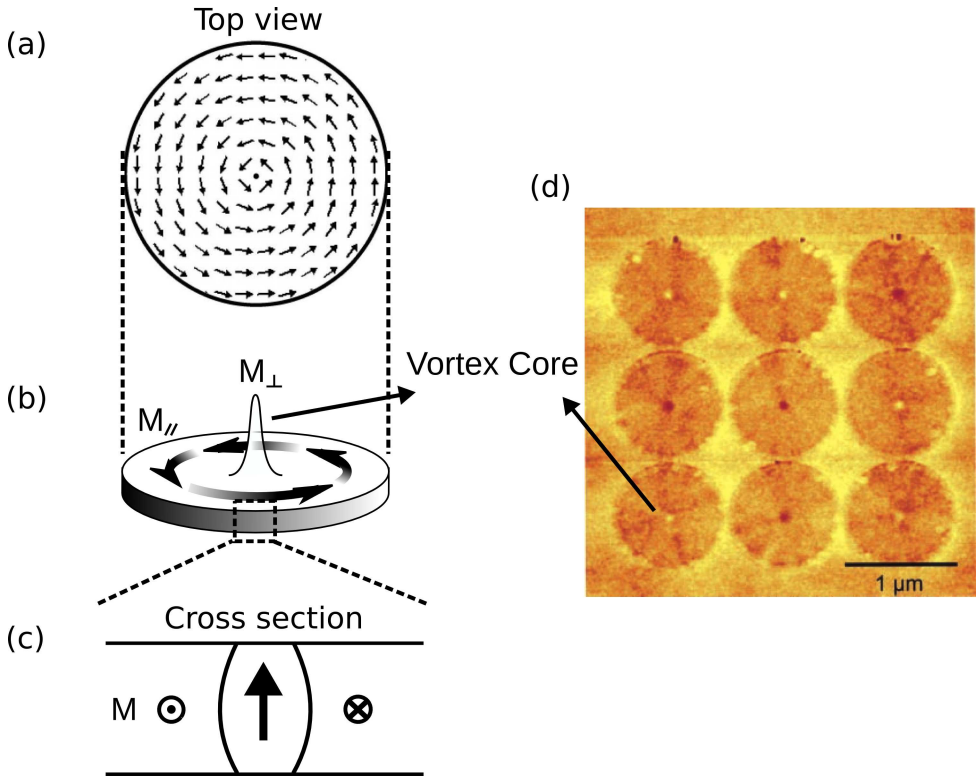

Figure 1.5: (a) The ground state configuration of the magnetization of a magnetic disk 1 μm in diameter and 50 nm in thickness. Data were obtained from a 2D micromagnetic simulation with a cell size of $5\times5\times50$ nm^3. The arrows in the disk indicate the in-plane component of the magnetization. (b) Schematic representation of a magnetic vortex. (c) Schematic representation of the vortex core seen from the cross section of the disk. (d) Magnetic force microscopy (MFM) image of an array of $Ni_{80}Fe_{20}$ disks with 1 μm in diameter and 50 nm in thickness. MFM images shows contrast at the disk centers due to the interaction between the magnetized tip and the vortex core. The black and white colors correspond to the core polarity $P = \pm1$ respectively. Reprinted from Ref. [58] with permission from the AAAS.

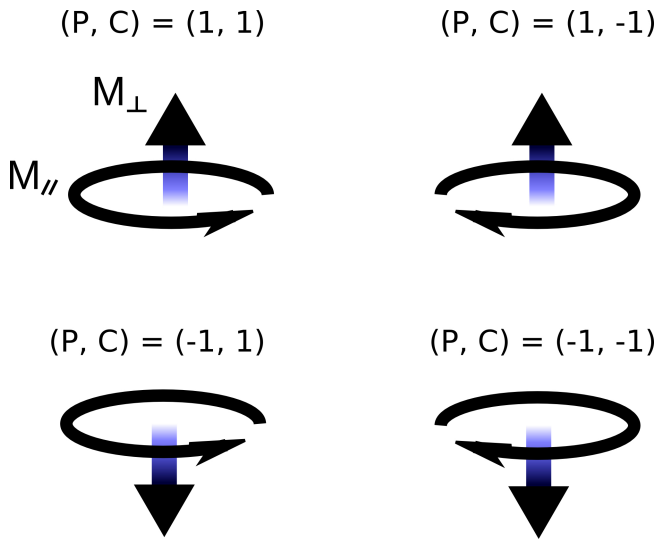

Figure 1.6: Four different combinations of (P, C), where P is the polarity and C the chirality, representing four different vortex states.

gradient associated with the circulated magnetization would cause the exchange energy to diverge. Consequently, the magnetization rotates out of the plane only within the vortex core to avoid the energy divergence. The radius of the vortex core is determined by minimizing the sum of the magnetostatic energy (Eq. 1.3) and the exchange energy (Eq. 1.1). Recall from Sec. 1.1.3 that the length scale associated with competition of the magnetostatic energy and the exchange energy in thin films is the exchange length. Similar to the exchange length, the radius of the vortex core is typically on the order of 10 nm.

In 2000, Raabe *et al.* [61] reported the first direct evidence for the vortex state, showing the in-plane circular magnetization by using Lorentz electron microscopy. In the same year, Shinjo et al. [58] showed the first direct observation of a vortex core by using magnetic force microscopy (MFM), as can be seen in Fig. 1.5(d).

A single magnetic vortex can be described by two topological quantities: the polarity P and the chirality C. The polarity describes the magnetization direction of the vortex core, and the chirality corresponds to the winding direction of in-plane magnetization. There are four different possible ground states denoted by

combinations of (P,C), as shown in Fig. 1.6. The degeneracy with respect to the polarity allows the gyrotropic motion of the vortex core to have two degenerate modes, as will be discussed in Sec. 1.4.4.

1.4.2 Diameter of the Vortex Core

The diameter of the vortex core is smaller at the surface of disk than in the equatorial plane of the disk, as shown schematically in Fig. 1.5(c). This barrel shape of the vortex core was predicted by theory [62] and by micromagnetic simulations [63]. The diameter of the core will be important for the discussions of vortex pinning in Ch. 4 because the core diameter at the surface determines the lateral pinning range for a magnetic vortex.

In the following I will discuss the core diameter by using quasi-3D micromagnetic simulations. A 1 μm diameter disk is divided into cells of a size of 5×5×s nm^3, where $s = L/5$ is the dimension of the cell along the normal axis of the disk and L is the thickness of the disk. It is quasi-3D because s scales with L, rather than a constant 5 nm for 3D simulations. The quasi-3D simulations are more efficient than the 3D simulations in terms of computation time, especially when simulating magnetization dynamics. Fig.1.7(a) shows a micromagnetic simulation of a core profile at the surface of the disk, obtained from the magnetization of the top (or the bottom) layer of the cells. I will define the diameter of the core as the distance between the peaks of the first derivative of the profile, which is shown in Fig. 1.7(b). Fig. 1.7(c) shows the simulated core diameters at the surface and in the equatorial plane of the disk as a function of L. Although both diameters increase with increasing L, the diameter at the surface is less sensitive to L compared to that in the equatorial plane. I will show in Ch. 4 that the thickness dependence of the core diameter at the surface matches the thickness dependence of the pinning range.

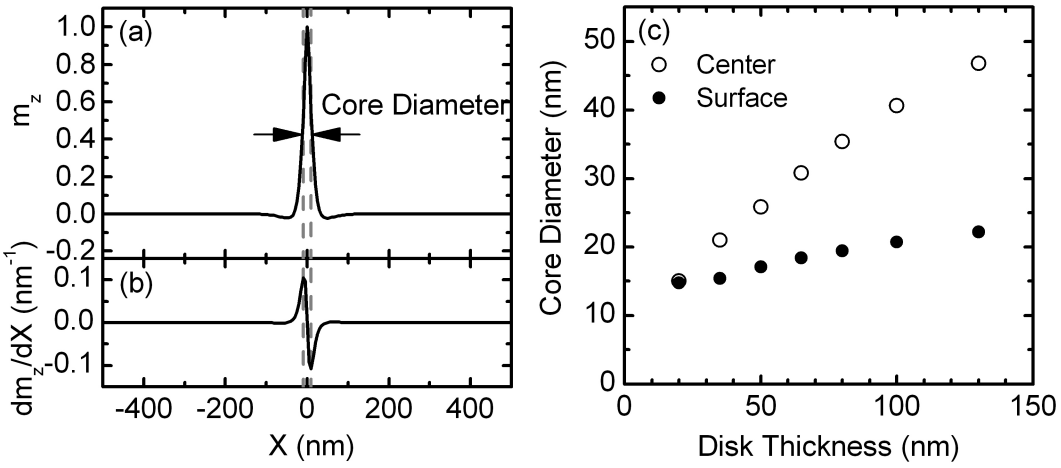

Figure 1.7: (a) The computed profile of vortex core, i.e., the z-component of the magnetization ($m_z \equiv M_z/M_s$), determined from a quasi-3D micromagnetic simulation of a 1 μm diameter disk with a thickness of 50 nm. The core profile shown in (a) is for the surface layer of the disk. (b) The first derivative of the core profile. The dashed lines indicate the positions of the extrema of the first derivative, providing the core diameter as indicated by the arrows in in (a). (c) The core diameter as a function of the disk thickness. The filled circles indicate the core diameter at the surface of the disk and the open circles indicate the core diameter in the equatorial plane of the disk.

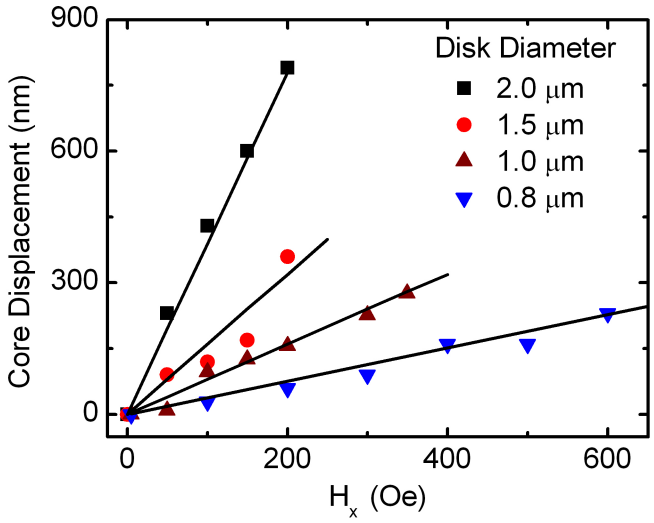

Figure 1.8: (a) Displacement of the vortex core versus field for four 50 nm thick disks with different diameters. Displacements are relative to the zero field core positions.

1.4.3 Displacement Susceptibility of the Vortex Core

The vortex core is located at the center of the disk unless an in-plane magnetic field is applied. The applied field moves the core in the direction perpendicular to the field direction [64]. The new equilibrium position is determined by the balance between the Zeeman and magnetostatic energies of the disk. For example, Fig. 1.8 shows the field dependence of the displacement of the core, measured using time-resolved Kerr microscopy (TRKM), which will be described in Ch. 2. In the field range shown, the measured displacement Y is linear with field H_x. Linear fits to the displacement curves give the displacement susceptibility $\chi_Y = dY/dH_x$. Typical values are $\chi_Y = 4.5 \pm 0.3$ nm/Oe for a 2 μm disk and 0.9 ± 0.2 nm/Oe for a 1 μm disk. In comparison, micromagnetic simulations give 3.9 and 1.1 nm/Oe respectively.

The position of the vortex core can be controlled in two dimensions within the disk by combining two orthogonal fields. In my experiment, this approach allows me to move the core repeatedly to the same position with a resolution of ~ 5 nm

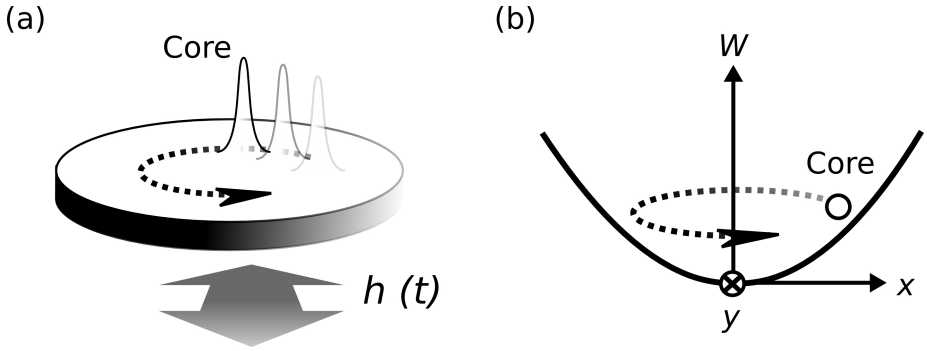

Figure 1.9: (a) Schematic representation of the gyrotropic mode of a magnetic vortex. The gyrotropic mode can be excited by applying an in-plane oriented magnetic field $h(t)$. (b) Cartoon of the potential well with magnetostatic energy W expanded to second order in vortex-core displacement. The dashed arrows in (a) and (b) indicate the orbital motion of the vortex core.

[65, 66]. As will discussed in Ch. 3 and Ch. 4, controlling the core position is crucial for studying the properties of localized pinning sites.

1.4.4 Gyrotropic Mode

Regarding the dynamics of a magnetic vortex, in this dissertation I will focus on the lowest frequency excitation of a magnetic vortex, i.e., the gyrotropic mode. The higher frequency modes, including the radial and azimuthal spin-wave modes, will not be addressed here and a discussion of them can be found in references [67–69].

In the gyrotropic mode the vortex core circulates around its equilibrium position and the core moves as a particle, as shown schematically in Fig. 1.9. Argyle in 1984 observed the first evidence of the gyrotropic motion of a magnetic vortex using a magneto-optical photomicrographic image [62]. Recently, the gyrotropic motion of a magnetic vortex has been experimentally observed in real time and space using time-resolved Kerr microscopy [64, 65, 67, 69], scanning transmission X-ray microscopy [70–73], and time-resolved photo-emission electron microscopy [74–76]. For a magnetic vortex in a disk, the gyrotropic mode in the linear regime

is well-understood, with experiment, analytical theory, and micromagnetic simulation, all showing that gyrotropic-mode frequency f_G is determined by the geometric aspect ratio (thickness/diameter) of the disk [67, 69, 77, 78]. In the following I will give a brief overview of the analytical calculation, following Guslienko's treatments in references [77, 79].

Thiele in 1973 developed a method to describe the steady-state motion of arbitrary micromagnetic feqaures such as domains and domain walls. Recall from Sec. 1.2.1 that the dynamics of magnetization are governed by the LLG equation (Eq. 1.8), which is a torque equation. On the assumption that a domain or a domain wall moves as a rigid object, Thiele transformed the torque equation (Eq. 1.8) into a force equation, which will be referred to as the Thiele equation:

$$\mathbf{G} \times \frac{d\mathbf{r}}{dt} - D\frac{d\mathbf{r}}{dt} - \frac{\partial W(\mathbf{r})}{\partial \mathbf{r}} = \mathbf{F}(t), \tag{1.12}$$

where

$$\mathbf{G} = -\frac{M_s}{\gamma} \int dr^3\mathbf{r} \left[\nabla\phi \times \nabla\theta\right] \sin\theta \tag{1.13}$$

and

$$\mathbf{D} = -\frac{M_s}{\gamma}\alpha \int dr^3\mathbf{r} \left[\nabla\theta\nabla\theta + \sin^2\theta\nabla\phi\nabla\phi\right]. \tag{1.14}$$

$\mathbf{r}$ is the displacement of the rigid magnetic structure, t is time, θ and ϕ are the polar coordinates of magnetization, W is the potential energy, and $\mathbf{F}$ is the applied force. Detailed derivations of the Thiele equation can be found in references [80, 81].

For the gyrotropic mode of a magnetic vortex, the vortex core moves as a rigid body and its dynamics can be described by the Thiele equation. In a magnetic disk, the majority of the in-plane part of the vortex also moves as a rigid body, along with the core. At the edge of the disk, however, the magnetization tends to align with the circular shape of the disk. To address the boundary condition, Guslienko developed a "two-vortices" model [77, 79], in which the magnetization at the edge of the disk aligns with the circular shape of the

disk, and the corresponding Thiele equation (Eq. 1.12) has the following parameters: $\mathbf{r}$ is the displacement of the vortex core relative to the equilibrium position of the core, $\mathbf{G} = -\pi P L M_s/\gamma \hat{\mathbf{z}}$ is the gyrovector, $D = \alpha\pi M_s L(2 + \ln\frac{R}{R_c})/\gamma$ is the damping constant with $R_c = 0.68{L_{ex}}^{2/3}L^{1/3}$, W is the potential energy, $\mathbf{F}(t) = (\xi\pi M_s L R)\mathbf{h}(t) \times \hat{\mathbf{z}}$ is the time dependent excitation force, and $\xi = 2/3$ is a model-dependent constant. The parameter $p = \pm 1$ is the vortex polarization, L is the disk thickness, R is the disk radius, and $\mathbf{h}(t)$ is the excitation field.

Eq. 1.12 can be solved numerically for general forms of W and $\mathbf{F}$, as will be discussed in Ch. 3. In the following I will consider a simple case, in which Eq. 1.12 can be solved analytically. When the vortex core is near the center of the disk, W can be approximated as a parabolic potential:

$$W = \frac{1}{2}kr^2, \tag{1.15}$$

where the curvature of the potential is $k = 9.98(\xi M_s L)^2\pi/R$ obtained from the "two-vortices" model. On the assumption that $F = 0$, solving Eq. 1.12 and Eq. 1.15 leads to two solutions, which are the clockwise and counterclockwise orbital motions of the core, with the gyrotropic mode frequency f_G given by [77, 82]:

$$f_G = \pm\frac{kG}{2\pi(G^2 + D^2)}, \tag{1.16}$$

where the positive sign is for the clockwise mode and the negative sign is for the counterclockwise mode. It should be noted that the polarity of the core $P = \pm 1$ determines the sign of G. For the case of $P = 1$, the clockwise mode has a negative f_G and the counterclockwise mode has a positive f_G. In other words, if $P = 1$ a counterclockwise-circular-polarized excitation force F at f_G drives the counterclockwise mode on resonance, but clockwise-circular-polarized F will not drive the clockwise mode on resonance. This asymmetric resonance is caused by the gyroforce $\mathbf{G} \times d\mathbf{r}/(dt)$ in Eq. 1.12. As will be discussed in Sec. 3.1.2, a reliable way to determine the polarity of a vortex core is to measure the direction of the core gyration.

Fig. 1.10(a) shows a schematic representation of the gyrotropic mode spectra for the case of $P = 1$. A clockwise-circular-polarized force can excite the clockwise mode with response power r_{CW}^2, as indicated by the red curve. A counterclockwise-circular-polarized force can excite the conterclockwise-mode with response r_{CCW}^2, as indicated by the blue curve.

The asymmetric resonance results in interesting orbital shapes when excited by a linearly polarized force F_{lin}, as was first pointed out by Lee *et al.* [82]. Fig. 1.10(b)-(d) show schematically the orbits excited by F_{lin}, which is along the x axis. The projections of F_{lin} in the circular coordinate contain two components F_{CW} and F_{CCW}, which excite $\mathbf{r}_{CW}$, as indicated by the red orbits, and $\mathbf{r}_{CCW}$, as indicated by the blue orbits, respectively. The response of F_{lin} is $\mathbf{r}_{CW} + \mathbf{r}_{CCW}$, as indicated by the black orbit. I will assume that F_{lin} is a sine wave at frequency f. For the case of $f = f_G$ [Fig. 1.10(b)], the excited r_{CCW}^2 is much larger than r_{CW}^2, as can be seen from the spectra [Fig. 1.10(a)], resulting in an elliptical orbit of $\mathbf{r}_{CW} + \mathbf{r}_{CCW}$ with very low ellipticity. In this case, the phase difference δ between $\mathbf{r}_{CW}$ and $\mathbf{r}_{CCW}$ is close to $\pi/2$, as indicated by the core positions (black filled circles) at a given time. For the case of $f < f_G$ [Fig. 1.10(c)], the amplitude difference between $\mathbf{r}_{CCW}$ and $\mathbf{r}_{CW}$ becomes smaller, with $\delta \sim \pi$, resulting in an elliptical orbit of $\mathbf{r}_{CW} + \mathbf{r}_{CCW}$ with the long axis along the x axis. For the case of $f > f_G$ [Fig. 1.10(d)], $\delta \sim 0$, resulting an elliptical orbit of $\mathbf{r}_{CW} + \mathbf{r}_{CCW}$ with the long axis along the y axis.

Although the ellipticity of the orbits are difficult to detect in experiment due to the small ellipticity for f close to the resonance, the elliptical orbits will be emphasized for the case of numerical calculations in Sec. 3.1.5.

.

1.4.5 Large Amplitude Regime

Several groups have reported that the experimental results of f_G are in consistent with the prediction of the "two-vortices" model (Eq. 1.16) [67, 69, 77, 78]. These

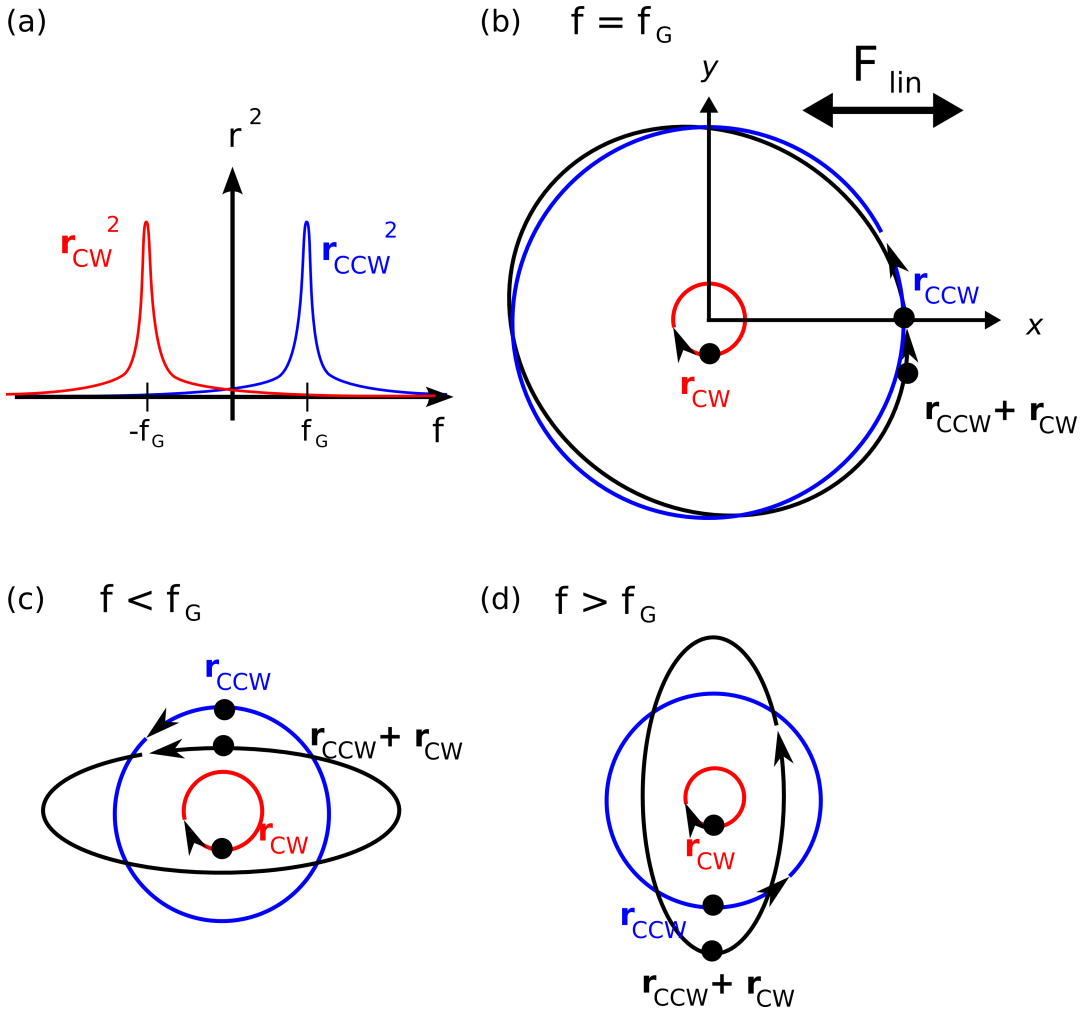

Figure 1.10: (a) Schematic of the gyrotropic mode spectra for the case of core polarity $P = 1$. The red curve indicates the spectrum of r_{CW}^2 as a function of excitation frequency f, where r_{CW} is the amplitude of the clockwise gyration. The blue curve indicates the spectrum of r_{CCW}^2, where r_{CCW} is the amplitude of the counterclockwise gyration. (b)-(d) Schematic of vortex-core orbits for the cases of (b) $f = f_G$, (c) $0 < f < f_G$, and (d) $f > f_G$. The black filled circle on each orbit represents the core position. The red and blue open circles represent the orbits of clockwise gyration $\mathbf{r}_{CW}$ and counterclockwise gyration $\mathbf{r}_{CCW}$. The black open ellipses represent the gyration of $\mathbf{r}_{CW} + \mathbf{r}_{CCW}$, which can be excited by the linear-polarized force F_{lin}. The amplitude of $\mathbf{r}_{CCW}$ at $f = f_G$ is much larger than those at $f < f_G$ and $f > f_G$. The amplitude of $\mathbf{r}_{CW}$ decreases with increasing f. In this case F_{lin} is along the x axis as indicated by an arrow in (b).

experimental results correspond to the cases of linear vortex dynamics, as I will discuss in Ch. 3. As noted earlier, non-linear vortex dynamics occur at large amplitude. First, as the amplitude of vortex motion increases, higher order terms in W of Eq. 1.12 need to be considered [83, 84]. For example, Buchanan *et al.* [83] measured the gyrotropic mode spectra for a vortex in circular and elliptical disks, and they showed that the spectral line-shape is asymmetric at high excitation powers, indicating that the non-linear dynamics are caused by anharmonic W.

As the core velocity increases further, the assumption of a rigid vortex core breaks down. Internal excitations of the vortex core occur in this dynamics regime, similar to the Walker breakdown of a domain wall under strong excitations (Sec. 1.3.3). For example, Vansteenkiste *et al.* observed directly that the vortex core deforms under strong excitations [72], and several groups observed that the vortex core reverses its polarity under strong excitation [71, 73, 85, 86]. I will discuss the reversal of the core polarity in more detail in Ch. 3.

1.4.6 Pinning of Magnetic Vortices

Alongside the non-linear effects discussed above, vortex dynamics are profoundly affected by pinning defects in the material. For example, pinning defects cause discontinuous vortex motion as a function of the applied magnetic field, as was first observed by Uhlig *et al.* [87]. Additionally, when a vortex is pinned by a defect, f_G increases significantly from the predicted value of Eq. 1.16, as was first observed by Compton and Crowell [65].

Because the magnitude of f_G reveals whether the vortex core is pinned, spatial distributions of pinning defects can be determined by measuring f_G at different core positions. For example, Fig. 1.11(a) shows f_G as a function of the orthogonal in-plane-oriented magnetic fields, revealing the map of spatial distribution of pinning defects in a 80 nm $\times$ 80 nm spatial range. The experimental technique used in Fig. 1.11(a) will be discussed in more detail in Ch. 2.

The fluctuations of f_G due to pinning [Fig. 1.11(a)] suggest the existence of

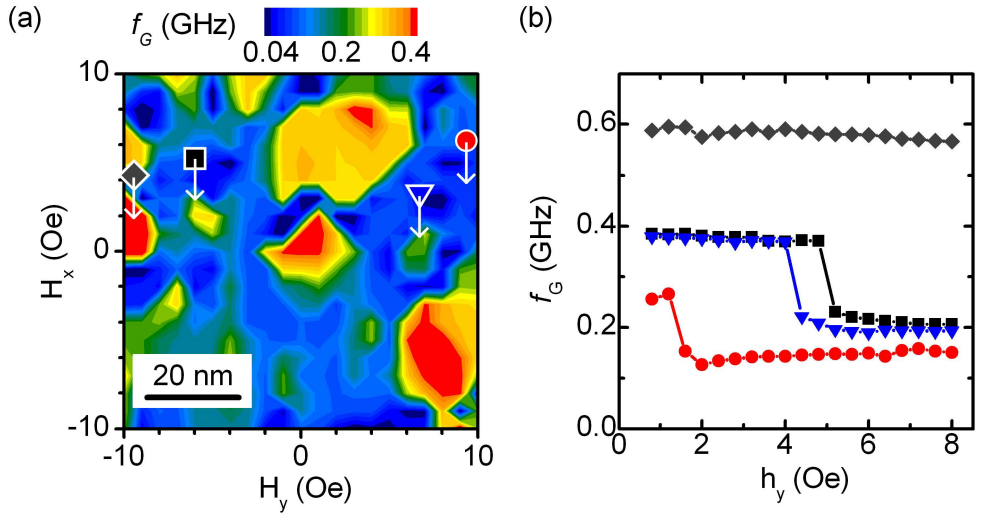

Figure 1.11: (a) Contour map of the gyrotropic frequency f_G as a function of static field applied along both in-plane directions for a 2 μm diameter disk. Data were obtained at a pulse amplitude of $h_y \sim 6$ Oe. (b) Gyrotropic frequency versus the amplitude h_y of the excitation pulse. Data were obtained at fixed locations in field space, as indicated by the symbols shown in (a).

a *depinning threshold* for a given position of the vortex core. Indeed, when f_G was measured as a function of the pulse amplitude at different core locations, f_G showed transitions from high to low values with increasing amplitude, as shown in Fig. 1.11(b). The transition field for the data indicated by the circles is only $\sim$ 1 Oe. For this location, indicated by the circle in Fig. 1.11(a), the vortex core is already depinned, since the pulse amplitude used to obtain the data of Fig. 1.11(a) is $\sim$ 6 Oe. On the other hand, for the frequency peak that is indicated by the diamonds in Fig. 1.11(a), no corresponding depinning transition was observed in Fig. 1.11(b). In this case the largest excitation amplitude achievable is smaller than the depinning field.

The observations of Fig. 1.11 suggest that a pinning defect induces a pinning potential, which locally confines the vortex core. At low excitation amplitude, the vortex core remains within the range of the pinning site. As the amplitude of the excitation increases, so does the radius of the orbit of the core about its equilibrium position. When the radius of the core's orbit exceeds the range of the pinning potential, the core is depinned and f_G decreases to the frequency predicted by the analytical model of the gyrotropic mode. I will discuss in detail the form of a pinning potential in Ch. 3.

1.4.7 Research Questions

(1) How does a defect affect the dynamics of a magnetic vortex? In Sec. 1.4.6, I maintained that the observation of enhancement of f_G implies the existence of localized pinning potentials. Quantitative determinations of the pinning potentials are needed to fully understand how defects affect the dynamics of a magnetic vortex. Although the experimental results shown in Fig. 1.11 revealed the depinning transition, the large bandwidth of the pulsed excitation made it difficult to interpret the transition and the subsequent dynamics. The ideal probe would address the response of a single vortex as a function of amplitude and frequency, with an amplitude range extending from the pinned regime up through

the threshold for core reversal. I have developed a set of new measurement techniques to achieve this goal, as will be discussed in Ch. 2. I will show in Ch. 3 that my approach allows for a highly quantitative analysis of the pinning potential. I will also show that the new approach can also be used to trace the dynamics of a single vortex from deep in the pinning regime to the onset of core reversal, showing a global phase diagram of vortex dynamics in the presence of pinning.

(2) What is the pinning mechanism? The microscopic mechanism of vortex pinning remains largely mysterious not only for $Ni_{80}Fe_{20}$, but also for all ferromagnetic materials. It is clear, however, that pinning of a single vortex can in fact be probed via vortex dynamics (Sec. 1.4.6). I will discuss my research results of the strength and range of pinning sites, which were obtained by measuring the vortex dynamics of disks with different thicknesses. As will be shown in Ch. 4, my experimental results indicate that the dominant source of pinning mechanism for a single $Ni_{80}Fe_{20}$ vortex is the surface roughness on the length scale of the vortex-core diameter.

(3) Where does the 2D-3D crossover of vortex dynamics occur? The vortex dynamics discussed thus far in this chapter are for vortices in thin disks ($L << R$). In the thin-disk limit the vortex structure can be treated in 2D. For sufficiently thick disks the 2D model must break down. In Ch. 5 I will discuss my research of the dimensional crossover of the vortex dynamics. Experimental results and simulations indicate that there are two gyrotropic modes which crossover at a critical thickness. Besides the original gyrotropic mode which can be described by the 2D model (Sec. 1.4.4), the second gyrotropic mode is associated with the distortion of the vortex core along the normal axis of the disk.

Chapter 2

Design and Methodology

This chapter will describe the experimental methodology, including two parts. The first part will discuss the preparation process of samples, including the deposition of $Ni_{80}Fe_{20}$ films and the lithography of micron-sized disks. The second part will discuss time-resolved Kerr microscopy (TRKM).

2.1 Sample Preparation

2.1.1 Sputtering of Magnetic Thin Films

Thirteen samples will be discussed in this dissertation, with the growth parameters given in Table 2.1. Samples 1 to 10 have the same deposition parameters except the thickness of the films, and they were prepared for studying the thickness dependence of vortex pinning and the dimensional crossover of vortex dynamics. Polycrystalline $Ni_{80}Fe_{20}$ films were grown on Si substrates with a SiN buffer layer by dc magnetron sputtering at 100 W (1 A/s) in 2.5 mTorr Ar, at ambient temperature (RT). The film thicknesses are 20, 35, 50, 65, 80, 100, 130, 160, 200, and 300 nm. Fig. 2.1 shows representative atomic force microscopy (AFM) images, which reveal the surface morphology of the films. The surface roughness and the grain size increase with the thickness of the film, as is typical. A detailed analysis

Sample	Substrate	Material	Thickness	Temp.	Rate
1	Si/SiN	$Ni_{80}Fe_{20}$	20 nm	RT	1 A/s
2	Si/SiN	$Ni_{80}Fe_{20}$	35 nm	RT	1 A/s
3	Si/SiN	$Ni_{80}Fe_{20}$	50 nm	RT	1 A/s
4	Si/SiN	$Ni_{80}Fe_{20}$	65 nm	RT	1 A/s
5	Si/SiN	$Ni_{80}Fe_{20}$	80 nm	RT	1 A/s
6	Si/SiN	$Ni_{80}Fe_{20}$	100 nm	RT	1 A/s
7	Si/SiN	$Ni_{80}Fe_{20}$	130 nm	RT	1 A/s
8	Si/SiN	$Ni_{80}Fe_{20}$	160 nm	RT	1 A/s
9	Si/SiN	$Ni_{80}Fe_{20}$	200 nm	RT	1 A/s
10	Si/SiN	$Ni_{80}Fe_{20}$	300 nm	RT	1 A/s
11	Si/SiN	$Ni_{80}Fe_{20}$	50 nm	RT	1 A/s
12	Al_2O_3	Cu	30 nm	RT	2 A/s
		$Ni_{80}Fe_{20}$	50 nm		1 A/s
13	Al_2O_3	Cu	30 nm	250 C	2 A/s
		$Ni_{80}Fe_{20}$	50 nm		1 A/s

Table 2.1: Growth parameters for thin $Ni_{80}Fe_{20}$ films.

of the surface roughness will be given in Sec. 4.2.

Sample 11 has the same thickness (50 nm) as sample 3, but it has smaller roughness. (Sample 11 was obtained from a different deposition run.) For samples 12 and 13, polycrystalline $Ni_{80}Fe_{20}$ films were grown on sapphire (Al_2O_3) substrates with a Cu buffer by dc magnetron sputtering at 100 W (1 A/s) in 2.5 mTorr Ar, at either ambient temperature (for sample 12) or at an elevated substrate temperature of 250 C (for sample 13). Because of the elevated substrate temperature, sample 13 has larger grain size ($\sim$ 100 nm) [64] than samples 3, 11, and 12 ($\sim$ 30 nm), although they all have the same thickness. This can be clearly seen from the AFM images (Fig. 2.1).

For all samples, a capping layer of Al (2.5 nm thick) was grown on top of the $Ni_{80}Fe_{20}$ film with growth rate 0.5 A/s. The capping layer protects the magnetic films from oxidation.

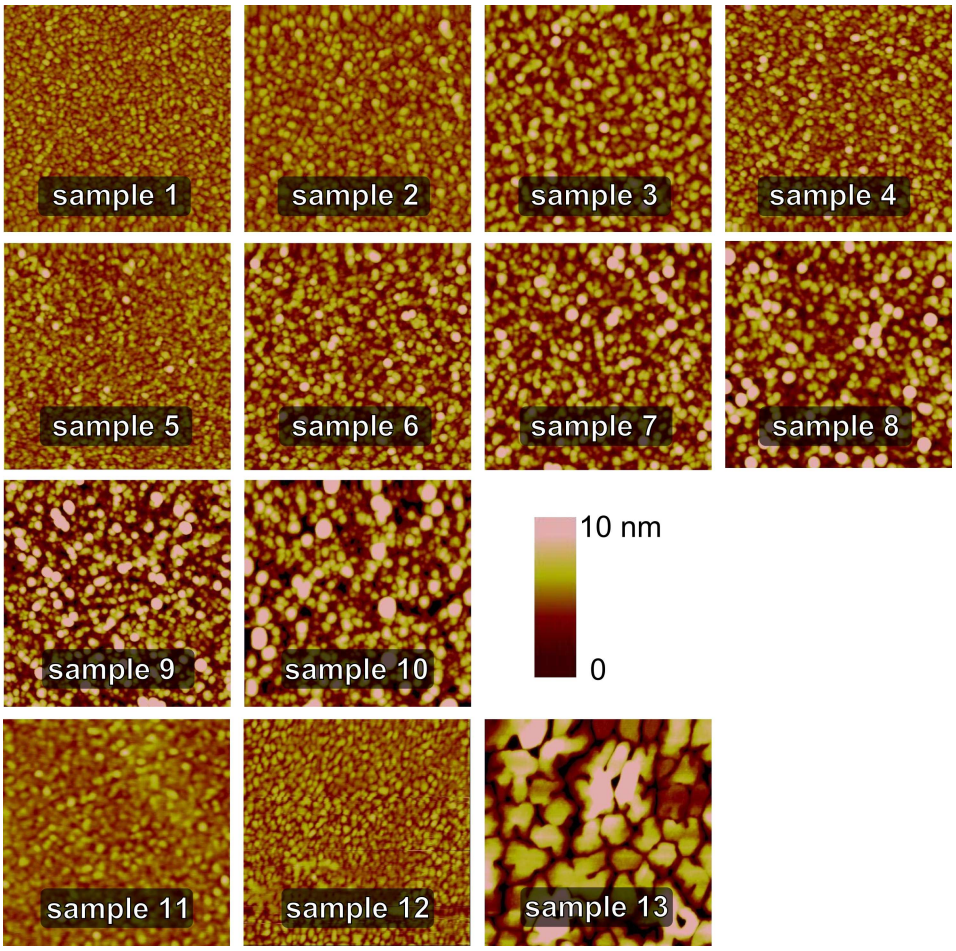

Figure 2.1: Representative atomic force microscopy (AFM) images of the $Ni_{80}Fe_{20}$ films. The lateral scanning range is 1 μm $\times$ 1 μm. The color scale represents the thickness fluctuation from 0 to 10 nm at the surface of the films. Sample numbers correspond to those in Table 2.1

2.1.2 Patterning of Disks

The samples were fabricated by electron beam lithography (EBL) and dry etching at the University of Minnesota Nanofabrication Center. First, EBL patterns were defined in the Graphic Data System (GDSII) format, which were obtained from the drawing package AutoCad. The EBL process we used is a bilayer resist process with polymethylmethacrylate (PMMA) as the imaging layer and polymethylglutarimide (PMGI) as the undercut layer. After the bilayer resist was spin-coated on $Ni_{80}Fe_{20}$ films, the patterns were written on the resist using either the Raith 150 EBL system (for samples 1, 2, 4–6, 11–13) or the Vistec EBPG5000+ EBL system (for samples 3, 7–10). Both of the EBL systems provide similar results for the patterns used in this dissertation. Following exposure in the EBL system, the resist is developed in two steps to obtain the image mask (PMMA) and the undercut (PMGI). After the resist was developed into disk patterns, one of the two following dry-etching processes can be applied, both providing similar results.

The first dry-etching process was used for samples 1–11. A 70 nm layer of Ti was deposited on the bilayer resist and the resist was lifted off, resulting in a layer of Ti disks as a hard mask. Next, the disk patterns were transferred from the Ti layer into the permalloy layer by Ar ion milling. Finally, the Ti mask was removed by fluorine-based reactive ion etching.

The second dry-etching process was used for samples 12 and 13. A 50 nm layer of SiN was reactively sputtered onto the permalloy film before the bilayer resist was spin-coated. After the resist was developed into disk patterns, a 50 nm layer of Al was deposited through the resist to form disks. The resist was then lifted off. The disk patterns were then transferred from the Al layer into the SiN layer by fluorine-based reactive ion etching. Finally, the SiN mask pattern was transferred to the permalloy layer by Ar ion milling.

A representative scanning electron microscopy (SEM) image of the patterned $Ni_{80}Fe_{20}$ disk is shown in Fig. 2.2. The fabrication process described above is a "top-down" method, and it has the advantage of compatibility with any deposition technique and substrate, because the deposition is done prior to the EBL. The

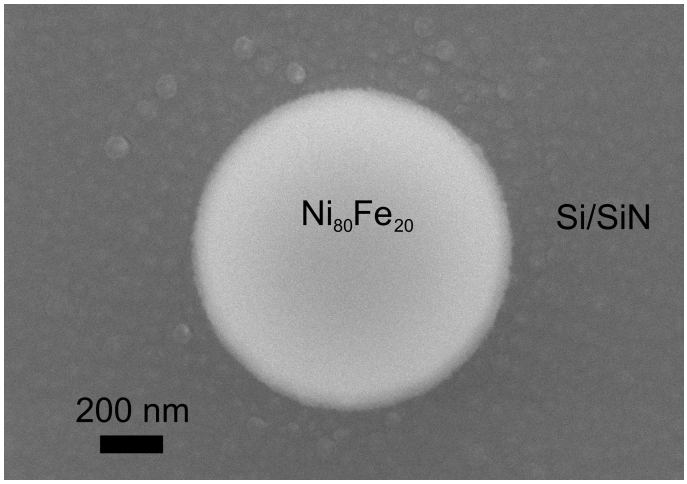

Figure 2.2: Representative scanning electron microscopy (SEM) image of a 1 μm diameter $Ni_{80}Fe_{20}$ disk (sample 11).

opposite method (not described in this dissertation) is usually referred to as "lift-off", in which films are deposited on the substrates with EBL resist patterns.

2.2 Time-Resolved Kerr Microscopy

Time-resolved Kerr Microscopy (TRKM) [88] is the main experimental technique used in this dissertation. TRKM is based on the magneto-optical Kerr effect, which is the rotation of the polarization of light reflected by a magnetic material. To achieve temporal resolution (<1 ns), TRKM is a pump-probe technique that is sensitive to magnetization changes that are induced by magnetic field excitations. The polar Kerr signal θ_{Kerr} is acquired stroboscopically in a manner similar to a sampling oscilloscope. Purely stochastic effects are therefore averaged out. The laser beam is focused into a 400 nm diameter spot. When the focused laser light scans across a sample, it can provide images of the pump-induced change in the z-component of the magnetization of the sample.

The TRKM setup described in the following is an upgraded version of former graduate students' work. Details of the original setup can be found in the theses

of Johoo Park [89] and Rob Compton [66]. The original excitation approach of TRKM is pulsed magnetic fields. I have worked with Paul Crowell and Andrew Galkiewicz to upgrade the experimental setup, and we have recently developed three additional types of excitation approaches. The following will discuss the working principles, the most essential components, and some typical data of these four approaches.

2.2.1 Overview

Fig. 2.3 shows a schematic diagram of the TRKM setup. A Ti:Sapphire laser (Coherent Mira-107661) produces a 76 MHz optical pulse train with wavelength $\lambda = 810$ nm. The repetition rate of the pulses is reduced to f_0 by a pulse picker (Conoptics 350). The laser beam is split into pump and probe beams. To obtain a polar Kerr signal, which is sensitive to the z-component of the magnetization of the sample, the probe beam is linearly polarized, and it is focused through an oil immersion objective (Nikon CFI-P-100X) to a spot with a full width at half maximum (FWHM) $\sim$ 400 nm. The laser spot is incident on the magnetic disk and the reflected signal is collected by the same objective.

The sample substrate is polished to a thickness of 50 μm and positioned above the center conductor of a coplanar waveguide (CPWG) as shown in Fig. 2.3(b) [89]. A current passes through the CPWG and generates a magnetic field. The thin substrate allows the magnetic disks (on the substrate) to be sufficiently close to the waveguide and therefore to be excited by the field.

Fig. 2.3(c) is a schematic diagram showing the focused laser beam incident on a magnetic disk. In this example, the beam is focused 300 nm from the center of the disk. The measured signal $\theta_{Kerr} \propto M_z$, and the offset of the beam allows θ_{Kerr} to be sensitive to the position of the vortex core, which is the only region with non-zero M_z. The position of the vortex core is probed as a function of time by varying the delay of the probe pulse relative to the excitation. The excitation, therefore, needs to have a fixed phase relative to the pulse train of the probe beam.

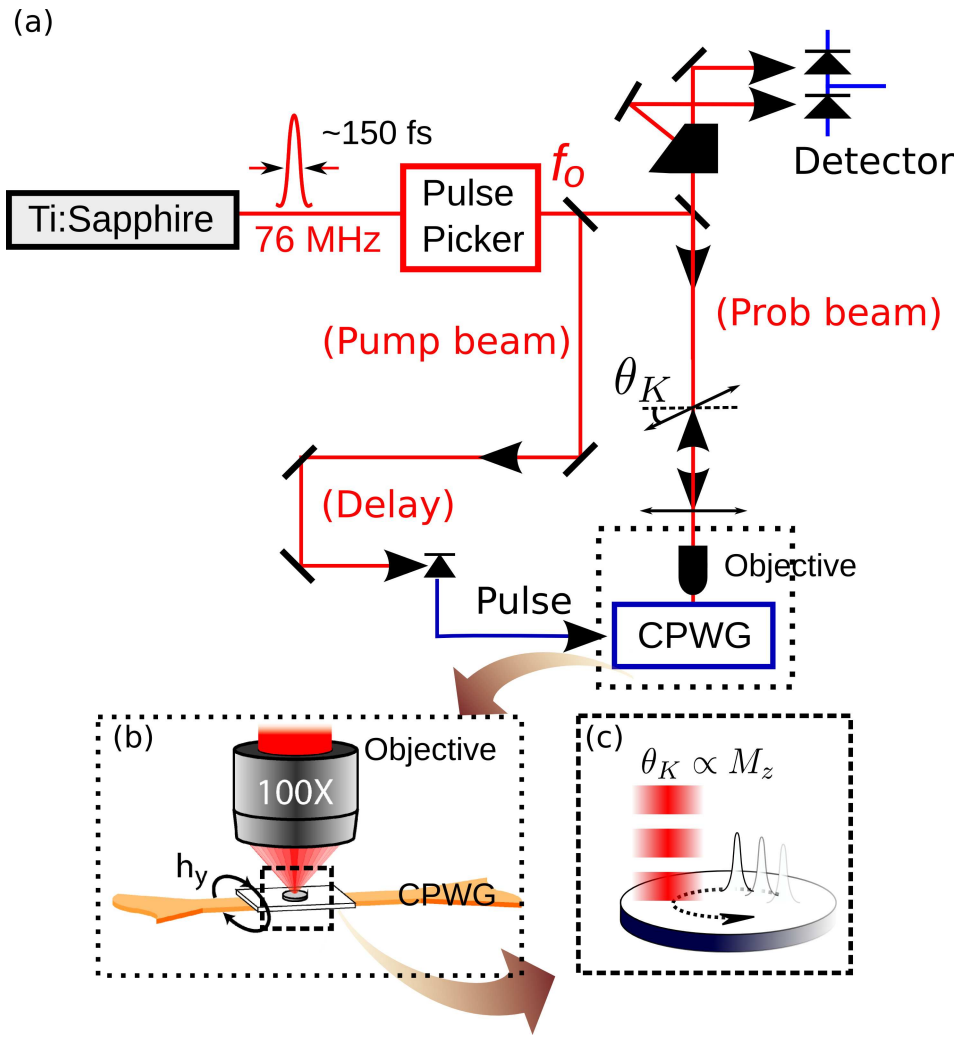

Figure 2.3: (a) Schematic diagram of the time-resolved Kerr microscope. The pulse train from the Ti:Sapphire laser is split into pump and probe beams. The pump beam is incident on a fast photoswitch, generating a pulse of electrical current that produces an in-plane field excitation. The probe beam is focused onto the sample by a microscope objective. The detector, which is a photodiode bridge, analyzes the pump-induced rotation of the polarization θ_{Kerr}. (b) Cartoon of the microscope, focusing the probe beam onto a single magnetic disk. The sample is mounted on a coplanar waveguide (CPWG). (c) Cartoon of the gyrotropic mode probed by the focused probe beam. The beam is offset from the center of the disk, so that the motion of the vortex core generates an oscillating signal.

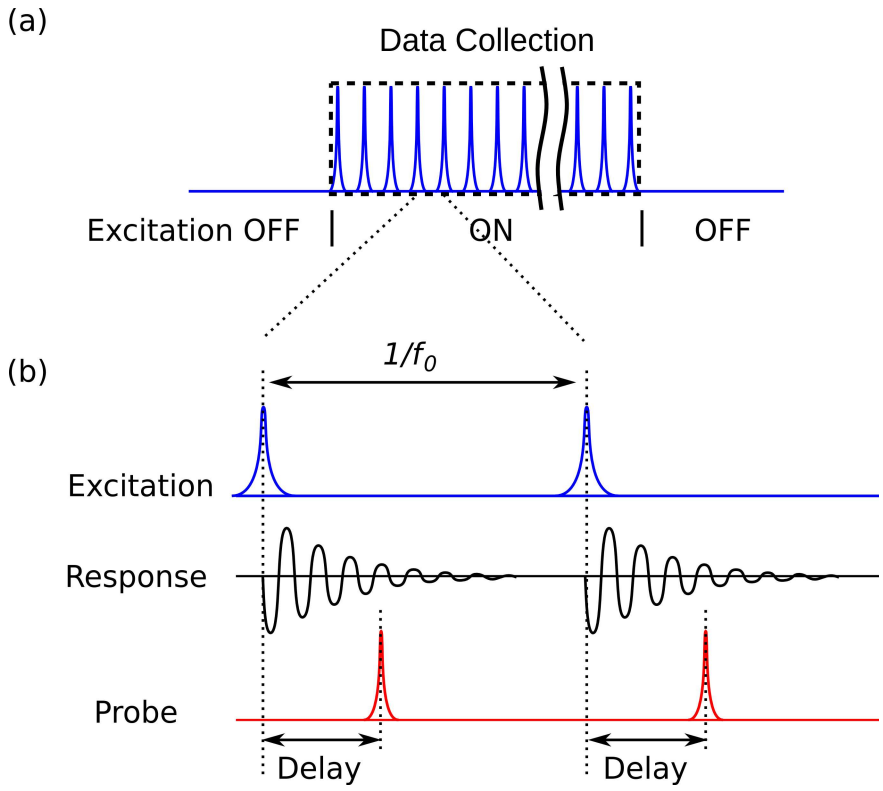

Figure 2.4: (a) Schematic representation of the drive amplitude as a function of time for the case of pulsed excitation. The modulation is applied for lock-in detection. Data of the response amplitude is collected during the ON cycles. (b) Schematic representation of the excitation (i.e., magnetic field), the response θ_{Kerr}, and the probe (i.e., optical pulse), as a function of time. The repetition period of the excitation and the probe is $1/f_0$. The probe is delayed relative to the excitation to detect the response as a function of time.

The details of the synchronization will be discussed in the following.

2.2.2 Pulsed Excitation

For the pulsed excitation setup [Fig. 2.3(a)], the pump beam is delayed relative to the probe beam by a movable retroflector, after which it is incident on a fast photoswitch (Hammamatsu G4176-03), producing electrical pulses with a temporal width $\sim$ 120 ps. This electrical signal is launched into the CPWG on which the sample is mounted. The electrical signal generates a pulse of in-plane oriented magnetic field, which drives the vortex motion. The amplitude of the magnetic field pulse can be calculated from the magnitude of the current, the thickness of the sample substrate, and the geometry of the CPWG.

Fig. 2.4(a) shows a schematic of the excitation amplitude as a function of time. The excitation is modulated on and off at 2.5 kHz by optically chopping the pump beam, so that the pump-induced change in polarization of the probe beam (detected by a polarization bridge) can be analyzed by a lock-in amplifier. Fig. 2.4(b) shows the relative phases for the excitation pulse, the response θ_{Kerr}, and the probe pulse. The response after each excitation pulse is a damped oscillation, corresponding to the orbital motion of the vortex core. The repetition of the excitation and the probe are tuned to be at $1/f_0 = 39.5$ ns, so that the response damps out before the next cycle. The delay between the excitation and the probe allows for the time-resolved measurement.

Fig. 2.5(a) shows typical data of a time scan. After the excitation pulse is applied at $t = 0$ ns, a 0.2 GHz (5 ns period) response is clearly seen. This corresponds to the orbital motion of the vortex core. Besides the core motion, immediately after the excitation, a higher frequency response damps out quickly before 2 ns, and it corresponds to the azimuthal spin-wave modes of the in-plane magnetization of the vortex [69]. These modes are revealed by the Fourier transform of the time scan, as shown in Fig. 2.5(b). The strong peak at 0.2 GHz associated with the core motion, and the two small peaks at 3.6 GHz and 4.4 GHz are the spin-wave

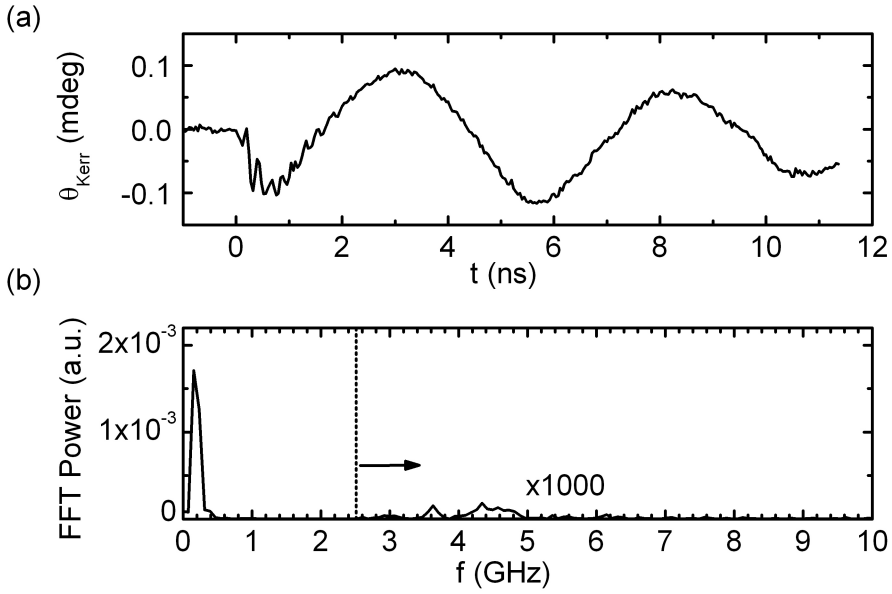

Figure 2.5: (a) Representative time scan using the pulsed excitation approach. The excitation is applied at $t = 0$ ns, with an amplitude of 4 Oe. Data were obtained from a 2 μm $\times$ 50 nm disk (sample 12). (b) The Fourier transform of (a). The data for $f > 2.5$ GHz are multiplied by 1000 for a better visibility.

modes propagating clockwise and counterclockwise around the disk. As pointed out by Park and Crowell [69, 89], the spin waves couple with the gyrotropic motion of the vortex. The symmetry of these two spin-wave modes is broken because the orbital motion of the core is either clockwise or counterclockwise.

In this dissertation I will focus on the orbital motion of the core. In practice, the pulsed excitation approach allows us to characterize the frequency of this mode very efficiently ($\sim$ 1 minute/scan). The efficiency becomes important for characterizing pinning defects in a material. I will show experimental data of more than 3000 time scans in Ch. 4.

2.2.3 Continuous-Wave (CW) Excitation

Fig. 2.6 shows the setup for continuous-wave (CW) excitation. The pump pulses are used as the clock input for a phase-locked loop (SiliconLabs Si5325-26), or

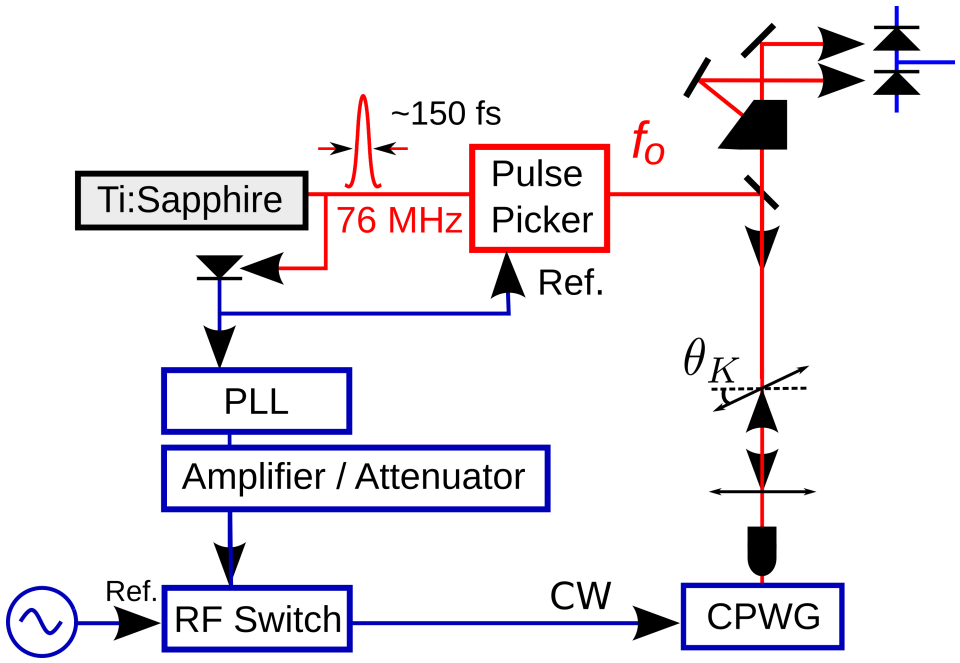

Figure 2.6: Schematic diagram of the time-resolved Kerr microscope for the case of CW excitation. The blue lines indicate the electric paths, and the red lines indicate the optical paths. The movable retroflector in Fig: 2.3 is bypassed, so that the pump beam is incident on a photodiode, which produces an electrical clock signal to the phase lock loop (PLL). A function generator (not shown) provides the reference for the RF switch and the lock-in amplifier.

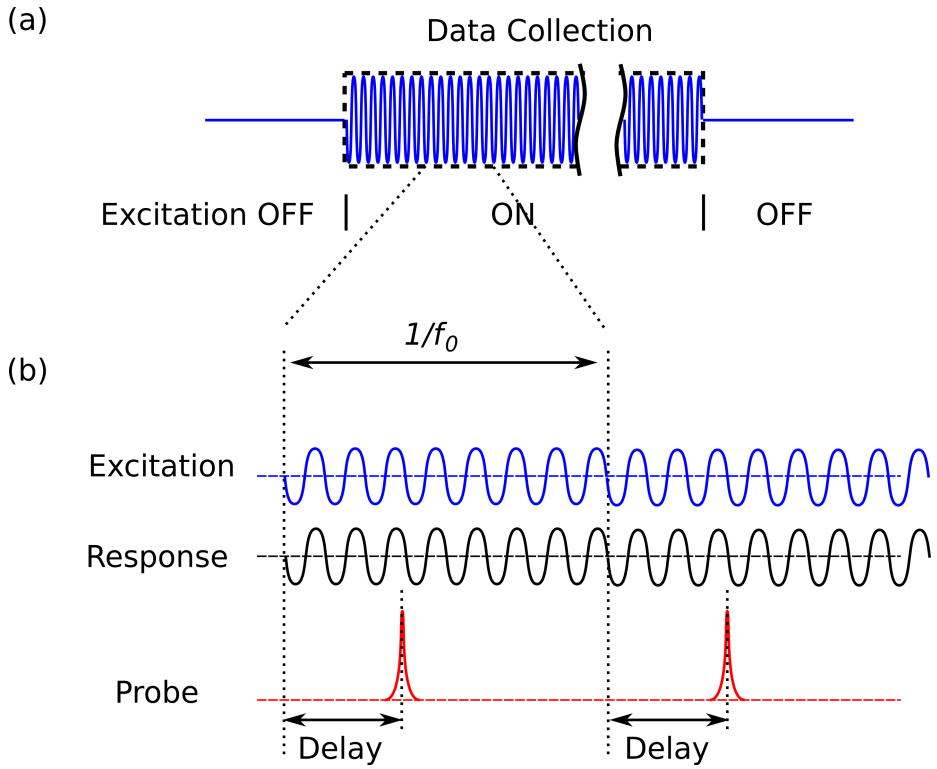

Figure 2.7: (a) Schematic representation of the drive amplitude as a function of time for the case of CW excitation. (b) Schematic representation of the excitation (i.e., magnetic field), the response θ_{Kerr}, and the probe (i.e., optical pulse), as a function of time. The repetition period of the probe is $1/f_0$. The probe is delayed relative to the excitation to detect the response as a function of time.

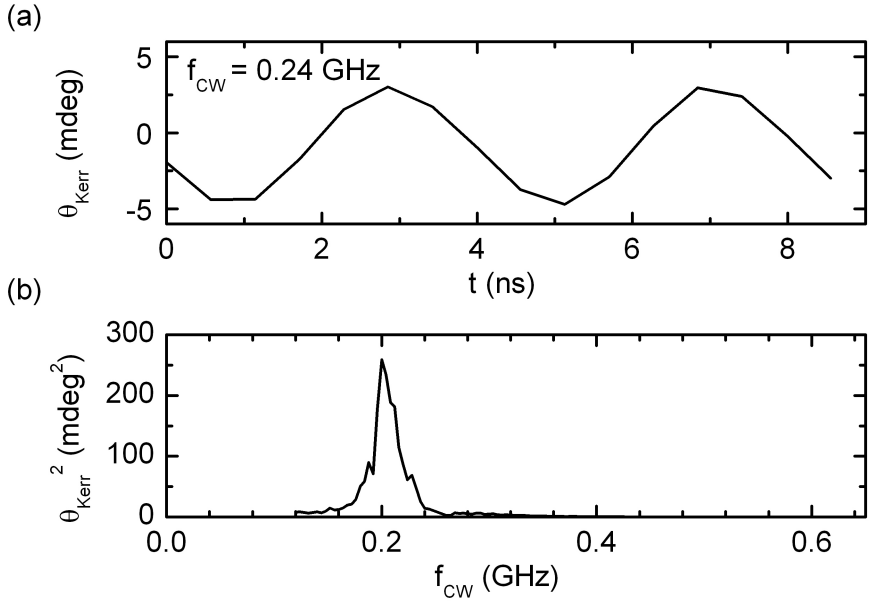

Figure 2.8: (a) Representative time scan in the case of CW excitation. The frequency of the excitation field is $f_{CW} = 0.24$ GHz. The field amplitude is 1.8 Oe. Data were obtained from a 2 μm $\times$ 50 nm disk (sample 12). (b) Gyrotropic mode spectra obtained by measuring the response power of the gyrotropic mode ${\theta_{Kerr}}^2$ as a function of the excitation frequency f_{CW}.

PLL, which synthesizes a sine wave with a frequency that can be selected from 2 MHz to 1400 MHz. The excitation power can be controlled over 4 orders of magnitude with a 0.5 dB resolution by using an amplifier and a digital attenuator. A RF switch chops the signal on and off at 2.5 kHz for lock-in amplifier detection. This 2.5 kHz chopping signal is obtained from a function generator, which does not need to be synchronized with the laser clock. Fig. 2.7(a) shows schematically the excitation signal as a function of time. Fig. 2.7(b) shows a zoomed-in view of Fig. 2.7(a) and the relative phases for the excitation sine wave, the response θ_{Kerr}, and the probe pulse. The important feature is that the excitation sine wave is phase-locked to the repetition rate of the probe beam ($f_0 = 4$ MHz). Similar to the pulsed excitation discussed above, the excited vortex-core motion is probed as a function of time by varying the delay of the probe pulse relative to the CW excitation. In this case, the delay is achieved by controlling the PLL electronically, instead of using a optical delay.

The CW excitation induces a steady state motion of the vortex core. Specifically, the orbital motion of the core builds up in amplitude starting from rest at the beginning of each data collection period. The orbital motion reaches a steady state after a typical time ~ 100 ns, which is determined by damping. The duration of the data collection period (200 μs) is much longer than the build-up time, so that the collected data represent the steady state motion.

Typical data for the case of CW excitation are presented in Fig. 2.8(a), which shows the steady-state gyrotropic motion of the vortex core measured at excitation frequency $f_{CW} = 0.24$ GHz. Fig. 2.8(b) shows the response power of the gyrotropic mode as a function f_{CW}. The peak of the gyrotropic mode spectrum shows a resonant frequency at 0.20 GHz, as is typical for a 2 μm diameter disk with 50 nm thickness.

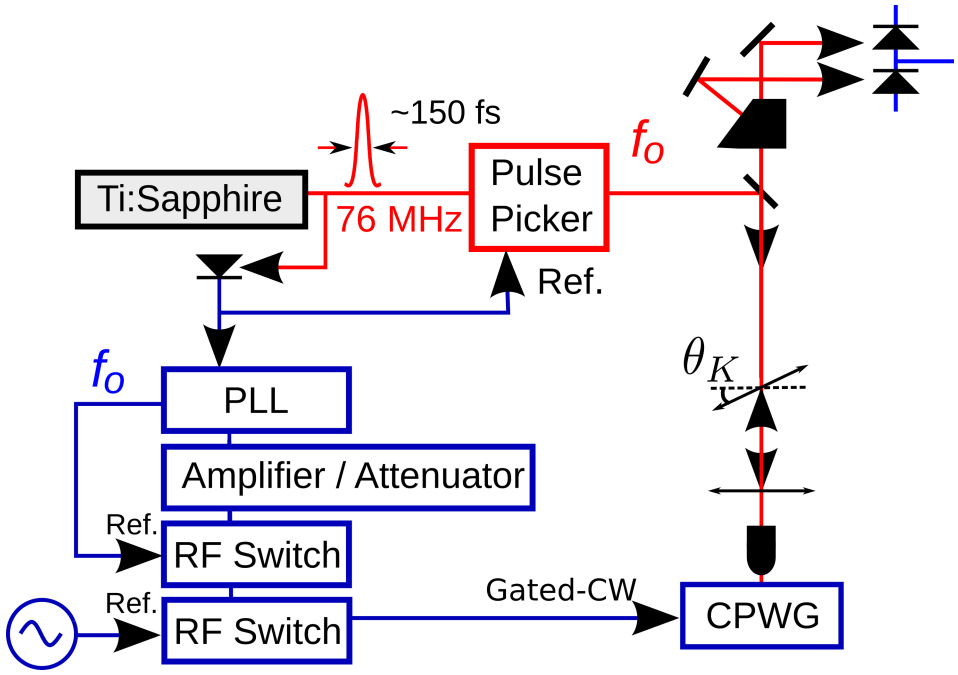

Figure 2.9: Schematic diagram of the time-resolved Kerr microscope for the gated CW excitation. An additional RF switch is added to the CW excitation setup (Fig. 2.7). This added RF switch is synchronized in phase with the PLL.

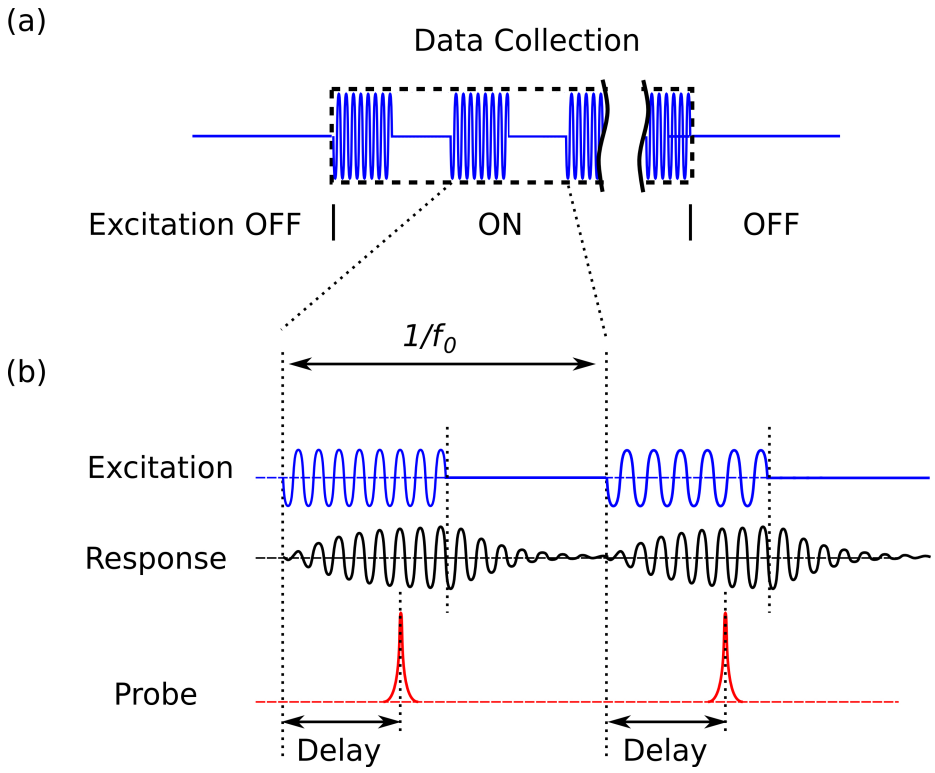

Figure 2.10: (a) Schematic representation of the drive amplitude as a function of time for the case of gated-CW excitation. The excitation is modulated within every "ON" cycle at the same phase and frequency as the probe beam. (b) Schematic representation of the excitation (i.e., magnetic field), the response θ_{Kerr}, and the probe (i.e., optical pulse), as a function of time. The repetition period of the excitation and the probe is $1/f_0$. The probe is delayed relative to the excitation to detect the response as a function of time.

2.2.4 Gated-CW Excitation

As shown in Fig. 2.9, gated-CW excitation is achieved by adding an additional RF switch to the CW-excitation setup. The added RF switch is synchronized in phase with PLL, so that the RF switch chops the excitation at $f_0 = 2$ MHz with a fixed phase relative to the probe beam. Fig. 2.10(a) shows schematically the resulting wave form. Fig. 2.10(b) shows the relative phases for the excitation, the response θ_{Kerr}, and the probe pulse. The delay time between the probe and the excitation allows for a time-resolved measurement of the response. With this approach I can measure the response of the vortex core as it starts from rest, or rings down after the excitation is turned off.

Fig. 2.11 shows typical data of a time scan in the case of gated-CW excitation. The frequency of the applied field is 0.20 GHz and the amplitude is 1 Oe. When the excitation is turned on at $t = 0$ ns, the gyrotropic motion of the vortex core builds up and gradually reaches a steady state. After the excitation is turned off at $t = 190$ ns, the gyrotropic motion decays exponentially.

There are two important aspects of the gated-CW technique. First, the total scanning time (the allowed delay time between the excitation and probe) can be as long as 500 ns, limited by $1/f_0$. The total scanning time is much longer than that of the pulsed excitation approach, which is 10 ns, limited by the distance of the movable optical path. Secondly, compared to the pulsed excitation approach, the gated-CW excitation has the advantage of controlling the motion of the vortex core *before* the excitation is turned off. With these two advantages, I have applied the gated-CW approach to study the spiral motion of the vortex after the excitation is turned off. This reveals interesting details of the pinning process in the time domain, as will be discussed in Sec. 3.2.

2.2.5 Double Modulation Excitation

As shown in Sec. 2.2.3, CW excitation induces steady state vortex motion starting from rest during each data collection cycle. It is also important to measure the

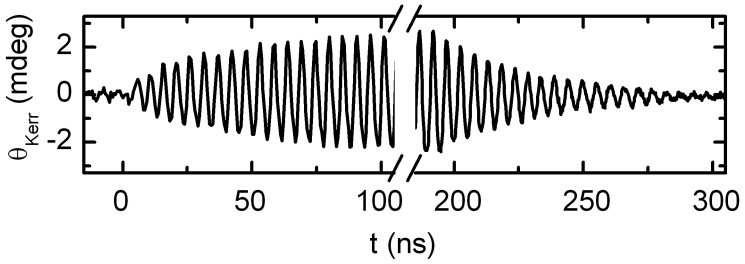

Figure 2.11: Representative time scan in the case of gated-CW excitation. The excitation field is switched on at $t = 0$ ns and it is turned off at $t = 190$ ns.

steady-state motion starting from large amplitude, rather than from rest, as I will discuss in Ch. 3. To achieve this, I have worked with Andrew Galkiewicz to developed a double-modulation technique, which discussed in the following.

Fig. 2.12 shows a schematic diagram of the double-modulation experimental setup. The output of the PLL becomes the reference for a microwave generator (Agilent N5183A), so that the output of the microwave generator is synchronized in phase with the probed beam. The output signal of the microwave generator is a sine wave with two modulation options, both of which are used in this case. The first modulation is referred to as pulsed modulation (PM), which corresponds to the chopping of the continuous sine wave on and off. The second modulation is referred to as amplitude modulation (AM), which modulates of the amplitude of the sine wave. For the case of the double-modulation setup, PM and AM are at the same frequency (2.5 kHz), but with a fixed phase difference. AM is delayed relative to PM by a delay time T_1.

Fig. 2.13(a) shows a schematic representation of the modulated sine wave for the case of double modulation. PM allows the excitation to have ON and OFF cycles for lock-in detection. AM is used to change the amplitude of sine wave except for the initial T_1 of each ON cycle, which therefore has two parts. The first part has a duration of $T_1 = 2$ μs and an amplitude of $A_1 = 6.4$ Oe, and the second part has a duration of $T_2 = 198$ μs and an amplitude of $A_2 \leq A_1$. Because $T_2 >> T_1$, the collected data represent primarily the response in the second part

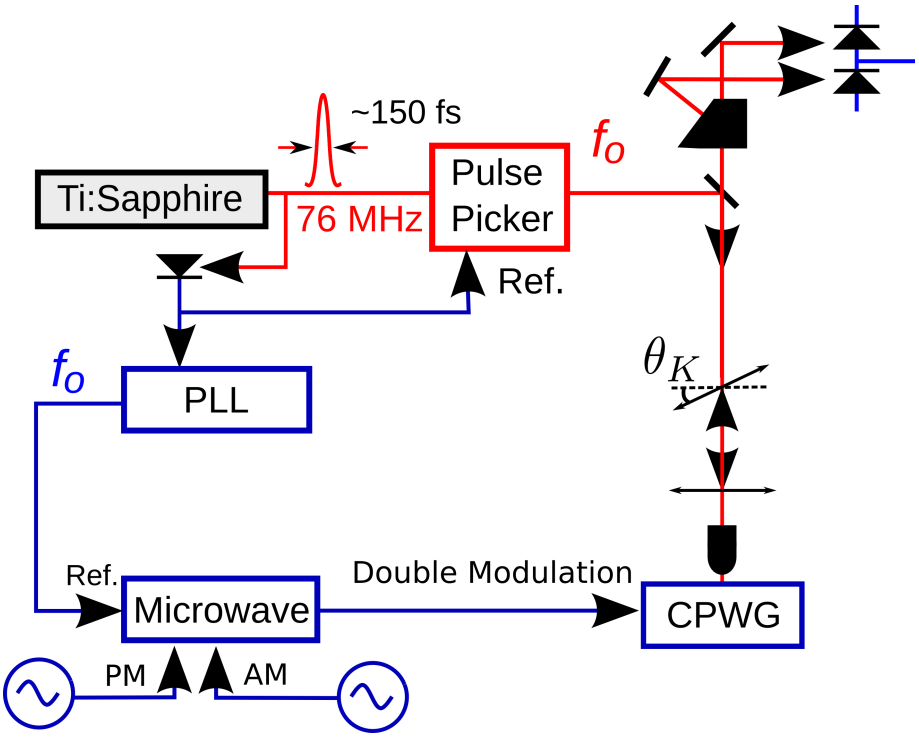

Figure 2.12: Schematic diagram of the time-resolved Kerr microscope for the case of the double-modulation technique. A microwave source is used to synthesize a continuous wave, with pulsed modulation (PM) and amplitude modulation (AM).

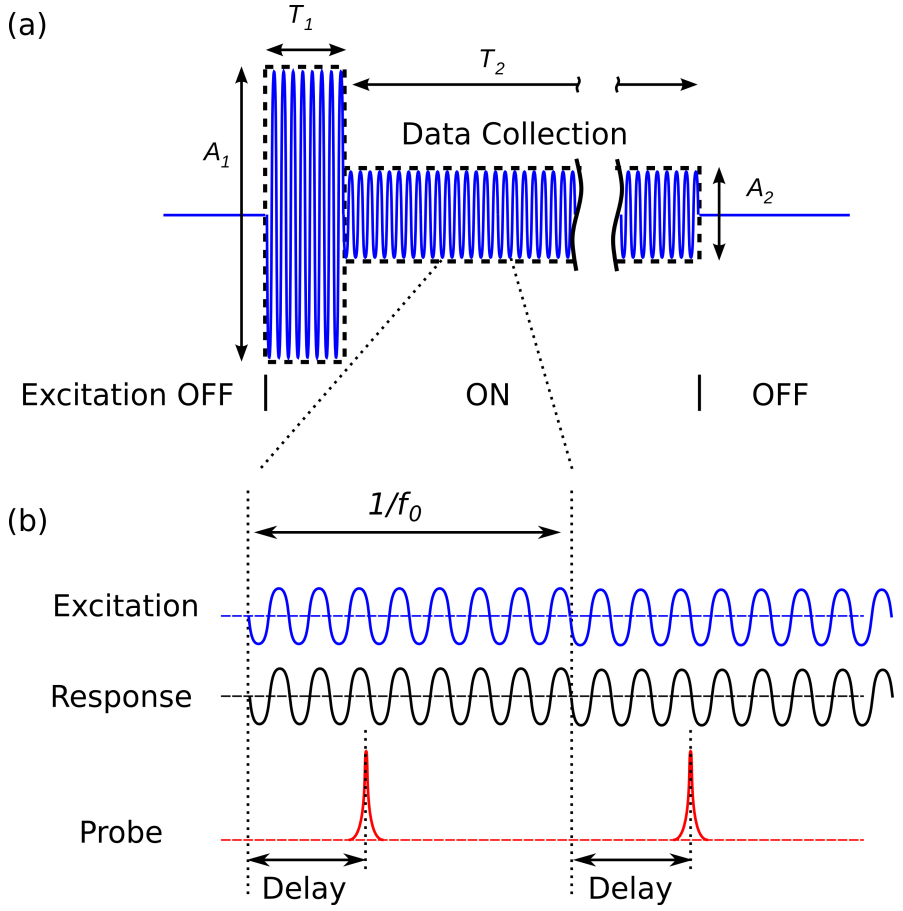

Figure 2.13: (a) Schematic representation of the drive amplitude as a function of time for the case of the double modulation technique. T_1 and A_1 indicate the duration and the amplitude of the first part of the ON cycle, while T_2 and A_2 are for the second part. The collected data correspond to the response amplitude effectively only during T_2, because T_2 is much longer then T_1. (b) Schematic representation of the excitation (i.e., magnetic field), the response θ_{Kerr}, and the probe (i.e., optical pulse), as a function of time. The repetition period of the excitation and the probe is $1/f_0$. The probe is delayed relative to the excitation to detect the response as a function of time

of the ON cycle. Fig. 2.7(b) shows the relative phases for the excitation sine wave, the response θ_{Kerr}, and the probe pulse. The excitation sine wave is phase-locked to the repetition rate of the probe beam. Similar to the CW excitation setup discussed in Sec. 2.2.3, the excited vortex-core motion is probed as a function of time by varying the delay of the probe pulse relative to the excitation.

Chapter 3

Non-linear Dynamics of a Magnetic Vortex in the Presence of Pinning

Recall from Sec.1.4 that defects in ferromagnetic films create localized pinning potentials, which influence the dynamics of a magnetic vortex. In this chapter I will discuss the depinning transition of a magnetic vortex and the associated non-linear dynamics. In the first part, I will show a set of measurements on a single magnetic vortex over a large dynamic range in amplitude and frequency, revealing a complete dynamic phase diagram. A simple model captures the physics of the observed phase diagram. In the second part, I will show a direct observation of the pinning process in the time domain.

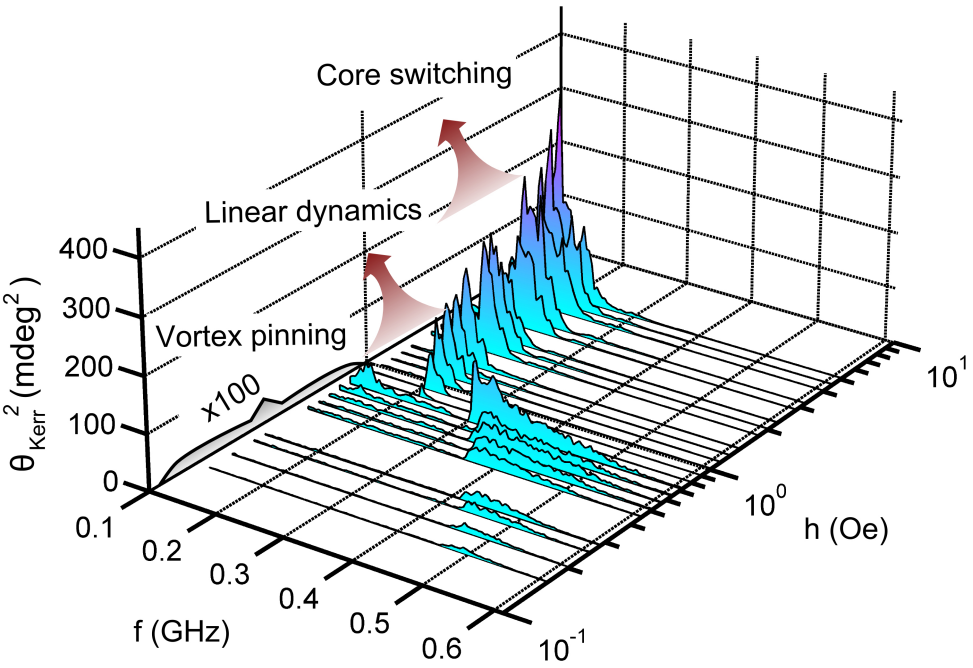

Figure 3.1: Observed gyrotropic spectra of a 2 um diameter disk excited by CW magnetic field for amplitudes from 0.2 Oe to 5.1 Oe. The equilibrium position of the core is determined by the external field of -50 Oe. Data at drive amplitudes below 0.8 Oe are multiplied by 100 for better visibility.

3.1 Dynamic Phase Diagram of a Magnetic Vortex

3.1.1 Gyrotropic-Mode Spectra

The spectrum of the gyrotropic mode can be measured by using the TRKM with the CW-excitation aproach, as described in Sec. 2.2.3. I will focus on a 2 μm diameter disk (sample 11) and discuss how the spectrum changes with the excitation amplitude.

As CW excitation is applied, the y-component of the motion of the vortex core is measured as a function of excitation frequency and amplitude, as shown in Fig. 3.1. For excitation fields between 1 and 2 Oe, the spectra show a single symmetric peak at 0.20 GHz. This is the ordinary gyrotropic mode, and both the lineshape and peak position indicate that the vortex dynamics are linear over this range [67, 69, 77, 78]. The equation of motion for a vortex in this case can be derived from the Thiele equation (Eq. 1.12), as discussed in Sec. 1.4.1.

For excitation fields above 2 Oe, the spectra become irregular. As originally observed by Vansteenkiste et al. [72], in this regime the assumption of a rigid core breaks down, and this results in the reversal the core polarity at the highest core velocities [71]. I will show in the following section that the apparent splitting of gyrotropic-mode spectra in this range results from the suppression of the average gyrotropic signal by successive core annihilation events [84, 90].

3.1.2 Reversal of the Vortex Core Polarity

To investigate the origin of the irregular spectrum at high amplitudes (Fig. 3.1), I performed time-resolved measurements by using gated-CW excitation (Sec. 2.2.4). The y-component of gyrotropic motion is shown in Fig. 3.2(a) as a function of time for excitation amplitudes of 1.3, 2.3, 2.9, and 4.6 Oe. The excitation field is turned on at $t = 0$ ns and switched off at $t = 190$ n. For an excitation field of 1.3 Oe, the amplitude of the gyrotropic motion saturates within 1 to 2 cycles. In contrast,

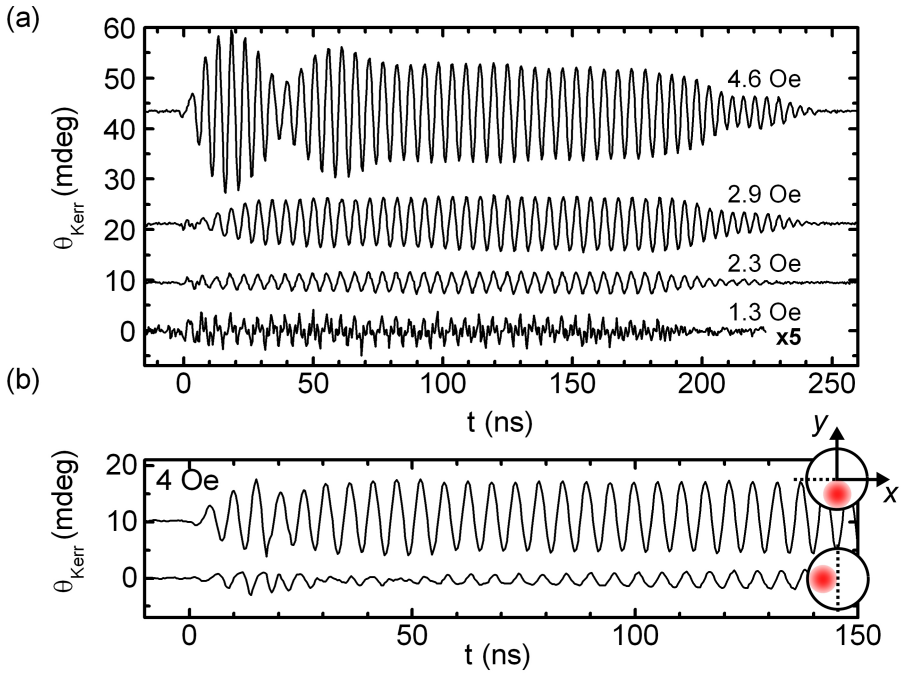

Figure 3.2: (a) Time-resolved data showing the y-component of the vortex motion for different excitation amplitudes at a frequency of 0.20 GHz. The data at 1.3 Oe are multiplied by 5 for better visibility. (b) Time-resolved data for different probe-beam positions, showing the asymmetry between the x- and y-components of the gyrotropic motion due to polarity switching. The insets are cartoons showing the offset directions of the focused probe beam (red circle).

the data obtained at 2.3 Oe show the typical orbital motion of a depinned vortex core, with a very long build-up and ringdown time determined by the Gilbert damping. At 2.9 Oe, the gyrotropic motion is similar, except that the apparent time constants for the build-up and decay of the motion become shorter. At 4.6 Oe, the motion shows dramatic amplitude modulation in the time domain. At the highest amplitudes, the apparent motion of the vortex core also becomes highly elliptical, as can be seen in Fig. 3.2(b), which shows the x and y components of the motion. The x-component is suppressed nearly completely.

In interpreting the data of Fig. 3.2, it is essential to realize that the detection of the vortex motion is stroboscopic, and so any process that is not strictly coherent will lead to averaging in the time domain. This is why the apparent build-up of motion for a vortex core near the depinning threshold (1.3 Oe) appears to occur in only 1 or 2 cycles. For successive clock cycles, the orbital phase varies stochastically. At high amplitudes, the effect that appears to be beating at 4.6 Oe is associated with reversal of the vortex core polarity (at approximately 25 ns). If the reversal always occurred at the exact same point for each clock cycle, the observed signal would undergo a rapid collapse followed by a build-up and then subsequent collapse as the core reverses again. In practice, the averaging over many 2 MHz clock cycles smears out the progressive build-up and collapse of the gyrotropic motion. The apparent beating is due to the successive reversal events. As the number of reversals increases, the uncertainty in the time at which the nth reversal occurs becomes comparable to the gyrotropic period and the modulation is no longer evident. This steady-state signal is smaller than it would be if the response in the linear regime (without core reversal) were extrapolated to higher drive amplitude. This is the primary reason for the "hole" that appears near the original gyrotropic frequency in the highest amplitude spectra shown in Fig. 3.1. Essentially, the power around this frequency ends up being dissipated during core flips, producing what appears to be splitting in the spectrum.

Each core reversal produces a change in the direction of gyration as well as a change in the sign of the polar Kerr signal, as discussed in Sec. 1.4.4. For

this reason, a superposition of signals from clockwise and counterclockwise orbits will appear as oscillatory motion of the vortex core parallel to the axis of the oscillating field (y in our case), with no component along x. This observation, also made by Cheng *et al.* [91], depends on the phase of the gyrotropic motion with respect to the alternating field and agrees with the calculation in Ref. [82]. In fact, Fig. 3.2(b) shows that the observed x-component of the motion is very weak, implying that there is incomplete cancellation of the signals from the two different directions of rotation. It is possible to verify the sense of rotation directly by imaging. I find that if the amplitude is increased above 2 Oe and then reduced back to the linear regime, the sense of rotation may be reversed. This is due to the fact that after 190 ns (and many core flips), the polarity of the vortex core is nearly random.

Careful analysis of the time-domain data as well as the spatial dependence of the signal demonstrate that the dynamics in the strong excitation regime are dominated by successive reversals of the vortex core polarity.

3.1.3 Pinning Potential

I now consider excitation fields below 1 Oe in Fig. 3.1. At the lowest excitation amplitude 0.2 Oe, the spectrum of Fig. 3.1 shows a resonant peak at about 0.50 GHz, which is much higher than the gyrotropic mode frequency observed at higher amplitudes. As shown previously using pulsed excitation [64, 65] (Sec. 1.4.6), this enhancement of the gyrotropic frequency is due to pinning and the measured frequency reflects the local curvature of the effective potential $W(r)$. As the amplitude increases, the peak shifts to lower frequencies, but the weight at higher frequencies is preserved, and so the lineshape becomes triangular. Over a narrow range of driving amplitudes (0.8 to 1.0 Oe), the response amplitude increases by a factor of 10, and a narrow peak emerges at the gyrotropic frequency (0.20 GHz). I will discuss in the following how this behavior emerges from the dynamics of a driven vortex in the presence of a pinning site.

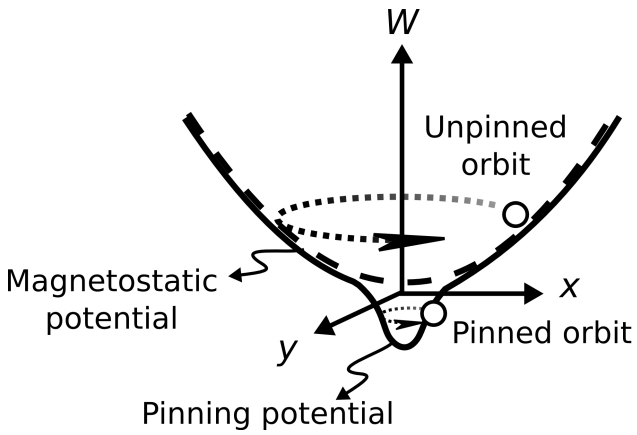

Figure 3.3: Schematic of the potential energy described by Eq. 3.1, including a parabolic magnetostatic potential (dashed curve) and a Gaussian pinning potential due to a point-like defect. The dotted arrows indicate the pinned and unpinned orbits of the ovrtex core.

To model the spectrum in the presence of pinning, I assume a total potential

$$W(r) = \frac{1}{2}kr^2 + W_p(r), \tag{3.1}$$

where W_p is the pinning potential and $\frac{1}{2}kr^2$ is the magnetostatic potential from the geometry, as discussed in Sec. 1.4.4. W_p must have a local minimum (below that of the background magnetostatic potential) and must vanish for large r, as shown schematically in Fig. 3.3 for the total energy. As originally suggested by Paul Crowell, we find that this condition is satisfied by a Gaussian

$$W_p = -a \cdot \exp\left(\frac{-r^2}{2c^2}\right), \tag{3.2}$$

which captures both required features with only two parameters, a depth a and a width c, or full-width at half-maximum FWHM $= c\sqrt{2\ln 2}$. Due to the form of W_p, the equation of motion Eq. 1.12 becomes a two-dimensional non-linear differential equation with explicit time-dependence. I solve this differential equation numerically using typical material constants for $Ni_{80}Fe_{20}$, including $M_s = 800$ emu/cm^3, $A = 1.05 \times 10^{-6}$ ergs/cm, $\alpha = 0.01$. In the numerical calculation the position of the vortex core can be obtained at each time step of the numerical integration.

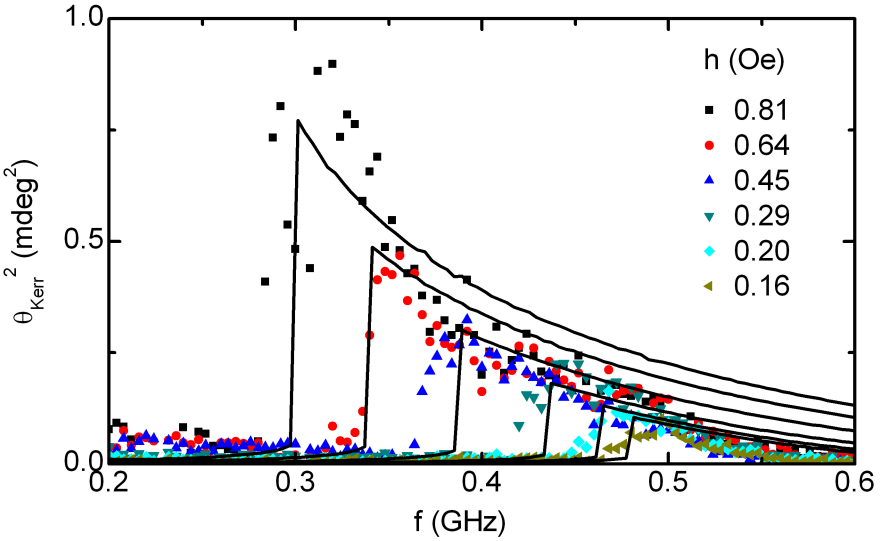

Figure 3.4: Gyrotropic spectra below 0.8 Oe from the experiment (points) and the numerical calculations (solid lines).

The orbital motion of the vortex reaches a steady state after a sufficiently large number of time steps. For a given choice of pinning center depth a and width c, I can solve for the spectrum of the steady-state vortex-core motion at each driving amplitude. Fitting of the experimental results can be achieved by the numerical calculations with different combinations of a and c. The results of this fit are shown in Fig. 3.4 as solid curves, which were obtained for $a = 0.17$ eV and the FWHM $c\sqrt{2\ln 2} = 7$ nm.

This model has two important aspects. First, it allows for determining the strength and range of pinning sites. The same approach can be applied to other pinning sites in the same disk in addition to the pinning site discussed above, and the experimental results show an average pinning energy 0.7 ± 0.2 eV and pinning range 16 ± 3 nm from six random pinning defects measured in this sample.

Second, the model provides a realistic picture of the depinning transition and the dynamics above the depinning transition. The solutions of Eq. 1.12 with W of the form of Eq. 3.1 are orbits. At small amplitudes, the frequency of an

orbit depends on r. For $r > c$, the frequency rapidly approaches the unpinned gyrotropic frequency (0.20 GHz). There is a well-defined boundary that separates these two regimes.

3.1.4 Phase Diagram of Vortex Dynamics

To obtain a global picture, it is instructive to represent the orbital amplitude as a contour plot in a parameter space of drive amplitude and frequency, as shown in Fig. 3.5(a) for the experiment and Fig. 3.5(b) for the numerical results. Note that the contours are shown for increasing amplitude, obtained by exciting the vortex starting from rest at each step of frequency and amplitude (CW excitation, see Sec. 2.2.3). The unpinned and pinned gyrotropic frequencies are indicated by vertical dashed lines. The sharp boundary separating the pinned and unpinned regimes as the drive amplitude increases is particularly evident for frequencies near the unpinned gyrotropic frequency.

3.1.5 Metastable Orbits of the Vortex Core

The numerical calculations [Fig. 3.5(a)] show that there are two metastable orbits in the depinning region, the boundary of which is shown as a dashed curve in Fig. 3.5(b). The two orbits in the metastable region include a pinned orbit and an unpinned orbit, while outside this region only one orbit exists, which is either pinned or unpinned. At an excitation frequency $f = 0.20$ GHz, for example, Fig. 3.6 shows the numerical solutions at three excitation amplitudes, 2.0 Oe, 0.5 Oe, and 0.05 Oe, representing three typical regions in the phase diagram. For the case of a 2.0 Oe excitation amplitude, as shown in Fig. 3.6(a), the numerical solution is a circular orbit with a diameter larger than that of the pinning potential (7 nm). The circular shape reflects that, in this range of field amplitude, the vortex dynamics are analogous to the dynamics of a 2D harmonic oscillator driven at resonance, as discussed in Sec. 1.4.4.

At 0.5 Oe, as shown in Fig. 3.6(b), both an unpinned orbit (outside the pinning

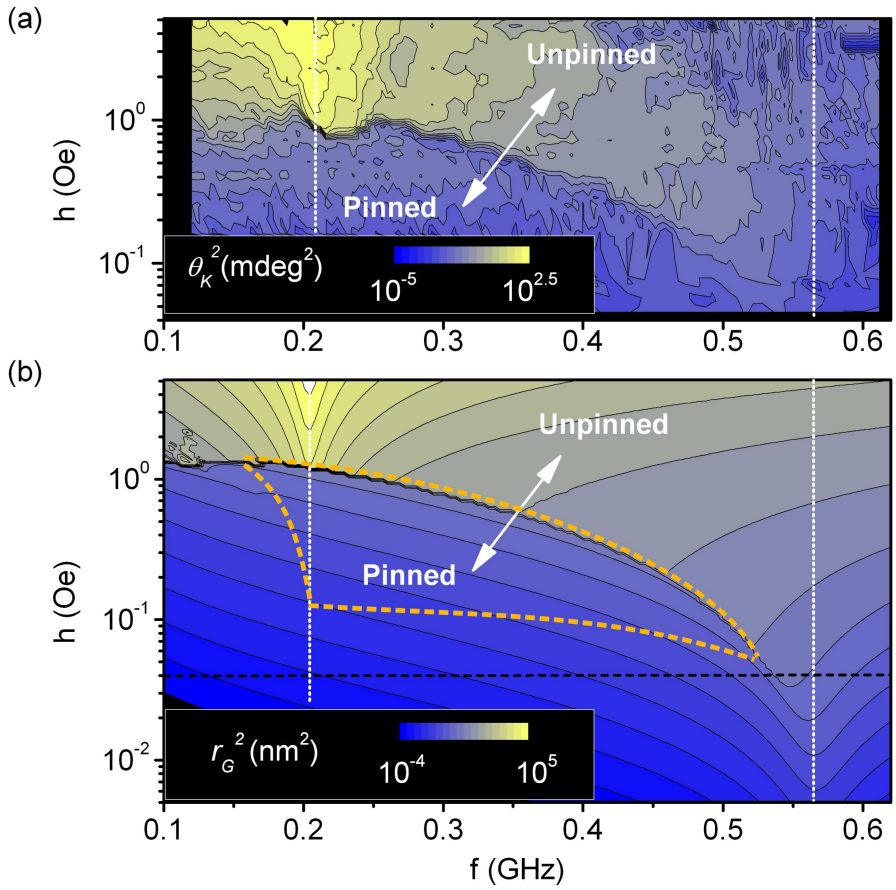

Figure 3.5: (a), (b), Gyrotropic response as a function of excitation amplitude and frequency for (a) the experiment and (b) the numerical calculations. The experimental parameter space is above the horizontal dashed line in (b). The color scale is logarithmic. The contours are shown for increasing amplitude. The dashed curve in (b) shows the boundary of the region in which two gyrotropic orbits exist.

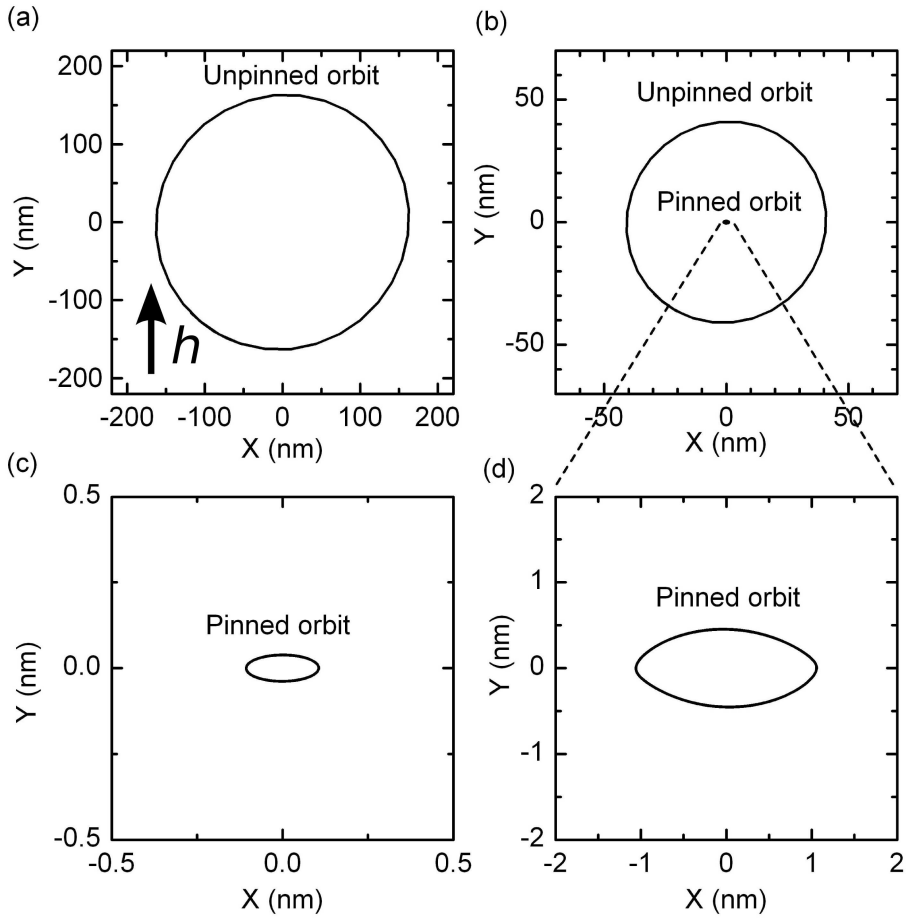

Figure 3.6: Gyrotropic orbits of the vortex core calculated at (a) 2.0 Oe, (b) 0.5 Oe, and (c) 0.05 Oe. The excitation frequency is at 0.20 GHz. The excitation field h is a sine wave oriented along the y-axis as indicated by the arrorw in (a). (d) Zoomed-in view of the pinned orbit in (b).

range) and a pinned orbit (inside the pinning range) exist. At 0.05 Oe, as shown in Fig. 3.6(c), only a pinned orbit exists. Recall from Sec. 1.4.4 that, for the gyrotropic mode in a parabolic potential, the orbits are elliptical when the drive frequency $f < f_G$, where f_G is the eigenfrequency associated with the potential. The potential can be approximated as parabolic near the bottom of the pinning potential (Eq. 4.2), and f_G becomes the pinned frequency f_{pin} for this case. The pinned orbit in Fig. 3.6(c) is elliptical because the drive frequency $f = 0.20$ GHz is below the resonant frequency $f_{pin} = 0.50$ GHz near the bottom of the pinning potential. Fig. 3.6(d) shows a zoomed-in view of the pinned orbit when excited at 0.5 Oe. Similar to the orbit in Fig. 3.6(c), the orbit in Fig. 3.6(d) is elongated along the x axis, but is not exactly elliptical. The shape of the orbit at 0.5 Oe reflects that, in the depinning regime, the potential energy (Eq. 3.1) is anharmonic.

To probe the metastability in experiment, I carried out a monotonic sweep of the drive amplitude in both directions using the double modulation technique described in Sec. 2.2.5. Experimental data are presented as solid (increasing) and dashed (decreasing) curves in Fig. 3.7(a), which shows the y-component of the orbital motion measured as a function of excitation amplitude at three fixed excitation frequencies. The corresponding numerical results at these frequencies are shown in Fig. 3.7(b). The depinning with increasing excitation amplitude is easily observed. At the gyrotropic frequency (0.17 GHz for this slightly larger disk), both the experimental and the numerical results clearly show hysteresis in the depinning region, demonstrating the existence of two distinct orbits. At 0.08 GHz, no hysteresis is observed as expected. At 0.27 GHz, however, hysteresis is seen in the numerical results but not in the experiment. This discrepancy is due to the presence of thermal activation in the experiment. In order to observe hysteresis, there must be a negligible probability for the core to jump from the pinned to the unpinned orbit on the time scale of the experiment, which is ~ 1 sec. The energy difference ΔE between the two orbits, calculated at the upper and lower boundaries of the coexistence region, is ~ 30 eV at 0.17 GHz, but is only ~ 0.3 eV at 0.27 GHz. The characteristic rate for thermally activated

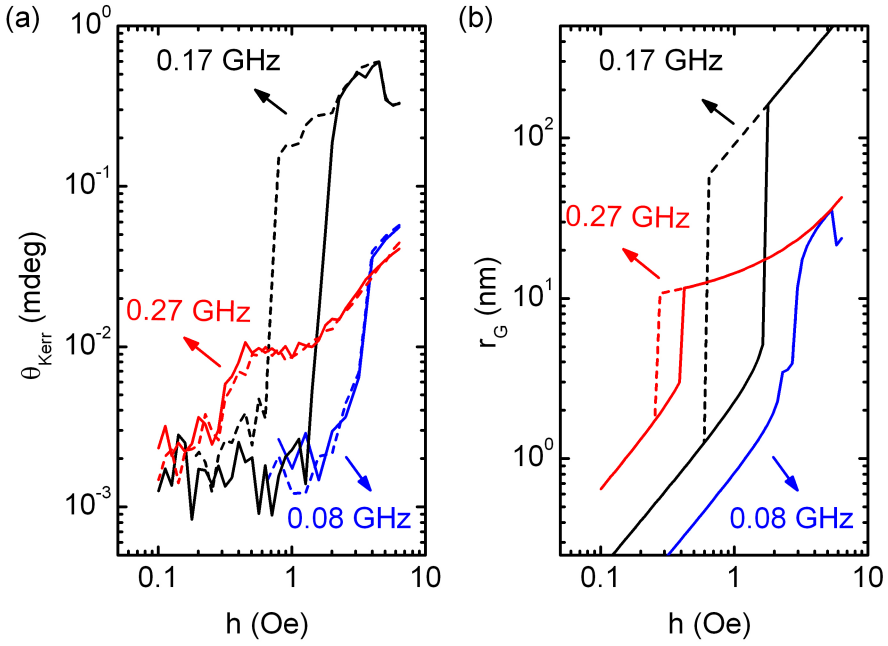

Figure 3.7: (a) Gyrotropic response versus excitation amplitude measured at 0.17 GHz (f_G of this disk), 0.08 GHz, and 0.27 GHz. Data taken on the increasing (decreasing) branch are shown using solid (dashed) lines. (b) Numerical results for the same conditions as the experiment. The two branches correspond to two different vortex core orbits.

jumps to occur is $f_0 \exp(-\Delta E/k_B T)$, where f_0 is the orbital frequency (the drive frequency). The calculated rate is insignificant at 0.17 GHz, but it is $\sim 10^3$ $\sec^{-1}$ at 0.27 GHz, which is why hysteresis cannot be observed. As the depinning transition is approached from below, thermal activation becomes significant even at the gyrotropic frequency, which is why the depinning transition at the resonance in Fig. 3.5(a) dips slightly below the boundary seen in Fig. 3.5(b) .

3.2 Pinning Process in the Time Domain

3.2.1 Spiral Motion of the Vortex Core

Pinning processes in the time domain can be investigated by using gated-CW excitation (Sec. 2.2.4). I first excited a vortex in the linear regime, below the onset of core reversal. After the excitation field was switched off, the core spiralled towards its equilibrium position, which may or may not be a pinning site, as shown schematically in Fig. 3.8 (a) and (b) respectively. Both cases were measured in the experiment, achieved by controlling the equilibrium position of the core with an in-plane oriented static field. Fig. 3.8 (c) and (d) show that the measured y-component of the orbital motion oscillates with decreasing amplitude after the excitation is switched off at $t = 0$ ns. For the unpinned vortex [Fig. 3.8(c)], the period of the oscillation remains constant, as indicated at three representative cycles. For the pinned case [Fig. 3.8(d)], in contrast, the period of the oscillation decreases as the amplitude decreases, as indicated at four representative cycles.

The differences between the unpinned and pinned cases can be clearly seen in Fig. 3.9, which shows the amplitude and frequency of the gyrotropic signal as a function of time, obtained from the data of Fig. 3.8. In the unpinned case, the amplitude decays exponentially and the gyrotropic frequency remains fixed. When, however, the equilibrium position is at a pinning site, the decay is exponential only up to a certain time, beyond which the amplitude drops more quickly and the frequency increases.

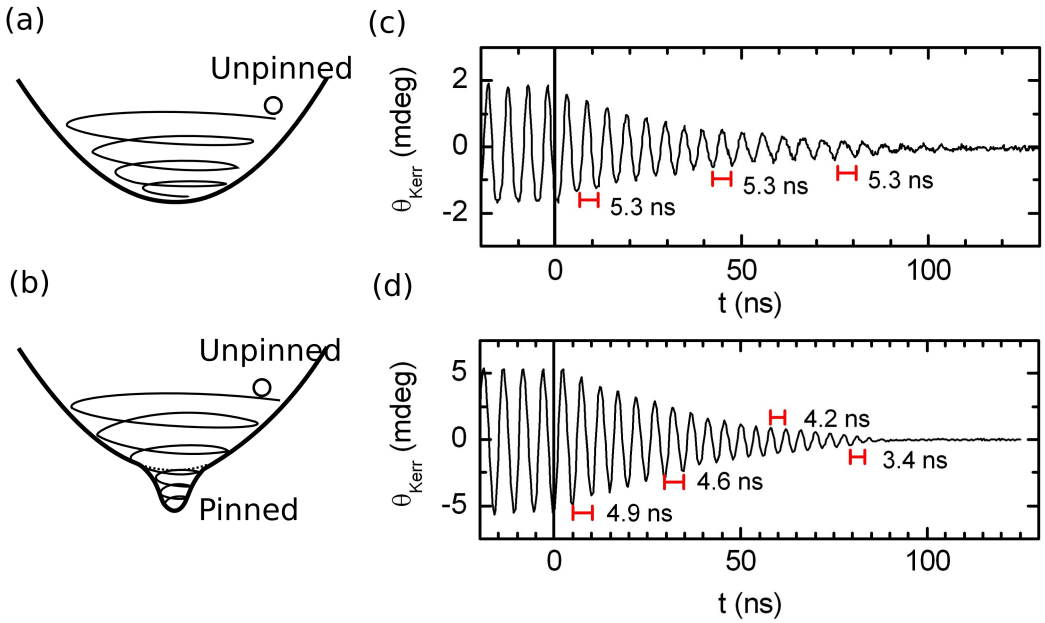

Figure 3.8: (a), (b), Cartoons of the gyrotropic motion in the potential energy, when the equilibrium position is (a) not at a pinning site or (b) at a pinning site. (c), (d), The y-component of the gyrotropic motion measured as a function of time when the equilibrium position is (a) not at a pinning site or (b) at a pinning site. The excitation is turned off at $t = 0$ ns. The periods of representative cycles are indicated by the horizontal bars.

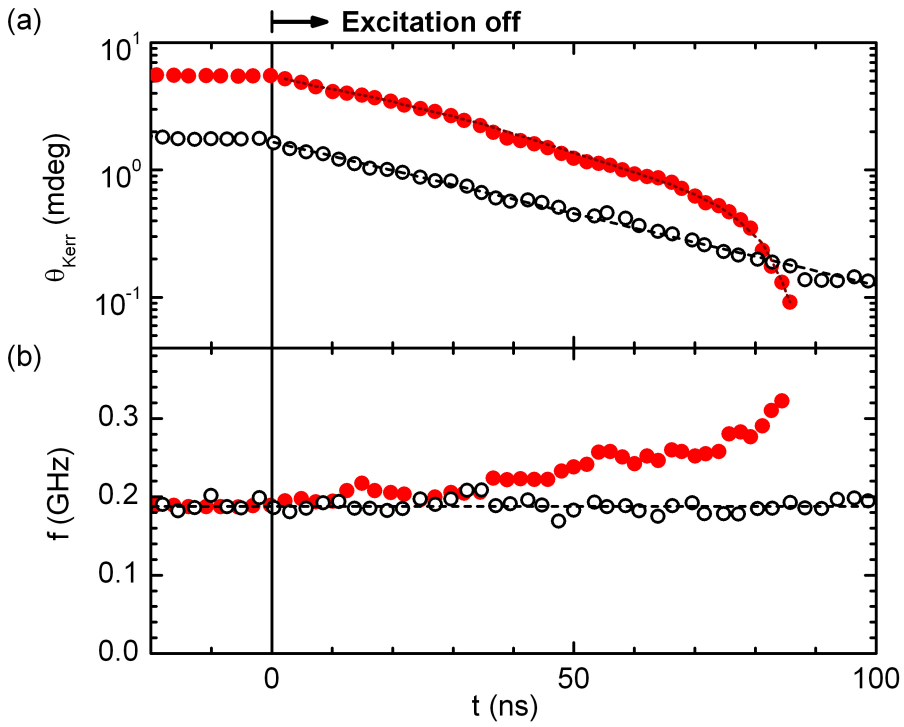

Figure 3.9: (a), (b), Amplitude (a) and frequency (b) of the gyrotropic motion measured as a function of time when the equilibrium position is at a pinning site (filled symbols) or not at a pinning site (open symbols). The dashed lines are linear fits for the open symbols.

The frequency of the oscillation remains constant immediately after the excitation is switched off because the drive frequency (before $t = 0$ ns) is at the characteristic frequency of the magnetostatic potential. For the unpinned case, the potential is parabolic for the entire process and the gyrotropic frequency remains fixed. For the pinned case, the frequency changes from the unpinned value to the pinned value as the core reaches the range of the pinning potential. For the case shown in Fig. 3.9(b), the core starts to interact with the pinning site after approximately 30 nsec.

3.2.2 Effect of Multiple Pinning Sites

It is possible to calibrate the Kerr signal in order to estimate the actual gyrotropic radius and compare it with the areal density of pinning sites, obtained by the method of measuring the gyrotropic frequency while sweeping the static magnetic field [64, 65] (Sec. 1.4.6). This reveals the important fact that at the maximum amplitude of Fig. 3.9(a), the core orbit encloses a large number of pinning sites (of order 30). This apparently has little effect on either the gyrotropic amplitude or frequency until the core starts to interact with the pinning site at its equilibrium position. The robustness of the gyrotropic orbit derives from the fact that the pinning energy, while large compared to $k_B T$, is still small compared to the overall magnetostatic energy of the disk. Detailed micromagnetic simulations by Min *et al.* [92] bear this out, in that high amplitude orbits simply avoid pinning sites, which represent minor perturbations to the magnetostatic energy.

3.2.3 Damping

In the unpinned regime, the frequency f and decay time τ can be used to determine the Gilbert damping parameter α, given that

$$f \cdot \tau = \left[\pi \left(2 + \ln \frac{R}{R_c} \right) \alpha \right]^{-1}, \tag{3.3}$$

which can be derived from Eq. 1.12 and Eq. 1.15 [77]. The unpinned data in Fig. 3.9(a) correspond to $\alpha = 0.007$, which is typical for $Ni_{80}Fe_{20}$. The data in Fig. 3.9(b) correspond to the same $\alpha = 0.007$ for $t < 30$ ns, but the apparent damping increases to ~ 0.015 as the core becomes pinned. This is unlikely, however, to reflect a true increase in the damping rate. The simulations of Min *et al.* [92] showed that the effect of pinning leads to an increase of α by $\sim 10\%$, much smaller than that observed in my experiment ($\sim 200\%$). It is more likely that fluctuations in the phase of the core motion relative to the optical probe pulse become larger as the core orbit encloses fewer pinning sites, leading to the apparent increase in the damping rate. In the absence of a single-shot measurement, it is impossible to rule out such a mechanism.

Chapter 4

Microscopic Pinning Mechanism of a Magnetic Vortex

This chapter will discuss the microscopic mechanism of vortex pinning in $Ni_{80}Fe_{20}$ films. In other words, what are the pinning defects? I will show the range and strength of pinning sites as a function of film thickness. I will also show a detailed analysis of the surface morphology of the films, which will be linked to the observed vortex pinning quantitatively.

4.1 Quantitative Measurements of Pinning Sites

The first step in identifying the dominant pinning mechanism is to characterize pinning defects for multiple samples with different growth parameters. Recall from Ch. 3 that the energy and range of a pinning site can be determined by fitting the gyrotropic-mode spectra at different amplitudes. Although this approach can provide detailed information of a pinning potential, it is time consuming in practice ($\sim$ 50 hours for a pinning site). A more efficient approach is needed for characterizing more than 10 pinning sites in each sample in order to obtain statistical results.

I have adopted a technique that was originally developed by Compton *et al.*

[64, 65] and I have established the following method to estimate the strength and range, but not the detailed form, of a pinning potential. I will show that, although this method is less rigorous than fitting the gyrotropic-mode spectra, it is effectively about 60 times faster than fitting an entire spectra.

4.1.1 Pinning Energy

Recall from Sec. 1.4.6 that Compton *et al.* [64, 65] developed a technique of constructing pinning maps by measuring f_G at different vortex-core positions. Using the same technique, I mapped the spatial distribution of pinning defects by measuring the gyrotropic frequency f_G as a function of the orthogonal in-plane oriented dc magnetic field, as shown in Fig. 4.1(a). In this case, the in-plane fields were varied in increments of 2 Oe over a range of 20 Oe $\times$ 20 Oe, which displaces the vortex core over a 80 $\times$ 80 nm^2 spatial region around the center of a 2 μm diameter disk.

Every pinning site in the pinning map shows two characteristics, the pinned frequency f_{pin}, which is the highest frequency within each point-like area, and ΔH, which is the FWHM of the f_G peak, averaged from the two orthogonal field directions. The measured ΔH and f_{pin} allow for estimating the range and energy of the pinning site, as will be described below.

Recall from Sec. 1.4.4 that the background geometric confinement W is approximated by a parabolic potential, given by $W(r) = \frac{1}{2}kr^2$, where k is the unpinned stiffness. An applied in-plane magnetic field H changes the potential energy by $H\mu r$, where $\mu = \xi M_s \pi RL$. Therefore, in an applied field the core moves to a new equilibrium position $r(H) = H\mu/k$ for an unpinned vortex.

Fig. 4.2(a) illustrates the concept of estimating E_{pin} from the measured ΔH. Assuming that the field H_0 positions the vortex core at the center of a pinning site that we want to characterize, the core is trapped by the local pinning potential W_p, unless a sufficiently large depinning field $H_{depin} \sim \frac{1}{2}\Delta H$ is applied to overcome

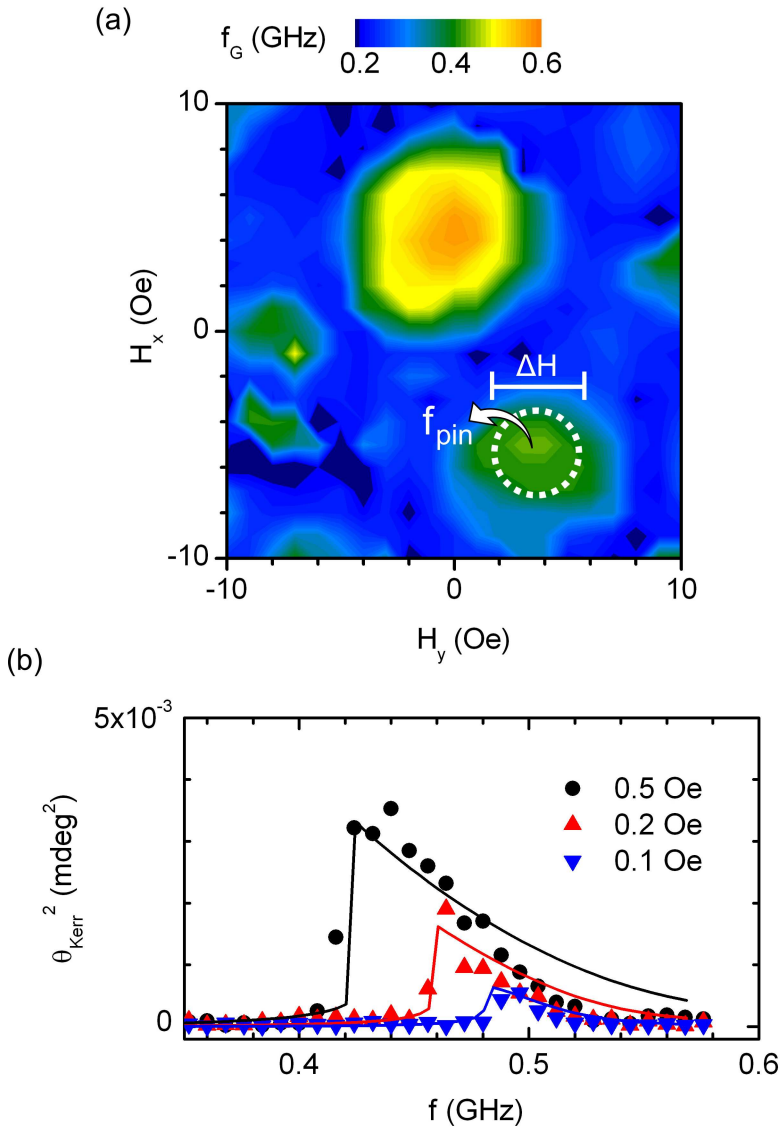

Figure 4.1: (a) Contour map of the gyrotropic frequency f_G for a 2 μm diameter disk. The dashed circle indicates one of the pinning sites within the measured spatial range. (b) Gyrotropic-mode spectra measured using CW excitation, showing results from the experiment (points) and the numerical calculations (solid lines) at different excitation amplitudes as labelled. The spectra were measured at the static fields H_x = -5 Oe and H_y = 3.5 Oe, which set the equilibrium position of the core at the center of the pinning site indicated by the dashed circle in (a). The fitting of the gyrotropic spectra provides independently the properties of the pinning site, which can be compared to those determined from (a).

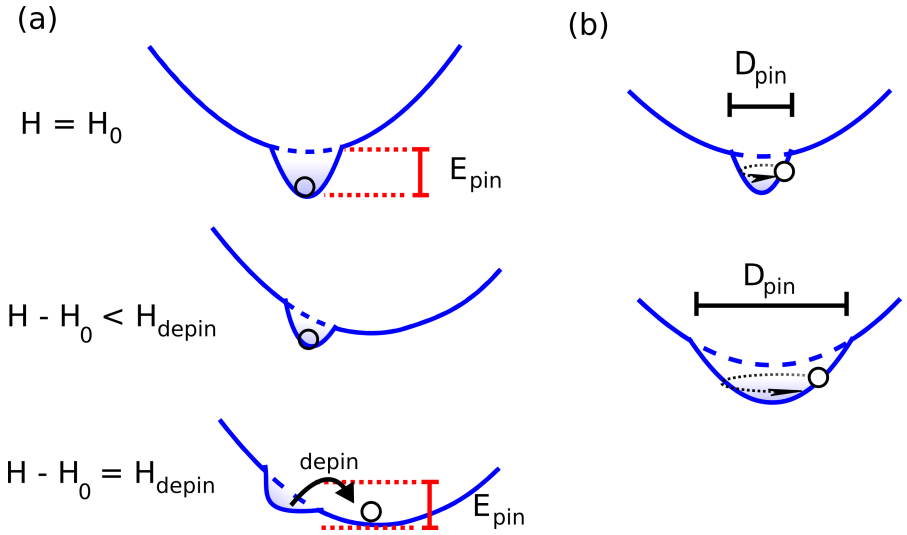

Figure 4.2: (a) Cartoons of energy profiles (solid lines) at different static fields H. The vortex core, indicated by a circle, is either inside or outside the pinning potential depending on the amplitude of H as labelled. H_0 represents the field required to move the vortex core to the center of a pinning site. H_{depin} is the field required to overcome the energy of pinning potential E_{pin}. (b) Cartoons of two energy profiles with the same pinning energy E_{pin}, but different pinning range D_{pin}. The upper one is expected to show a higher f_{pin} because of its smaller D_{pin} compared to the lower one.

the energy barrier. E_{pin}, i.e., the energy barrier, can be estimated from ΔH using

$$E_{pin} = \frac{1}{2}kr^2\left(\frac{1}{2}\Delta H\right). \tag{4.1}$$

4.1.2 Pinning Range

To determine the pinning range D_{pin}, which is the diameter of a pinning potential, we consider the simplest form of a pinning potential,

$$W_p(r) = \frac{1}{2}k_{pin}r^2, \tag{4.2}$$

where k_{pin} is the stiffness of the pinning potential. It should be noted that Eq. 4.2 is an approximation to the more realistic model, in which the pinning potential is of the Gaussian form as described in Ch. 3. In other words, here I focus on

estimating the range and energy of pinning potentials, and I ignore the details of the anharmonic characteristics that were discussed in Ch. 3.

There is a direct connection between f_{pin} and D_{pin}. It is instructive to compare two pinning potentials which have the same E_{pin}, but different D_{pin}, as shown in Fig. 4.2(b). Recall from Eq. 1.16 that f_G is proportional to the local curvature of the total magnetostatic energy. f_{pin} should be larger for the potential with a smaller D_{pin}, which has a larger curvature. To get a general formula for D_{pin}, by definition:

$$E_{pin} = W_p \left(\frac{1}{2} D_{pin} \right). \tag{4.3}$$

Eq. 4.2 and Eq. 4.3 lead to:

$$D_{pin} = 2\sqrt{\frac{2E_{pin}}{k_{pin}}}. \tag{4.4}$$

Since $f_{pin} = 2\pi G(k_u + k_{pin})$ and $f_u = 2\pi G k_u$ (Eq. 1.16), Eq. 4.4 leads to the expression of D_{pin}:

$$D_{pin} = 2\sqrt{\frac{E_{pin}}{\pi G(f_{pin} - f_u)}}. \tag{4.5}$$

4.1.3 Pinning Map and Spectra Fitting

Given the approach of fitting the gyrotropic-mode spectra (Ch. 3), we now have two independent approaches to determine the energy and range of a pinning site. The two approaches were applied to the same pinning site, which is indicated by the dashed circle in Fig. 4.1(a). For the first approach, the pinning map shows the ΔH and f_{pin} of the pinning site, which lead to the pinning energy and range 0.87 eV and 23 nm respectively, obtained from Eq. 4.1 and Eq. 4.5. For the second approach, after the data of Fig. 4.1(a) were taken, I applied the static fields H_x = -5 Oe and H_y = 3.5 Oe in order to position the vortex core at the same pinning site. At the pinning site I measured the gyrotropic-mode spectra at different amplitudes, as shown in Fig. 4.1(b). The spectra were fitted by using

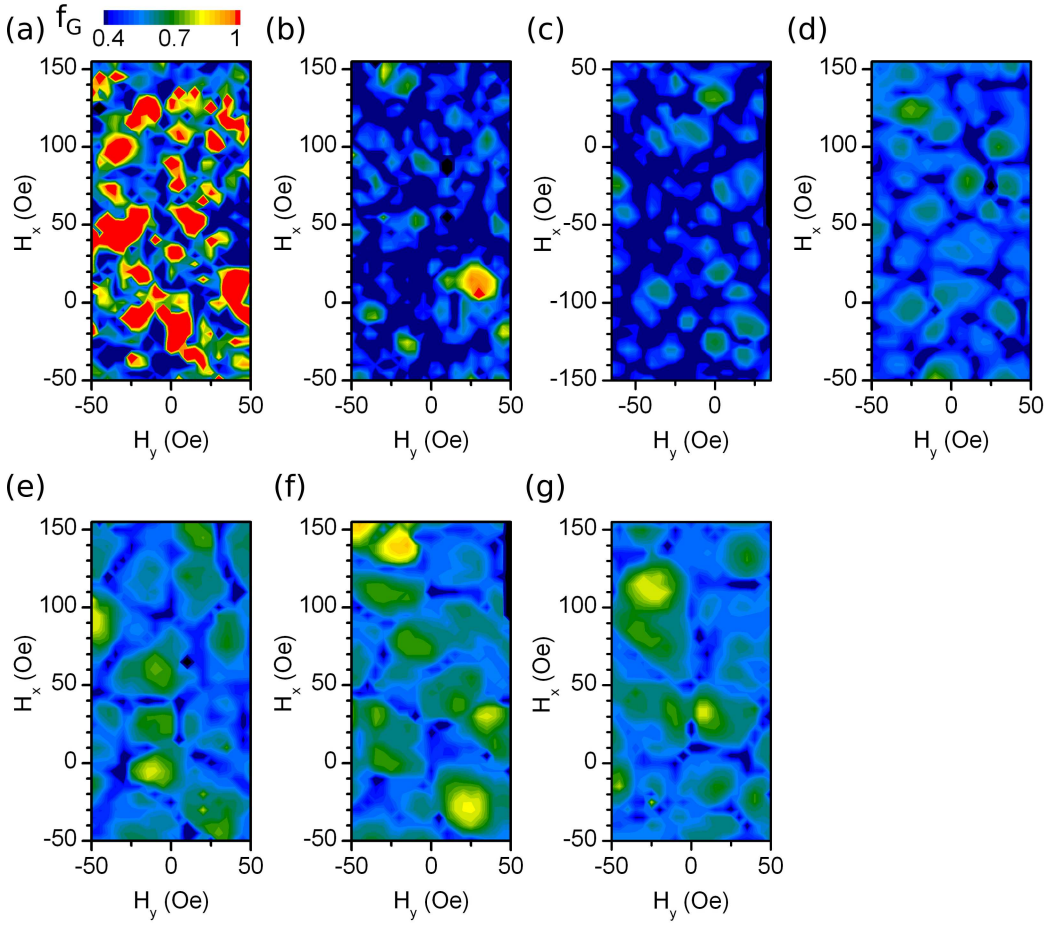

Figure 4.3: Contour maps of the gyrotropic frequency f_G as a function of the in-plane static field for disk thicknesses of (a) 20 nm, (b) 35 nm, (c) 50 nm, (d) 65 nm, (e) 80 nm, (f) 100 nm, and (g) 130 nm.

the procedure that is described in Sec. 3.1.3. The fitting reveals that the pinning energy and range are 0.93 eV and 19 nm respectively. The comparison of these two independent approaches indicates that the pinning-map approach provides reasonable estimations for the properties of a pinning site in a relatively short measurement time. In the following I will discuss the experimental results of seven samples measured by using the pinning-map approach.

4.1.4 Thickness Dependence of Pinning

I now discuss how the averaged energy and range of pinning sites change with the thickness of $Ni_{80}Fe_{20}$ films. Fig. 4.3 shows seven pinning maps, obtained from samples with different thickness L ranging from 20 nm to 130 nm (sample 1–7, see Sec. 2.1.1).

Properties of the pinning sites in Fig. 4.3 are summarized in Fig. 4.4, which shows the averaged pinning-site characteristics for each sample, i.e., $\langle f_{pin} \rangle$, D_{pin}, $\langle \Delta H \rangle$, and E_{pin}. Fig. 4.4(a) also shows the measured f_u, indicated by triangles. It should be noted that f_u was precisely determined by measuring f_G in the linear-dynamics regime to remove the influence of pinning, as discussed in Ch. 3. It is clear that the f_u increases with L, as expected from the analytical model and micromagnetic simulations [67, 69, 77, 78]. It is surprising, however, that $\langle f_{pin} \rangle$ is significantly higher in thinner disks, showing that the enhancement of f_G due to pinning ($\langle f_{pin} \rangle - f_u$) varies approximately as $1/L$.

Fig. 4.4(b) shows that the measured D_{pin} approximately matches the diameter of the vortex core at the disk surface (indicated by the solid curve) for all samples. The core diameter is obtained from the micromagnetic simulation shown in Fig. 1.7 of Sec. 1.4.2. Because of a large energy density associated with the core region, where the magnetization gradient is large, it is likely that local defects pin the vortex core region more effectively than the other regions of the vortex. Imperfections on length scales similar to the core diameter therefore cause the strongest pinning effects.

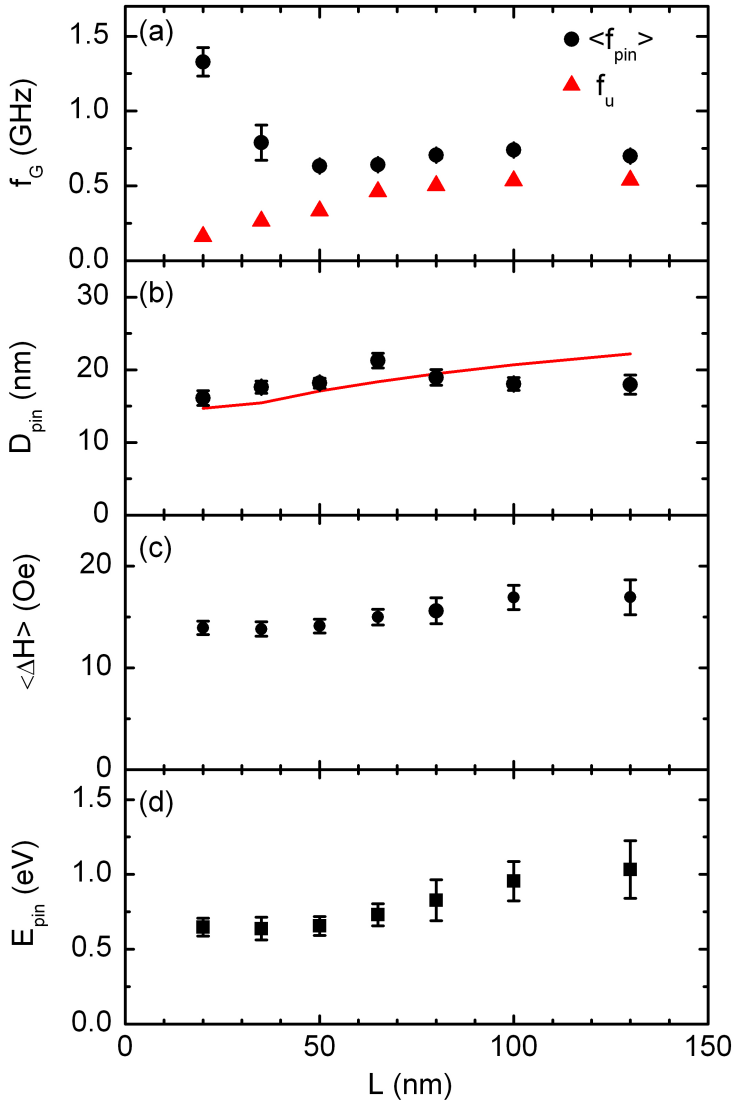

Figure 4.4: Thickness dependence of (a) the pinned frequency f_{pin} and the unpinned frequency f_u, (b) the pinning range D_{pin}, (c) the averaged depinning field ΔH, and (d) the pinning energy E_{pin}. The solid line in (b) is the diameter of the vortex core at the surface of the disk, obtained from micromagnetic simulations.

It should be noted that the above explanation for the observed pinning range is consistent with the consensus derived from models of domain wall pinning [24]. Specifically, pinning of domain wall motion is known to be most effective at defects with dimensions comparable to the wall width. However, to our knowledge this limiting-defect-size effect has been shown in experiments only through collective effects [52, 53, 93], in which the highest coercivities were observed when the grain or inclusion size in the film matched the estimated domain wall width. Here, because I directly identify the spatial range of the interaction between a single vortex and an individual pinning site (D_{pin}), which is set by the core diameter, my findings represent strong evidence for the predicted limiting-defect-size effect.

Additional information about the pinning defects can be obtained from the thickness dependence of $\langle E_{pin} \rangle$. If point defects in the bulk of the film (e.g., impurities, vacancies, and nonmagnetic inclusions) dominate the vortex pinning, $\langle E_{pin} \rangle$ should scale directly with L. On the other hand, if surface imperfections (e.g., roughness) dominate the vortex pinning, $\langle E_{pin} \rangle$ should be insensitive to L. Fig. 4.4(d) shows that the measured $\langle E_{pin} \rangle$ is relatively constant at small thickness and then drifts slightly upward with increasing L. The data suggest that the observed vortex pinning is dominated by surface imperfections.

4.2 Surface Roughness

4.2.1 Roughness Power Spectral Density

I now turn to analysis of the surface roughness, which was characterized by using tapping-mode AFM. (The AFM images were shown in Sec. 2.1.1.) Fig. 4.5(a) shows the power spectral density (PSD) of the surface roughness, obtained from the Fourier transform of the AFM images. The peak of the spectrum indicates the grain size, which increases with L, as is typical.

By integrating the spectrum, we can obtain the RMS roughness σ_{RMS}, which, however, does not account for the limiting-defect-size effect discussed in Sec 4.1.4.

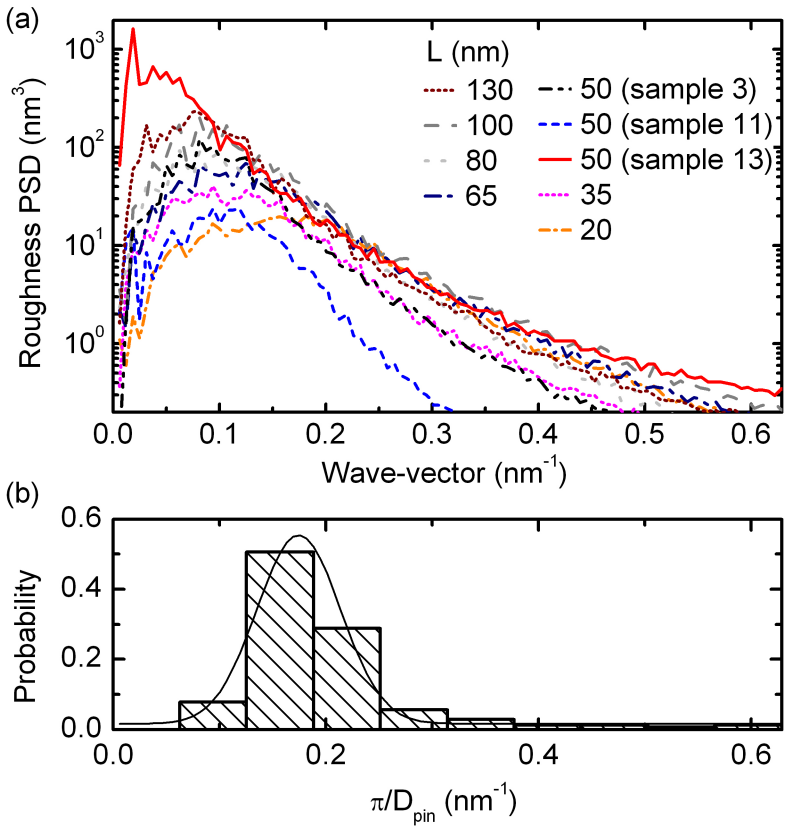

Figure 4.5: (a) Roughness power spectral density (PSD) as a function of wave-vector, obtained from the FFT of atomic force micrographs (AFM). (b) Probability distribution of $\pi/(D_{pin})$. The histogram consists of all pinning sites identified in Fig. 4.3(a)-(g). The solid line is a Gaussian fit to the histogram.

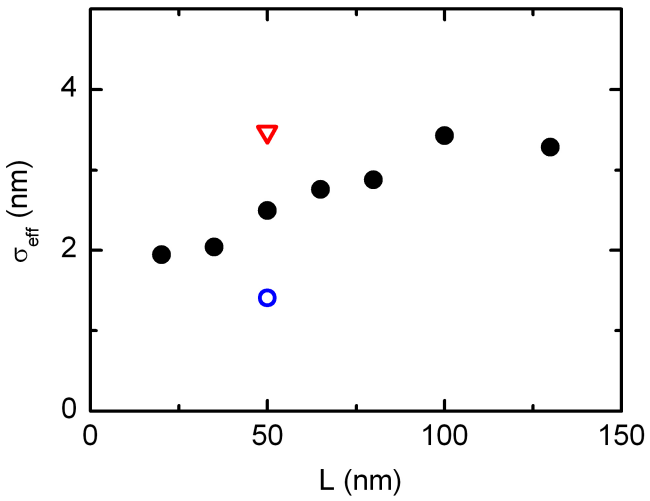

Figure 4.6: Effective roughness σ_{eff} versus the disk thickness L. Samples 1–7 are indicated by the filled circles. Samples 11 and 13 are indicated by the open circle and the open triangle respectively.

The spectrum shows the roughness at different length scales, and only the roughness on the length scale of the diameter of the vortex core should contribute to the vortex pinning. Therefore, the integration of the roughness PSD spectrum should include a weighting function. Although it is possible to develop a model of a weighting function based on the diameter of the core, I argue that a weighting function can be obtained experimentally from the measured probability distribution of D_{pin}. Fig. 4.5(b) shows the distribution of π/D_{pin}, which reflects the importance of defects at different length scales for contributing to the vortex pinning. I use π/D_{pin} as the relevant wave-vector $q = 2\pi/\lambda$, where λ is the wavelength of the fluctuations in the potential energy, because the measured D_{pin} corresponds to the FWHM of a pinning potential, which is approximately $\lambda/2$ in this case.

With this weighted integration procedure, an effective roughness σ_{eff} is obtained for each sample. Fig. 4.6 shows that σ_{eff} increases from approximately 2 to 4 nm as L is increased from 20 to 130 nm. For samples with the same growth conditions, the measured σ_{eff} varies roughly as $\sqrt{L}$, which is typical for sputtered

thin films, because the atoms of the thin film material fall on the substrate randomly during the thin-film deposition, resulting in a Gaussian distribution in the local thickness.

4.2.2 Dominant Mechanism of Pinning

The relationship between pinning and roughness can be seen in Fig. 4.7(a) and (b), which show E_{pin} as a function of σ_{RMS} and σ_{eff} respectively. Besides the samples discussed thus far (filled circles), two additional 50 nm thick samples are shown for comparison, indicated by open circles for sample 11 and open triangles for sample 13. Recall from Sec. 2.1.1 that sample 11 has smaller roughness compared to the original 50 nm sample (sample 3). Sample 13 has larger grain size ($\sim$ 100 nm) than samples 3 and 11 ($\sim$ 30 nm). Fig. 4.7(a) shows that there is no clear linear correlation between σ_{RMS} and E_{pin}. However, as shown in Fig. 4.7(b), it is clear that E_{pin} scales linearly with σ_{eff}, and the linear fit, shown as a solid line, intercepts the y-axis at approximately zero. This result indicates that the effective roughness is the dominant vortex pinning mechanism for these permalloy films.

The correlation between E_{pin} and σ_{eff} also explains the thickness dependence of E_{pin} shown in Fig. 4.4(d). The slight increase of E_{pin} with increasing L is due to the fact that σ_{eff} is larger for thicker disks (Fig. 4.6). Also consistent with this explaination, Fig. 4.8 shows that E_{pin}/σ_{eff} is independent of L.

Besides the correlation between E_{pin} and σ_{eff}, which clearly indicates the true source of the pinning, another important aspect of the findings discussed above is that I can now estimate how small the effective roughness would need to be in order to avoid this mechanism. I will consider that a pinning site is unimportant only if depinning of a vortex from that site can be thermally activated at room temperature on a typical laboratory time scale, e.g., 1 sec.

The critical pinning energy ΔE can be estimated by setting the characteristic

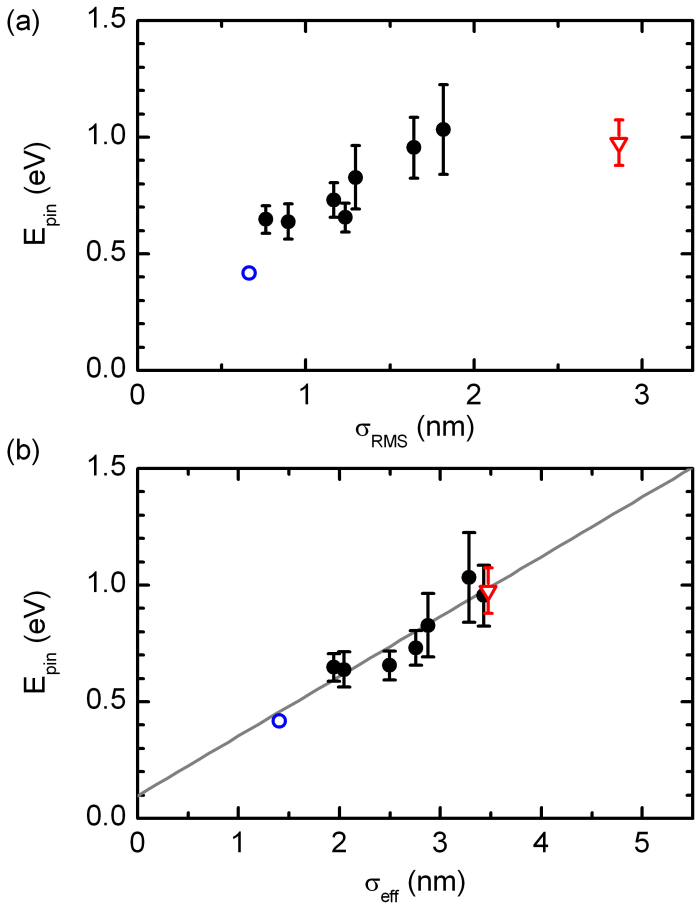

Figure 4.7: Pinning energy versus (a) the RMS roughness σ_{RMS}, and (b) the effective roughness (on the length scale of the core diameter) σ_{eff}. The solid line is a linear fit. Samples 1–7 are indicated by the filled circles. Samples 11 and 13 are indicated by the open circles and the open triangles respectively.

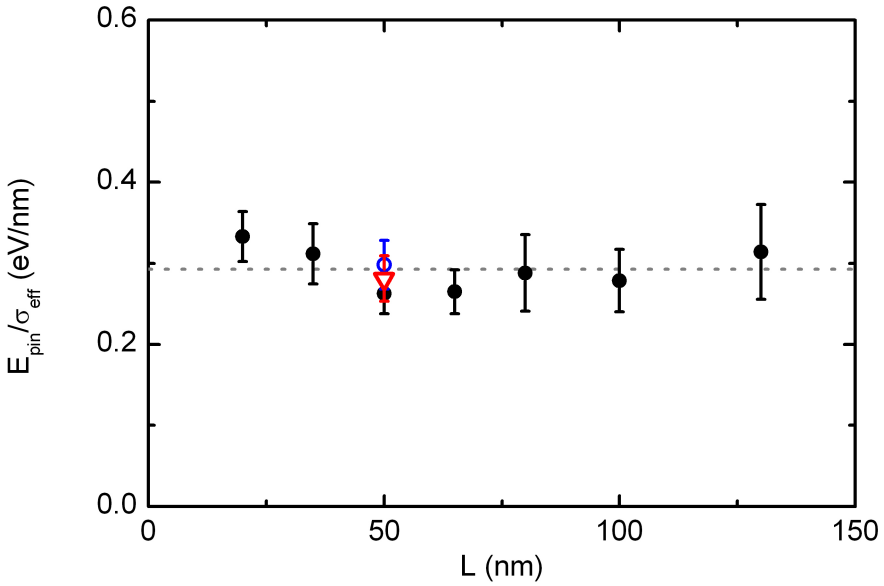

Figure 4.8: Pinning energy E_{pin} normalized by the effective roughness σ_{eff} versus disk thickness L. Samples 1–7 are indicated by the filled circles. Samples 11 and 13 are indicated by the open circle and the open triangle respectively. The dashed line indicates the average value of E_{pin}/σ_{eff}.

rate for thermally activated jumps to occur as 1 Hz:

$$f_0 \exp\left(\frac{-\Delta E}{k_B T}\right) = 1, \tag{4.6}$$

where $f_0 \sim 0.5$ GHz is the gyrotropic-mode frequency, which is the attempt frequency in this case. Solving Eq. 4.6 leads to $\Delta E \sim 0.5$ eV, below which a vortex can be thermally activated. Therefore, the data in Fig. 4.7(b) indicate that the effective roughness would need to be smaller than 1.5 nm to avoid vortex pinning.

To put this effective roughness value in perspective, I will consider its implication for films with various growth modes, as was originally pointed out by Chris Leighton. In the Volmer-Weber or island growth mode (often relevant to sputtered polycrystalline metal films) [94], roughness is significant and the lateral correlation length is directly linked to the grain size. Given that this length scale in most practical situations is on the same order of magnitude as the physically relevant pinning length scale (i.e., $\sim$ 20 nm, the vortex core diameter), the constraint $\sigma_{eff} << 1.5$ nm is a very stringent one, requiring grain sizes very different from the core diameter. In Frank-van der Merwe (i.e., layer-by-layer) or step-flow growth modes [94, 95] (potentially relevant to MBE-grown epitaxial metal films) the lateral correlation length of the roughness is set by the mean terrace width, and thus the vicinality of the substrate surface. Satisfying $\sigma_{eff} << 1.5$ nm may be possible, but even in this case it would require specific tailoring of the vicinality and terrace width to avoid the scale of the core diameter. Thus, I expect that the surface roughness pinning mechanism plays an important role for vortex pinning in virtually all soft ferromagnetic films. Similar length scale arguments apply to edge roughness in patterned thin film devices, as the length scale associated with the patterning probe is again likely on a similar scale to the vortex core.

Chapter 5

Dimensionality Crossover in Magnetic Vortex Dynamics

Recall from Sec. 1.4 that the dynamics of a magnetic vortex can be treated two-dimensionally (2D) and the gyrotropic frequency f_G is determined by L/D for a magnetic vortex in a thin disk (thickness $L <<$ diameter D). The model of vortex pinning discussed in Ch. 3 and Ch. 4 is also based on the magnetic vortices which are in the thin-disk regime. For sufficiently thick disks, the assumption of 2D vortex-core dynamics must break down, and the vortex-core dynamics along the normal-axis direction of the disk must become important. It is important to understand the properties of the 3D vortex-core dynamics and the critical thickness L_c, beyond which a new model of vortex dynamics is needed.

In this chapter, I will show the experimental results of f_G as a function of L, which varies from 20 to 300 nm. I will discuss a 2D-3D crossover of the gyrotropic mode at $L_c \sim 160$ nm for 1 μm diameter permalloy ($Ni_{80}Fe_{20}$) disks. The experimental results will be compared with quasi-3D micromagnetic simulations and will be explained using a simple 3D model of the vortex-core dynamics.

5.1 Thickness Dependence of the Gyrotropic mode Frequency

As already shown in Ch. 4, both the unpinned and pinned f_G can be measured in experiment [Fig. 4.4(a)]. I will focus on the unpinned f_G for the purposes of this chapter. Fig. 5.1 shows the thickness dependence of f_G over a large range of L (20 to 300 nm), obtained by the CW excitation technique (Sec. 2.2.3). The results from the 2D micromagnetic simulations are indicated by the dotted line. As noted in Sec. 1.4, the experimental results, as indicated by the black circles, show that f_G is proportional to L for thin disks ($L < 100$ nm), consistent with the 2D micromagnetic simulations as well as the analytical model (Eq. 1.16). In this region the vortex dynamics are well-explained by the 2D model (Sec. 1.4.4). For $L = 130$, 160, and 200 nm, the experimental values of f_G deviate from those of the 2D simulations, and an additional mode appears at higher frequencies. For $L = 300$ nm, only one mode is observed and the experimental value of f_G is close to that of the 2D simulation.

The existence of two modes is very surprising, because only one gyrotropic mode frequency exists if the core moves as a rigid body, as discussed in Sec. 1.4.4. The additional mode is not one of the spin-wave modes (Sec. 2.2.2), because the spin-wave modes are at much larger frequencies (> 5 GHz) than those shown in Fig. 5.1 [69]. I will show in the following that the two modes in Fig. 5.1 are both gyrotropic modes. In one mode the core oscillates uniformly through the thickness of the disk, while in the other mode the core oscillates with larger amplitude at the surfaces, with a node in the equatorial plane of the disk.

It is instructive to show the relative strengths of the two modes at different L. Fig. 5.2(a) shows the measured spectra for the thicknesses of 80, 100, 130, 160, and 200 nm. Data were obtained by using the the pulsed excitation technique (Sec. 2.2.2). For each sample I measured time scans at $\sim$ 900 different core positions, with a step size of $\sim$ 5 nm. An averaged FFT spectra of these time scans were obtained for each sample, and the effect of the fluctuations of f_G due

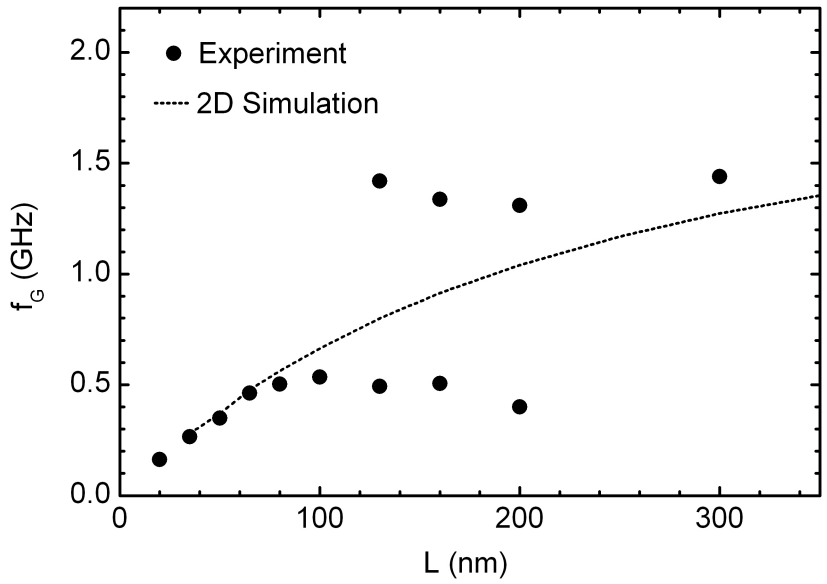

Figure 5.1: Thickness dependence of the gyrotropic mode frequencies. The experimental results for the unpinned frequency are indicated by the black circles. The results of the 2D simulations are indicated by the dotted line.

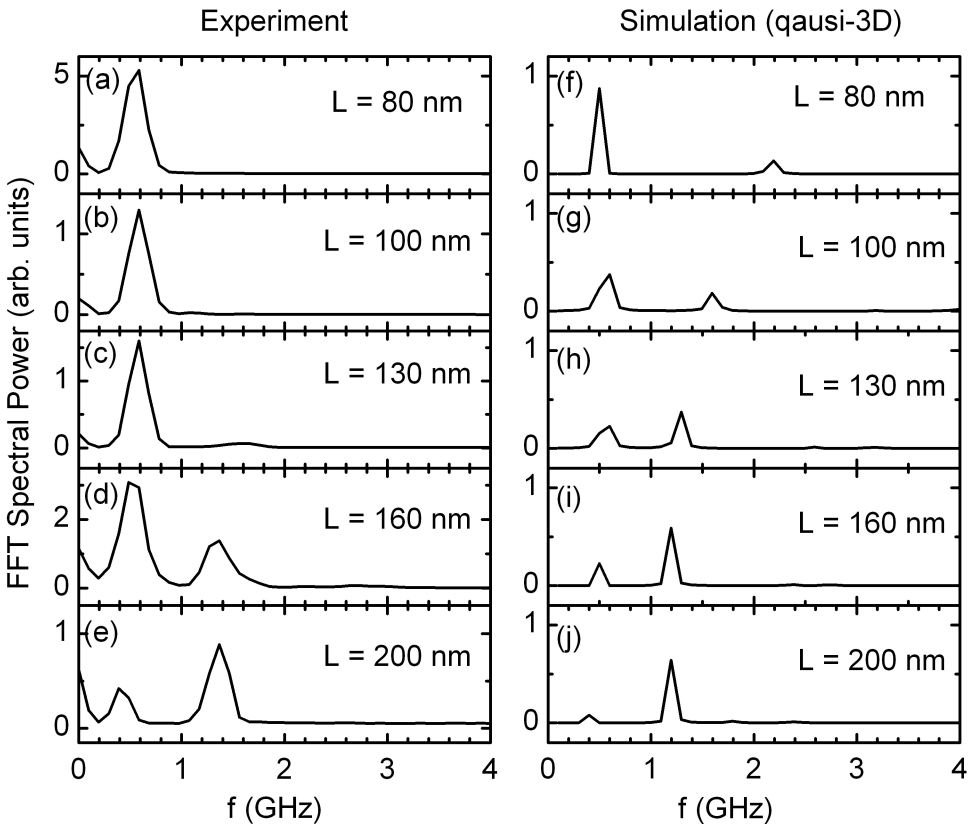

Figure 5.2: (a)-(e) Experimental response spectra for vortices in disks with different L. (f)-(j) Quasi-3D simulation results of the response spectra of vortices in disks with different thicknesses L. The simulation data were obtained from the spectrum of the surface layer in each disk.

to pinning can be minimized in this approach. Fig. 5.2 shows that two modes appear for the cases of 130, 160, and 200 nm, but not for the cases of 80 and 100 nm. At 130 nm, the power of the lower frequency mode is about a factor of 30 stronger than that of the higher frequency mode. At 160 nm, the lower frequency mode is about twice as strong as the higher frequency mode. At 200 nm, the higher frequency mode becomes the stronger mode, about twice as strong as the lower frequency one. It appears that there is a crossover of two modes, one with a strong response power and the other one with a weaker response power. This crossover will be discussed in detail in the following.

5.2 Quasi-3D Simulations

To get insight into the thickness dependence of f_G, I have simulated the vortex dynamics by using the quasi-3D approach discussed in Sec. 1.4.2. A 1 μm diameter disk is divided into cells of a size of $5\times5\times s$ nm^3, where $s = L/5$ is the dimension of the cell along the normal axis of the disk. In the micromagnetic simulations, the vortex dynamics are excited by a pulsed in-plane oriented magnetic field of the Gaussian form with a full width at half maximum of 180 ps. The magnetization dynamics are averaged within each of the 5 layers, revealing a spectrum at each layer of the disk.

From the micromagnetic simulations it becomes clear that there are two gyrotropic modes. Fig. 5.3 shows schematic representations of the two modes. In Fig. 5.3(a), the core oscillates uniformly through the thickness of the disk. This is the original gyrotropic mode, and it will be referred to as the zero-node mode. In Fig. 5.3(b), the core oscillates with a larger amplitude at the surface, and with a node in the equatorial plane of the disk. The core above the equatorial plane of the disk gyrates with a phase difference of π compared to the core below the equatorial plane. I will refer this mode [Fig. 5.3(b)] as the one-node mode.

Fig. 5.2(b) shows spectra from the simulation results at $L = 80$, 100, 130, 160,

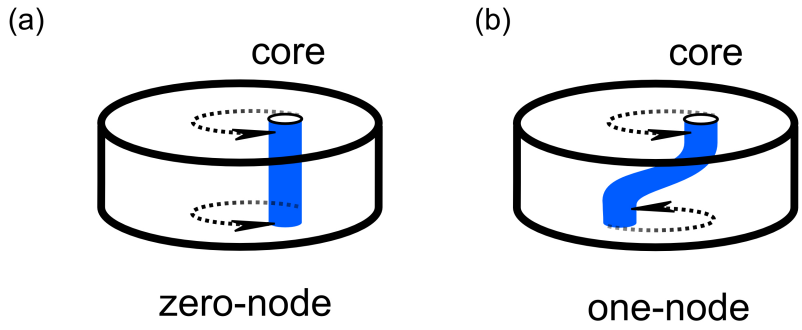

Figure 5.3: Schematic representations of the gyrotropic modes. (a) The zero-node mode. (b) The one-node mode. The vortex core is indicated by the shaded region. The directions of the gyration of the core are indicated by the dashed arrows.

and 200 nm. For $L = 80$ nm, the lower frequency peak corresponds to the zero-node mode, while the higher frequency peak corresponds to the one-node mode. For $L = 200$ nm, it is the opposite: the lower frequency peak corresponds to the one-node mode, while the higher frequency peak corresponds to the zero-node mode. The shift of the primary response power from the lower frequency mode to the higher one is also observed in the experimental results of Fig. 5.2(a). In the experiment, however, the one-node mode is not apparent for $L = 80$ and 100 nm. A possible reason for the discrepancy will be discussed later.

Fig. 5.4 shows the simulated f_G as a function L, providing a global picture of the gyrotropic modes. The values of f_G from the quasi-3D simulations, as indicated by the red squares, are close to those from the experimental results (black circles) for the entire thickness range shown in Fig. 5.4. Starting from the smallest L, the frequency of the one-node mode is much larger than that of the zero-node mode. The frequency of the zero-node mode increases with increasing L. This increasing trend can be well-presented by the values of f_G from the 2D simulations (black dotted line), because the zero-node mode is the only mode observed in the 2D simulations. On the other hand, the frequency of the one-node mode decreases with increasing L, as indicated schematically by the red dashed curve. These two modes crossover at about $L \sim 160$ nm. The true crossing of

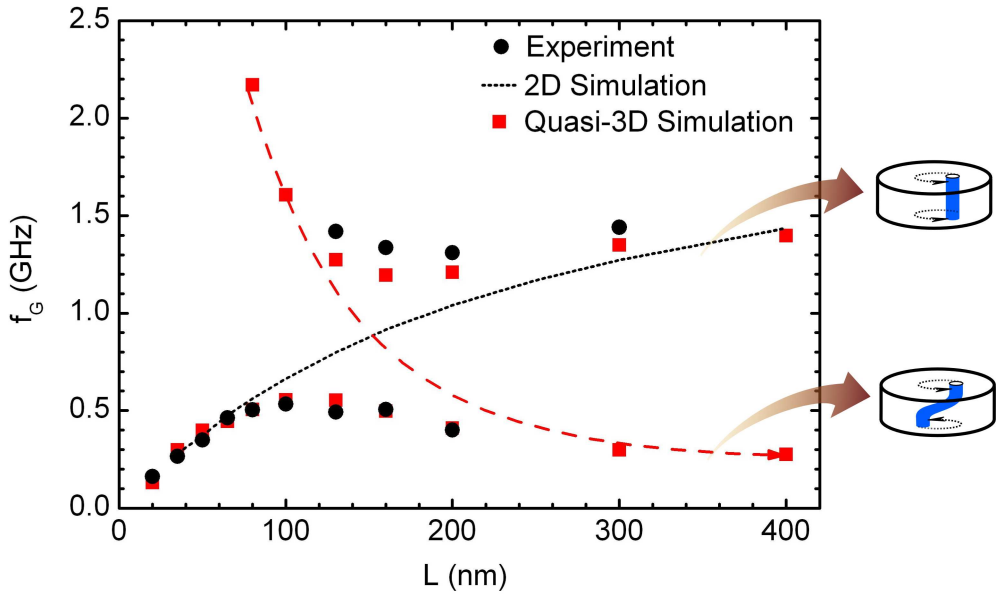

Figure 5.4: Thickness dependence of the gyrotropic mode frequencies. The experimental results and the 2D simulations are indicated by the black circles and dotted line respectively. The quasi-3D simulations are indicated by the red squares. The dashed curve is a guide to the eyes for the thickness dependence of the one-node mode (see text). The inset shows cartoons of the zero-node mode and the one-node mode, corresponding to the increasing f_G with increasing L (dotted line) and the decreasing f_G with increasing L (dashed line) respectively, as indicated by the arrows.

the eigenmodes, however, is forbidden. Instead, the eigenmodes in the crossover regime become the superposition of the zero-node mode and the one-node mode, resulting in an apparent mode repulsion, which is typical for the crossover of modes in dynamical systems.

The superposition of the zero-node mode and the one-node mode can be seen from the simulated gyrotropic mode spectrum for each of the five layers at three representative L at 80, 160 and 200 nm, as shown Fig. 5.5. For the case of $L = 80$ nm, the spectra show two primary peaks at 0.5 and 2.2 GHz. The lower frequency peak corresponds to the zero-node mode, and the power of the peak is the same for the layers 1 to 5. The higher frequency peak corresponds to the one-node mode, with the power decreasing to zero in layers 1 to 3, and increasing in layers 3 to 5. For the case of $L = 160$ nm (in the crossover region), the simulations show no clear indication for the zero-node and one-node modes. The power of the two primary peaks at 0.5 and 1.2 GHz both decrease from the surface layer to the mid-layer of the disk, but neither of them show a true node at the layer 3. This is consistent with the discussion above that, in the crossover region, the two observed modes are superpositions of the zero-node and one-node modes. For the case of $L = 200$ nm, the spectra show two primary peaks at 0.4 and 1.2 GHz. In contrast to the case at $L = 80$ nm, it is the higher frequency mode that has the characteristics of the zero-node mode.

In the micromagnetic simulations, the excitation field is uniform along the normal axis of the disk. If the eigenmodes of the system are truly the zero-node mode and one-node mode, the excitation field should only excite the zero-node mode because of symmetry. As discussed above, in the crossover region superpositions of the modes occurs. This is why for the case of $L = 160$ nm in Fig. 5.5 both modes have similar response power. Away from the crossover region, superpositions of the modes are less apparent than those in the corssover region, resulting in the weaker response of the one-node mode away from the crossover region.

Similar to the micromagnetic simulations, in experiment the excitation field is

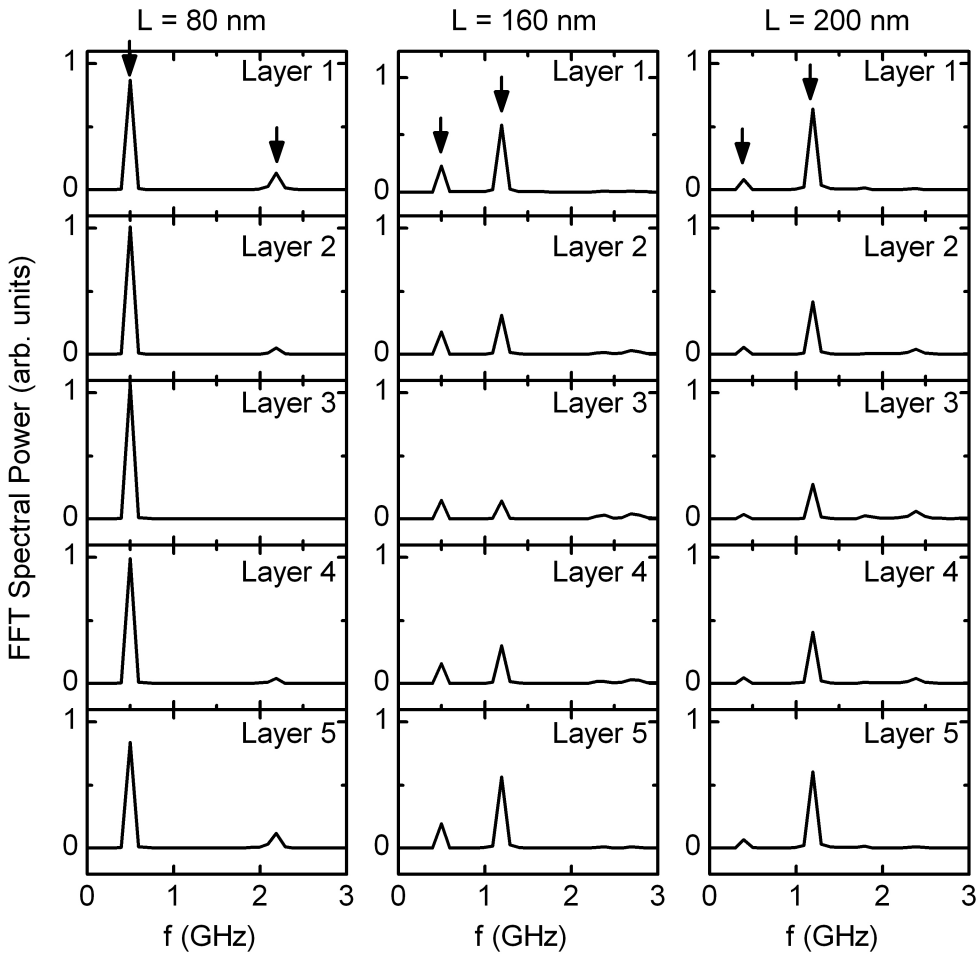

Figure 5.5: Gyrotropic mode spectra of 1 μm diameter $Ni_{80}Fe_{20}$ disks at three representative thickness L = 80, 160, and 200 nm. Data were obtained from quasi-3D simulations, in which the disks were divided by five layers. The arrows indicate the frequencies of the two gyrotropic modes discussed in the text.

uniform along the normal axis of the disk. The experimental results, however, do not show the one-node mode when L is away from the crossover region, based on the observed f_G (Fig. 5.4). It is likely that the response of the one-node mode is too weak to be resolved in experiment when L is away from the crossover region.

The underlying physics of the distinctive thickness dependences for the two gyrotropic modes can be explained by the dominant energies associated with the modes. Recall from Sec. 1.4.4 that, for the zero-node mode, the vortex remains rigid, so that f_G of the zero-node mode is determined by the magnetostatic energy. In this case the vortex core can be treated as a particle oscillating in a parabolic potential of the magnetostatic energy. The curvature of the potential increases with increasing L, resulting the increasing trend of f_G with increasing L for the zero-node mode. In contrast, in the one-node mode the gyration of the vortex core is associated with the distortion of the vortex core, and the energy associated with the one-node mode is dominated by the exchange energy. Recall from Sec. 1.1.1 that the gradient of magnetization causes the exchange energy. The magnetization gradient due to the distortion of the core decreases with increasing L, so that f_G of the one-node mode decreases with increasing L. A rigorous analytical treatment is needed to fully understand the physics of the one-node mode, and the results discussed in this chapter will provide the foundation for the development of the analytical model.

Chapter 6

Summary

In this dissertation, I have reported on investigations of the linear and non-linear regimes of vortex dynamics in a single magnetic disk over a large dynamic range in drive amplitude. The spectra reveal important information about transitions between different dynamical regimes. I have identified three distinct regimes of vortex behavior: the pinned regime, a linear response regime corresponding to ordinary gyrotropic motion, and finally the core reversal regime. In addition to core reversal at high amplitudes, a second class of non-linear dynamics is associated with the depinning transition, in which the response amplitude changes hysteretically as a function of the excitation amplitude. The spectrum of the vortex oscillations near the depinning threshold can be used to measure the strength and range of a pinning potential, and a simple model captures the physics of the depinning transition, including the existence of two metastable states (pinned and unpinned). A direct observation of the pinning process in the time domain further supports the concept of a localized pinning potential. This complete picture of vortex dynamics including pinning will facilitate further developments of spintronic devices that contain vortices, such as nanocontacts, nanopillars, magnetic tunnel junctions, and write heads in computer hard disk drives.

Regarding the dominant mechanism of the vortex pinning, I have shown that the dynamics of a single vortex allow for quantifying the energy and length scales

associated with an individual pinning site. I have shown that, from studying the vortex pinning as a function of film thickness, the measured pinning range, approximately 20 nm, is identical to the diameter of the vortex core, demonstrating that the pinning defects interact only with the core of the vortex. The dominant pinning defects are located on the surfaces. I have demonstrated quantitatively that the pinning is correlated not with the RMS surface roughness but rather with the roughness on the lateral length scale of the core diameter, i.e. an effective roughness. This pinning mechanism likely sets the minimum pinning energy for vortex motion in most soft ferromagnetic thin-film devices, such as vortex domain walls in nanowires. These findings therefore provide important insights into the properties of magnetic vortices in real materials.

I have shown that the dynamics of the vortex core can be treated in 2D for thin disks. Besides the 2D gyrotropic mode, i.e. the zero-node mode, the one-node mode has much larger f_G than the zero-node mode in thin disks. I have shown that the opposite thickness dependence of the two modes results in a crossover region, at which the eigenmodes are the superposition of the zero-node and one-node modes. The disk thickness at which the crossover occurs can be defined as a critical thickness, which is determined by the disk diameter and the material. For example, I have demonstrated that the critical thickness is $\sim$ 160 nm for 1 μm diameter $Ni_{80}Fe_{20}$ disks.

For future directions, the experimental techniques of characterizing pinning defects in $Ni_{80}Fe_{20}$ can be applied to other soft ferromagnets. Recently, I have successfully observed the gyrotropic mode of a single vortex in micron-sized disks that are made of Co, Ni, and CoFe films. It will be interesting to investigate the pinning mechanisms in these materials.

Another interesting research direction is to study the pinning of a pair of vortices instead of a single vortex. Two coupled vortices can be obtained from ferromagnetic films that are patterned into stadium shapes. It is likely that the microscopic pinning mechanism will be the same as a single vortex. The competition between the pinning strength of the defects and the coupling strength

between the vortices may lead to interesting magnetization dynamics. The study of two vortices will also suggest how the pinning of a single vortex is related to the pinning of other magnetic structures, such as cross tie walls, which consist of chains of coupled vortices and antivortices.

References

[1] L. Berger, J. Appl. Phys. **49**, 2156 (1978).

[2] L. Berger, J. Appl. Phys. **55**, 1954 (1984).

[3] P. P. Freitas and L. Berger, J. Appl. Phys. **57**, 1266 (1985).

[4] L. Berger, Phys. Rev. B **54**, 9353 (1996).

[5] D. C. Ralph and M. D. Stiles, J. Magn. Magn. Mater. **320**, 1190 (2008).

[6] G. S. D. Beach, M. Tsoi, and J. L. Erskine, J. Magn. Magn. Mater. **320**, 1272 (2008).

[7] J. C. Slonczewski, J. Magn. Magn. Mater. **159**, L1 (1996).

[8] J. C. Slonczewski, J. Magn. Magn. Mater. **195**, L261 (1999).

[9] D. Berkov and J. Miltat, J. Magn. Magn. Mater. **320**, 1238 (2008).

[10] P. M. Haney, R. A. Duine, A. Núñez, and A. H. MacDonald, J. Magn. Magn. Mater. **320**, 1300 (2008).

[11] J. A. Katine and E. E. Fullerton, J. Magn. Magn. Mater. **320**, 1217 (2008).

[12] H. Ohno and T. Dietl, J. Magn. Magn. Mater. **320**, 1293 (2008).

[13] T. J. Silva and W. H. Rippard, J. Magn. Magn. Mater. **320**, 1260 (2008).

[14] J. Z. Sun and D. C. Ralph, J. Magn. Magn. Mater. **320**, 1227 (2008).

[15] Y. Tserkovnyak, A. Brataas, and G. E. W. Bauer, J. Magn. Magn. Mater. **320**, 1282 (2008).

[16] J. P. van der Ziel, P. S. Pershan, and L. D. Malmstrom, Phys. Rev. Lett. **15**, 190 (1965).

[17] A. V. Kimel, A. Kirilyuk, P. A. Usachev, R. V. Pisarev, A. M. Balbashov, and T. Rasing, Nature **435**, 655 (2005).

[18] C. D. Stanciu, F. Hansteen, A. V. Kimel, A. Kirilyuk, A. Tsukamoto, A. Itoh, and T. Rasing, Phys. Rev. Lett. **99**, 047601 (2007).

[19] A. M. Kalashnikova, A. V. Kimel, R. V. Pisarev, V. N. Gridnev, A. Kirilyuk, and T. Rasing, Phys. Rev. Lett. **99**, 167205 (2007).

[20] K. Vahaplar, A. M. Kalashnikova, A. V. Kimel, D. Hinzke, U. Nowak, R. Chantrell, A. Tsukamoto, A. Itoh, A. Kirilyuk, and T. Rasing, Phys. Rev. Lett. **103**, 117201 (2009).

[21] D. Hinzke and U. Nowak, Phys. Rev. Lett. **107**, 027205 (2011).

[22] R. C. O'Handley, *Modern Magnetic Materials: Principles and Applications* (Wiley-Interscience, New York, 1999).

[23] Y. Tserkovnyak, A. Brataas, G. E. W. Bauer, and B. I. Halperin, Rev. Mod. Phys. **77**, 1375 (2005).

[24] H. Alex and S. Rudolf, *Magnetic domains : the analysis of magnetic microstructures* (Springer, Berlin ; New York, 1998).

[25] M. R. Scheinfein, *LLG micromagnetics simulator, v.2.55* (2004).

[26] H. Barkhausen, Z. Phys **20**, 401 (1919).

[27] R. F. Soohoo, J. Appl. Phys. **67**, 5639 (1990).

[28] R. F. Soohoo, J. Appl. Phys. **69**, 5871 (1991).

[29] J. R. Barnes, S. J. O′Shea, and M. E. Welland, J. Appl. Phys. **76**, 418 (1994).

[30] K.-J. Kim, J.-C. Lee, S.-M. Ahn, K.-S. Lee, C.-W. Lee, Y. J. Cho, S. Seo, K.-H. Shin, S.-B. Choe, and H.-W. Lee, Nature **458**, 740 (2009).

[31] P. Bak, C. Tang, and K. Wiesenfeld, Phys. Rev. Lett. **59**, 381 (1987).

[32] P. J. Cote and L. V. Meisel, Phys. Rev. Lett. **67**, 1334 (1991).

[33] E. Puppin, Phys. Rev. Lett. **84**, 5415 (2000).

[34] A. Schwarz, M. Liebmann, U. Kaiser, R. Wiesendanger, T. W. Noh, and D. W. Kim, Phys. Rev. Lett. **92**, 077206 (2004).

[35] J. P. Sethna, K. A. Dahmen, and C. R. Myers, Nature **410**, 242 (2001).

[36] S. Zapperi, P. Cizeau, G. Durin, and H. E. Stanley, Phys. Rev. B **58**, 6353 (1998).

[37] D.-H. Kim, S.-B. Choe, and S.-C. Shin, Phys. Rev. Lett. **90**, 087203 (2003).

[38] P. Chauve, T. Giamarchi, and P. Le Doussal, Phys. Rev. B **62**, 6241 (2000).

[39] P. J. Metaxas, J. P. Jamet, A. Mougin, M. Cormier, J. Ferre, V. Baltz, B. Rodmacq, B. Dieny, and R. L. Stamps, Phys. Rev. Lett. **99**, 217208 (2007).

[40] S. Lemerle, J. Ferré, C. Chappert, V. Mathet, T. Giamarchi, and P. Le Doussal, Phys. Rev. Lett. **80**, 849 (1998).

[41] M. Yamanouchi, J. Ieda, F. Matsukura, S. E. Barnes, S. Maekawa, and H. Ohno, Science **317**, 1726 (2007).

[42] R. A. Duine and C. M. Smith, Phys. Rev. B **77**, 094434 (2008).

[43] A. B. Kolton, G. Schehr, and P. Le Doussal, Phys. Rev. Lett. **103**, 160602 (2009).

[44] L. San Emeterio Alvarez, K.-Y. Wang, S. Lepadatu, S. Landi, S. J. Bending, and C. H. Marrows, Phys. Rev. Lett. **104**, 137205 (2010).

[45] N. L. Schryer and L. R. Walker, J. Appl. Phys. **45**, 5406 (1974).

[46] A. P. Malozemoff and J. C. Slonczewski, *Magnetic Domain Walls in Bubble Materials* (Academic Press, New York, 1979).

[47] S. Konishi, S. Yamada, and T. Kusuda, IEEE Trans. Magn. **7**, 722 (1971).

[48] G. S. D. Beach, C. Nistor, C. Knutson, M. Tsoi, and J. L. Erskine, Nat. Mater. **4**, 741 (2005).

[49] M. Hayashi, L. Thomas, C. Rettner, R. Moriya, and S. S. P. Parkin, Nat. Phys. **3**, 21 (2007).

[50] K. Fukumoto, W. Kuch, J. Vogel, J. Camarero, S. Pizzini, F. Offi, Y. Pennec, M. Bonfim, A. Fontaine, and J. Kirschner, J. Magn. Magn. Mater. **293**, 863 (2005).

[51] J. C. Brice, J. A. Cundall, and A. P. King, J. Mater. Sci. **1**, 170 (1966).

[52] L. J. Dijkstra and C. Wert, Phys. Rev. **79**, 979 (1950).

[53] G. Herzer, IEEE Trans. Magn. **26**, 1397 (1990).

[54] M. Li, Y.-P. Zhao, G.-C. Wang, and H.-G. Min, J. Appl. Phys. **83**, 6287 (1998).

[55] D. A. Allwood, G. Xiong, C. C. Faulkner, D. Atkinson, D. Petit, and R. P. Cowburn, Science **309**, 1688 (2005).

[56] S. S. P. Parkin, M. Hayashi, and L. Thomas, Science **320**, 190 (2008).

[57] X. Jiang, L. Thomas, R. Moriya, and S. S. P. Parkin, Nano Lett. **11**, 96 (2011).

[58] T. Shinjo, T. Okuno, R. Hassdorf, K. Shigeto, and T. Ono, Science **289**, 930 (2000).

[59] A. Aharoni, J. Appl. Phys. **68**, 2892 (1990).

[60] N. A. Usov and S. E. Peschany, J. Magn. Magn. Mater. **118**, L290 (1993).

[61] J. Raabe, R. Pulwey, R. Sattler, T. Schweinbock, J. Zweck, and D. Weiss, J. Appl. Phys. **88**, 4437 (2000).

[62] B. E. Argyle, E. Terrenzio, and J. C. Slonczewski, Phys. Rev. Lett. **53**, 190 (1984).

[63] P. Fischer, M.-Y. Im, S. Kasai, K. Yamada, T. Ono, and A. Thiaville, Phys. Rev. B **83**, 212402 (2011).

[64] R. L. Compton, T. Y. Chen, and P. A. Crowell, Phys. Rev. B **81**, 144412 (2010).

[65] R. L. Compton and P. A. Crowell, Phys. Rev. Lett. **97**, 137202 (2006).

[66] R. L. Compton, *Vortex Pinning and Dynamics*, unpublished Ph.D. Thesis (University of Minnesota, Minneapolis, 2007).

[67] J. P. Park, P. Eames, D. M. Engebretson, J. Berezovsky, and P. A. Crowell, Phys. Rev. B **67**, 020403 (2003).

[68] M. Buess, R. Höllinger, T. Haug, K. Perzlmaier, U. Krey, D. Pescia, M. R. Scheinfein, D. Weiss, and C. H. Back, Phys. Rev. Lett. **93**, 077207 (2004).

[69] J. P. Park and P. A. Crowell, Phys. Rev. Lett. **95**, 167201 (2005).

[70] K. W. Chou, A. Puzic, H. Stoll, D. Dolgos, G. Schütz, B. Van Waeyenberge, A. Vansteenkiste, T. Tyliszczak, G. Woltersdorf, and C. H. Back, Appl. Phys. Lett. **90**, 202505 (2007).

[71] B. Van Waeyenberge, A. Puzic, H. Stoll, K. W. Chou, T. Tyliszczak, R. Hertel, M. Fähnle, H. Brückl, K. Rott, G. Reiss, et al., Nature **444**, 461 (2006).

[72] A. Vansteenkiste, K. W. Chou, M. Weigand, M. Curcic, V. Sackmann, H. Stoll, T. Tyliszczak, G. Woltersdorf, C. H. Back, G. Schutz, et al., Nat. Phys. **5**, 332 (2009).

[73] M. Weigand, B. Van Waeyenberge, A. Vansteenkiste, M. Curcic, V. Sackmann, H. Stoll, T. Tyliszczak, K. Kaznatcheev, D. Bertwistle, G. Woltersdorf, et al., Phys. Rev. Lett. **102**, 077201 (2009).

[74] S.-B. Choe, Y. Acremann, A. Scholl, A. Bauer, A. Doran, J. Stohr, and H. A. Padmore, Science **304**, 420 (2004).

[75] J. Raabe, C. Quitmann, C. H. Back, F. Nolting, S. Johnson, and C. Buehler, Phys. Rev. Lett. **94**, 217204 (2005).

[76] K. Y. Guslienko, X. F. Han, D. J. Keavney, R. Divan, and S. D. Bader, Phys. Rev. Lett. **96**, 067205 (2006).

[77] K. Y. Guslienko, B. A. Ivanov, V. Novosad, Y. Otani, H. Shima, and K. Fukamichi, J. Appl. Phys. **91**, 8037 (2002).

[78] V. Novosad, F. Y. Fradin, P. E. Roy, K. S. Buchanan, K. Y. Guslienko, and S. D. Bader, Phys. Rev. B **72**, 024455 (2005).

[79] K. Y. Guslienko, Appl. Phys. Lett. **89**, 022510 (2006).

[80] A. A. Thiele, Phys. Rev. Lett. **30**, 230 (1973).

[81] D. L. Huber, Phys. Rev. B **26**, 3758 (1982).

[82] K.-S. Lee and S.-K. Kim, Phys. Rev. B **78**, 014405 (2008).

[83] K. S. Buchanan, M. Grimsditch, F. Y. Fradin, S. D. Bader, and V. Novosad, Phys. Rev. Lett. **99**, 267201 (2007).

[84] K. Y. Guslienko, R. H. Heredero, and O. Chubykalo-Fesenko, Phys. Rev. B **82**, 014402 (2010).

[85] K. Yamada, S. Kasai, Y. Nakatani, K. Kobayashi, H. Kohno, A. Thiaville, and T. Ono, Nat. Mater. **6**, 270 (2007).

[86] B. Pigeau, G. de Loubens, O. Klein, A. Riegler, F. Lochner, G. Schmidt, and L. W. Molenkamp, Nat. Phys. **7**, 26 (2011).

[87] T. Uhlig, M. Rahm, C. Dietrich, R. Höllinger, M. Heumann, D. Weiss, and J. Zweck, Phys. Rev. Lett. **95**, 237205 (2005).

[88] W. K. Hiebert, A. Stankiewicz, and M. R. Freeman, Phys. Rev. Lett. **79**, 1134 (1997).

[89] J. P. Park, *Spin Dynamics in Magnetic Vortex Structures*, unpublished Ph.D. Thesis (University of Minnesota, Minneapolis, 2005).

[90] T. Y. Chen and P. A. Crowell, IEEE Trans. Magn. **46**, 1457 (2010).

[91] X. M. Cheng, K. S. Buchanan, R. Divan, K. Y. Guslienko, and D. J. Keavney, Phys. Rev. B **79**, 172411 (2009).

[92] H. Min, R. D. McMichael, J. Miltat, and M. D. Stiles, Phys. Rev. B **83**, 064411 (2011).

[93] R. C. O′Handley, J. Megusar, S.-W. Sun, Y. Hara, and N. J. Grant, J. Appl. Phys. **57**, 3563 (1985).

[94] K. Oura, V. G. Lifshits, A. A. Saranin, A. V. Zotov, and M. Katayama, *Surface Science: An Introduction* (Springer, Berlin, 2003).

[95] A. Pimpinelli and J. Villain, *Physics of Crystal Growth* (Cambridge University Press, Cambridge, 1998).

Appendix A

Details of Magnetic Disk Fabrication

This appendix explains the detailed processing procedure I used to fabricate the $Ni_{80}Fe_{20}$ disks studied in this dissertation. A general overview of the process is discussed in Sec. 2.1.2.

A.1 Details of the Device Fabrication Procedure

Before beginning the fabrication process, the wafers of the $Ni_{80}Fe_{20}$ films must first be cleaved into a piece of appropriate size; the devices studied in this dissertation were approximately 5×5 mm^2.

I. Spin PMGI/PMMA Bilayer Resist:

1. Prepare the PMGI resist by mixing PMGI SF6 with Type T thinner with a ratio of 2 to 3. For example, this can be achieved by mixing 80 ml of SF9 (9%) with 220 ml of T thinner.
2. Prepare the PMMA resist by mixing 12 ml of 495k PMMA A9 with 15 ml of Type A thinner.

3. Clean the sample with solvents, N2 dry, and check under microscope.
4. Prebake the sample at 105 C; 1 min on hotplate.
5. Spin PMGI at 4000 rpm for 20 seconds. If the sample is small ($<5\times5$ mm^2), set the Headway spinner at 3000 rpm and ramp to 4000 rpm. This will prevent pooling of a resist at the edges. If it still pools, start the spin at 4000 rpm immediately.
6. Bake the sample at 250C for 5 min using a hotplate. Let the sample cool $\sim$ 1 to 2 minutes.
7. Spin PMMA by ramping slowly to 4000 rpm for 40 sec at the top speed.
8. Bake the sample at 180 C for 3 minutes on a hotplate.
9. If results are unsatisfactory, use NMP and O2 asher to remove the resists and start over.

II. Electron Beam Lithography (Vistec EBPG5000+):

1. Vent the load lock, load samples, and then pump down.
2. Use the command "ce cjob" to check the design and to export the .job file
3. Wait until the pressure is below 4×10^{-5} Torr.
4. Use the command "subl 1" or "subl 2" to load the holder.
5. Use the command "pg select holder" to select the holder. For the small piece holder the ID number is 3.
6. Use the command "mvm" to check the holder.
7. Use the command "pg measure current" to measure the current.
8. Use the command "pg move pos [X]mm,[Y]mm –rel" to move the electron gun to the center of the sample at (X,Y).

9. Use the command "job [FILENAME.job] 3 0 [X in μm],[Y in μm]" to start writing the pattern.
10. Use the command "pg archive restore beam 1nA_300um_6.beam_100" to restore the beam to the latest calibrated beam file.
11. Use the command "subu 1" to unload the holder.
12. Unload the sample and pump down the load lock.

III. Develop:

1. Develop PMMA in MIBK:IPA :: 1:3 for 30 sec. Rinse in IPA to stop.
2. Check under the microscope. Developed pattern has a gray color. (High dose regions might show brighter color.)
3. Develop PMGI in Shipley CD-26:IPA :: 1:40 for 30 sec. Rinse in IPA to stop develop and blow dry.
4. Inspect features using optical microscope.

IV. Deposit Ti (hard mask) and lift-off:

1. E-beam evaporate 70 nm thick Ti at $\sim$ 1 Å/s. The pressure during deposition is $\sim 2 \times 10^{-6}$ Torr. The deposition of Ti can be done using either the CHA E-beam evaporator or the Temescal E-beam evaporator. (The Ti thickness 70 nm is optimized to process $Ni_{80}Fe_{20}$ films up to 300 nm thick.)
2. Place several cover glass slips with the sample to deposit witness Ti films on the cover glass slips.
3. After the deposition, lift-off the Ti pattern in NMP on an 80 C hotplate for 5-10 minutes. The resist should get lumpy on the sample as it lifts off. (Avoid sonication since this can destroy the smallest features.)

4. Rinse the sample in acetone/ methanol/ IPA/ DI water and blow dry.

V. Dry Etch Recipe:

1. Place a cover glass slip over a portion of the film to be milled to aid in determining when milling is complete.
2. Ion mill settings: accelerator voltage: 100 V; beam voltage: 300 V; discharge: $\sim$ 50 V; beam current: 95 mA (achieved by adjusting cathode); pump down to 8×10^{-6} mTorr (Ar on to 9×10^{-5} mTorr). Ion mill at 0 deg for 40 min (50 nm thick sample). Finish the ion mill process at 60 degree for 3 minutes. (Remember to change to 0 degree before closing the shutter.)
3. Take a picture under microscope.
4. Use AFM to check the etched sample if the etching rate needs to be calibrated.
5. Test the etching rate of the STS etcher using the witness cover glass slip (with 70 nm thick Ti); The file name of the etching recipe is "TCHEN200" (CF4). The etching time is about 3 min 0 sec for 70 nm Ti.
6. Etch the Ti layer on the permalloy samples after calibrating the etching time. (Place a witness cover glass slip with the sample to monitor the etching process.)
7. Deposit SiO_2 (60 nm thick) on the samples using the Varian E-beam evaporator in order to protect the patterned samples.

Once the samples have been fabricated, they should be stored under vacuum until they are going to be measured.

Appendix B

Details of Experimental Setup

Figs. B.1 and B.2 show the detailed diagrams of the experimental setups I used in the CW excitation and double modulation techniques. A general overview of the techniques are discussed in Ch. 2.

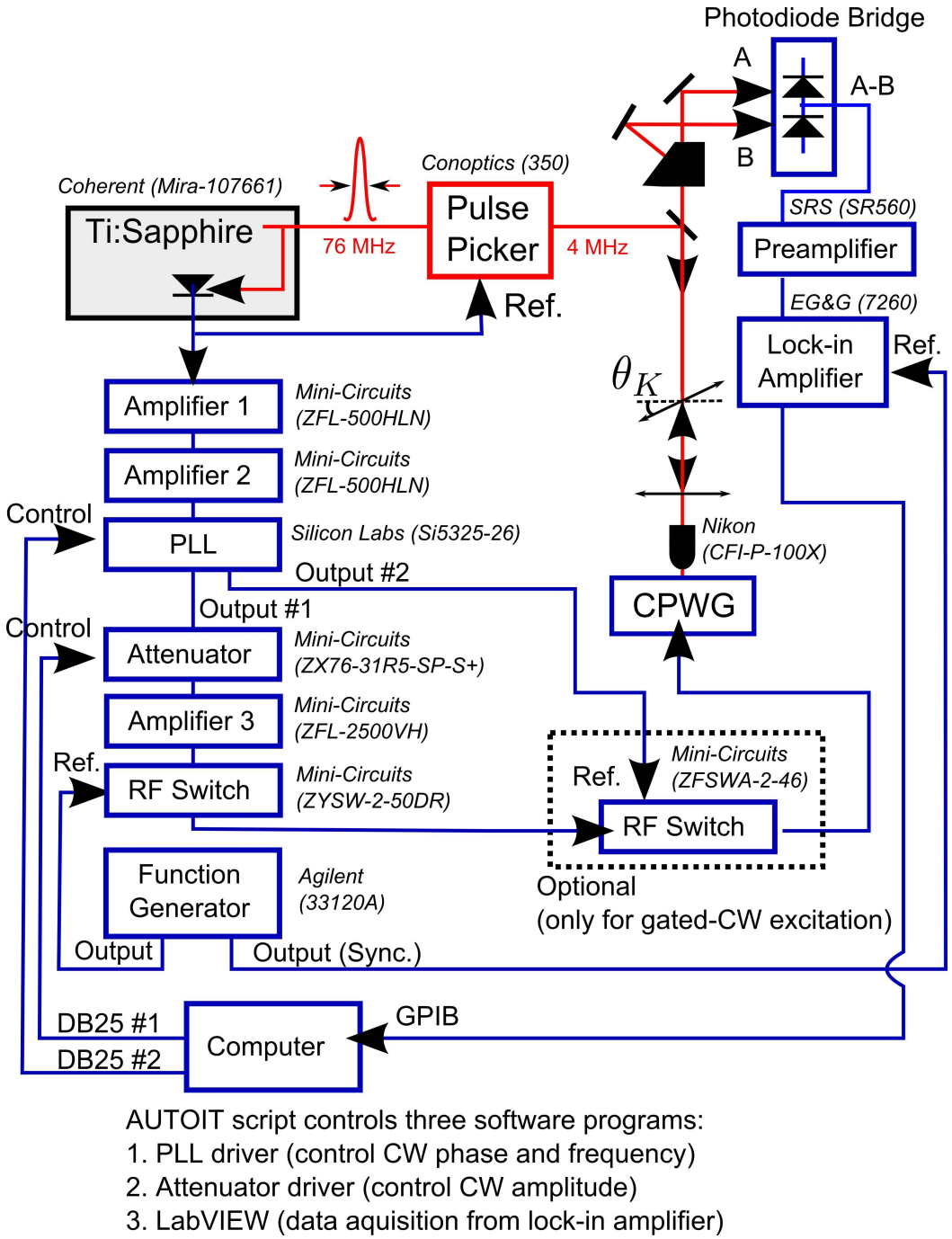

Figure B.1: Schematic diagram of the CW excitation technique.

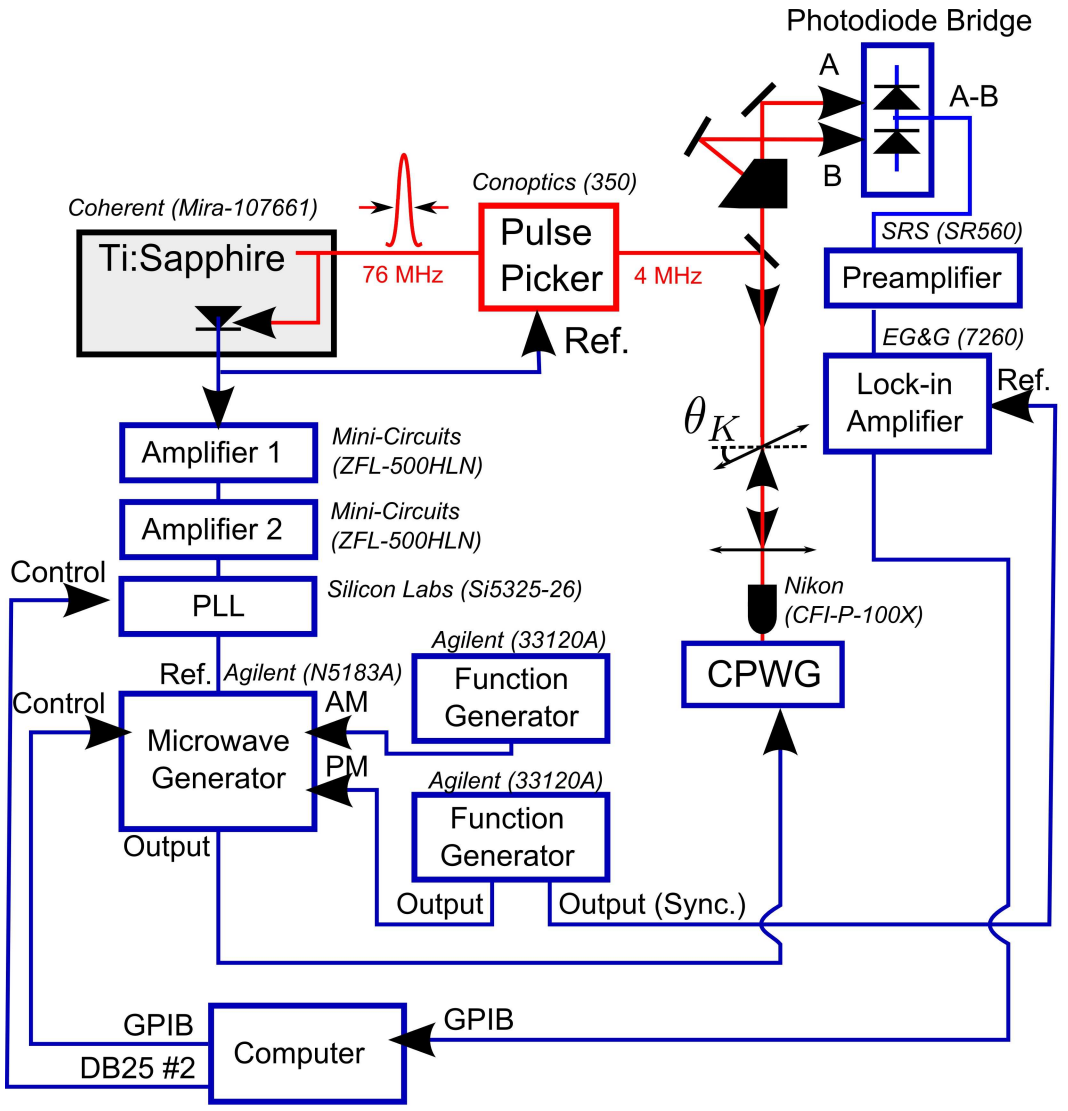

Figure B.2: Schematic diagram of the double-modulation excitation technique.

Appendix C

Glossary

C.1 List of Abbreviations

Table C.1: List of Abbreviatons

Abbreviation	Meaning
2D	Two-Dimensional
3D	Three-Dimensional
AFM	Atomic Force Microscopy
AM	Amplitude Modulation
CPGW	Coplanar Waveguide
CW	Continuous Wave
EBL	Electron Beam Lithography
FWHM	Full Width at Half Maximum
LLG	Landau-Lifshitz-Gilbert
MFM	Magnetic Force Microscopy
PLL	Phase Locked Loop
PM	Pulsed Modulation
PMGI	Polymethylglutarimide

Continued on next page

Table C.1 – continued from previous page

Abbreviation	Meaning
PMMA	Polymethylmethacrylate
PSD	Power Spectral Density
RMS	Root Mean Square
RF	Radio Frequency
SEM	Scanning Electron Microscopy
TRKM	Time-Resolved Kerr Microscopy

C.2 List of Symbols

Table C.2: List of Symbols

Symbol	Definition
A	Exchange constant
C	Vortex core chirality
D	Damping constant
D_{pin}	Pinning range
E_{pin}	Pinning energy
f_G	Gyrtropic mode frequency of a magnetic vortex
f_0	Reduced repetition rate of the probe beam in TRKM
f_{pin}	Pinned gyrotropic mode frequency
F	Force
F_{dep}	Depinning threshold force,
F_W	Critical force at Walker breakdown
k	Curvature (stiffness) of a parabolic potential
k_{pin}	Curvature (stiffness) of a pinning (parabolic) potential
k_B	Boltzmann constant = 1.38×10^{-16} ergs/k
$\mathbf{G}$	Gyrovector
$\boldsymbol{H_d}$	Dipole field
H_{depin}	Depinning (static) field
$\boldsymbol{H_{eff}}$	Effective magnetic field
$\boldsymbol{H_{ext}}$	External magnetic field
$\mathbf{h}(t)$	Time-dependent excitation field
$\boldsymbol{J}$	Angular momentum
L	Thickness of a magnetic disk
L_c	Critical thickness
L_{ex}	Exchange length

Continued on next page

Table C.2 – continued from previous page

Symbol	Definition
L_{DW}	Domain-wall width
$\boldsymbol{M}$	Magnetization (magnetic moment per unit volume)
m	Domain-wall mobility
m_z	Z-component of the magnetization normalized by M_s
M_s	Saturation magnetization
P	Vortex core polarization $p = \pm 1$
R	Radius of a magnetic disk
$\mathbf{r}$	Displacement of a vortex core
s	Cell height in quasi-3D micromagnetic simulations
T	Temperature
v_{DW}	Domain-wall velocity
W	Potential energy
W_{ex}	Exchange energy
W_H	Zeeman energy
W_{ms}	Magnetostatic energy
W_p	Pinning potential
α	Gilbert damping constant
δ	The phase difference between r_{CCW} and r_{CW}
ΔE	Critical energy for a thermal activation process
γ	Gyromagnetic ratio
λ	Wavelength
μ_B	Bohr magneton
ω_0	Precession frequency of magnetization
θ_K	Polar Kerr rotation
χ_Y	Displacement susceptibility of a vortex core in the y direction
ΔH	FWHM of the f_G peak observed in pinning maps
σ_{eff}	Effective roughness on the length scale of the vortex core